PHONON DISPERSION RELATIONS IN CRYSTALS

Gordon Edward Peckham,
Trinity College,
Cambridge.

Preface

Most of the work described in this dissertation was carried out at A.E.R.E. Harwell, during the tenure of a D.S.I.R. Research Studentship. I wish to thank Drs E. Bretscher and P. A. Egelstaff for providing the experimental facilities, and their staff for much help with the experimental work. I am especially indebted to my fellow research student, Mr S. K. Sinha, with whom I collaborated in building some of the apparatus, and who rendered invaluable assistance at all times.

I am grateful to members of the P.N.R. group at Harwell for many informal discussions; to Dr J. R. Hardy for suggesting the choice of magnesium oxide as a substance to study; to Dr W. Cochran for discussions about the *Shell Model* theory; and to my supervisor, Dr G. L. Sguires, for many helpful discussions and for his encouragement throughout the period of this research.

Detailed acknowledgements are given in the text and in Appendix IV.

A note on this digital version of the thesis

Optical character recognition was used to prepare digital text from a photocopy of the original thesis. The document was typeset using LaTeX with the American Mathematical Society's package *amsmath*. Line drawings were rendered into postscript using the package *pstricks*; other diagrams are from photocopies.

Pagination has changed – original page numbers are printed in the outside margins. Because diagrams may be in a different location with respect to the text some captions have been added to aid identification. The list of contents, of course, now refers to the new page numbers.

A few typographic and spelling errors in the original have been corrected.

G. E. Peckham
2011

Contents

Chapter 1

Introduction

Inelastic neutron scattering experiments can provide much information about the thermal motions in solids and liquids. Neutrons which have been thermalised by the moderator of a nuclear reactor have energies similar to those associated with these thermal motions. It so happens that they also have wavelengths similar to the interatomic spacing in solids and liquids. Quite large and easily measured changes in energies and wave vectors are apparent when neutrons are scattered from solids or liquids, and these may be related to properties of the thermal motions.

The theory of the thermal motions in a crystalline solid is well-known, and was first published as long ago as 1912 (Born, von Kármán, 1912). The motion is described in terms of plane waves or normal modes of vibration. At first, the only experimental information came from specific heat measurements, and the success of the very much simpler Debye theory did not encourage development of the Born–von Kármán crystal dynamics. However, discrepancies were apparent and some more detailed calculations were made (e.g. Kellermann 1940).

Since the introduction of nuclear reactors, large fluxes of thermal neutrons have been available for inelastic neutron scattering experiments. The scattering from a single crystal enables us to deduce the phonon dispersion relation, that is the frequency of the normal modes as a function of their wave vectors. These experiments provide a far more direct test of theories of crystal dynamics than do specific heat measurements.

The possibility of experimental measurements of the dispersion relation has stimulated theoretical work on crystal dynamics. The theory of ionic crystals is particularly well advanced. The *Shell Model* has been developed by Cochran and others to give excellent agreement with the experimental dispersion relations for the alkali halides (Cowley, Cochran, Brockhouse and Woods 1963).

This dissertation describes experiments to investigate the inelastic scattering of neutrons from a magnesium oxide single crystal. The phonon dispersion relation is deduced, and is discussed in terms of the *Shell Model* . The *Shell Model* is shown to provide a good description of the crystal dynamics of magnesium oxide. A less extensive experiment of the same type to deduce the phonon dispersion relation for a lead single crystal is also described.

Chapter 2

An Introduction to Lattice Dynamics and the Inelastic Scattering of Neutrons from Single Crystals

2.1 Introduction

The Born–von Kármán theory of crystal dynamics for crystals with more than one atom per unit cell is summarised to introduce the notation used in this thesis. The notation is similar to that of Born and Huang (1954), but cartesian components are indicated by superscripts, all other indices being written as subscripts. The principal features of the phonon dispersion relation are discussed, including the effects of crystal symmetry. The value of experimental measurements of this dispersion relation, and the advantages of thermal neutron scattering over other methods are emphasised. Two particular methods for neutron spectroscopy are mentioned, and the relevant cross section formulae given.

2.2 The Normal Modes of Vibration of a Crystal Lattice

The dynamics of crystals have been discussed at length by Born and Huang (1954). The basis of the Born von Kármán theory of crystal dynamics is the use of a potential function for the crystal which is a function of the nuclear coordinates only, and is quadratic in these coordinates. To derive such a potential function, we must make two approximations. The adiabatic approximation is to assume that the electrons accommodate themselves rapidly to the changing nuclear coordinates, so that the electron coordinates do not enter into the potential function. The electron does not make transitions from one state to another, but the state itself is continuously deformed by the nuclear motion. This is a good approximation if the energies of electron excitations are very much higher than the energies of vibration of the nuclei. This is the case for insulators, but it is more difficult to justify the approximation in the case of metals. The harmonic approximation is to ignore higher powers of the nuclear coordinates than the second. This is a necessary approximation in order to obtain a first solution to the problem, but is at variance with such properties of the crystal as thermal expansion and heat conduction. Having obtained a first solution in terms of normal modes of vibration, the effects of the higher powers may be described by an interaction between the normal modes.

A crystal has translational symmetry. That is, it could be built up from a series of identical cells placed together so as to fill the volume occupied by the crystal. The unit cell is the smallest such cell from which the crystal can be constructed. It is not unique, but all possible unit cells will have the same volume.

Consider a crystal with n particles in its unit cell. A particle is referred to

2

by two indices, l denoting the unit cell, and $k = 1, 2 \ldots, n$ denoting the position in the unit cell. The cartesian components of the particle displacements from their equilibrium positions are $U_{l,k}^{\alpha}$ where $\alpha = 1, 2, 3$. We write

$$\left(\frac{\partial^2 \Phi}{\partial U_{l,k}^{\alpha} \, \partial U_{l',k'}^{\beta}} \right)_0 = \Phi_{l-l',k,k'}^{\alpha,\beta}$$

where Φ is the potential energy of the crystal. Because of the symmetry of the lattice, this force constant depends only on the relative cell index $l - l'$, and not on l and l' individually. The equations of motion for each particle are

$$m_k \ddot{U}_{l,k}^{\alpha} = - \sum_{l',k',\beta} \Phi_{l-l',k,k'}^{\alpha,\beta} \, U_{l',k'}^{\beta}$$

where m_k is the mass of the kth particle in the unit cell, For an infinite lattice, we have an infinite number of simultaneous differential equations. These equations may be reduced by substitution of the wave solutions

$$U_{l,k}^{\alpha} = \frac{1}{\sqrt{m_k}} \xi_k^{\alpha} \exp \left\{ 2\pi i \, \boldsymbol{q} \cdot \boldsymbol{r}_{l,k} - i \, \omega t \right\}$$

ξ_k^{α} is a component of the polarisation vector, $\boldsymbol{r}_{l,k}$ is the position vector of the kth particle in the lth cell, ω is the angular frequency of the wave, and $\boldsymbol{q}$ is its wave vector. We obtain $3n$ simultaneous equations for ξ_k^{α}

$$\omega^2 \xi_k^{\alpha} = \sum_{k',\beta} M_{k,k'}^{\alpha,\beta} \, \xi_{k'}^{\beta}$$

where

$$M_{k,k'}^{\alpha,\beta}(\boldsymbol{q}) = \frac{1}{\sqrt{m_k m_{k'}}} \sum_{l'} \Phi_{l-l',k,k'}^{\alpha,\beta} \exp \left\{ -2\pi i \, \boldsymbol{q} \cdot (\boldsymbol{r}_{l,k} - \boldsymbol{r}_{l',k'}) \right\}$$

$$= \frac{\exp\{-2\pi i \, \boldsymbol{q} \cdot (\boldsymbol{r}_k - \boldsymbol{r}_{k'})\}}{\sqrt{m_k m_{k'}}} \sum_{l} \Phi_{l,k,k'}^{\alpha,\beta} \exp\{-2\pi i \, \boldsymbol{q} \cdot \boldsymbol{r}_l\} \qquad (2.1)$$

Here $\boldsymbol{r}_l$ is the position of an origin in the lth cell, and $\boldsymbol{r}_k$ is the position of the kth particle in the cell with respect to this origin. Thus

$$\boldsymbol{r}_{l,k} = \boldsymbol{r}_l + \boldsymbol{r}_k$$

Consider $M_{k,k'}^{\alpha,\beta}$, written out as a $3n \times 3n$ matrix. the row index is taken to be $(k + n\alpha - n)$, and the column index $(k' + n\beta - n)$. This is then the familiar eigenvalue problem. The dynamical matrix will have $3n$ eigenvalues denoted by $\omega_j^2(\boldsymbol{q})$, $j = 1, 2, \ldots, 3n$, and $3n$ corresponding eigenvectors $\xi_{k,j}^{\alpha}(\boldsymbol{q})$. The ω_j^2 are the solutions of the secular equation

$$\text{Determinant} \left(M_{k,k'}^{\alpha,\beta} - \omega^2 \delta_{\alpha,\beta} \delta_{k,k'} \right) = 0$$

The dynamical matrix is Hermitian i.e.,

$$M_{k',k}^{\beta,\alpha,} = \left(M_{k,k'}^{\alpha,\beta} \right)^{\star}$$

3

where $M^\star$ denotes the complex conjugate of M. This means that all its eigenvalues will be real. Furthermore, if any of the eigenvalues were negative, the frequency would be imaginary, and the lattice consequently unstable. The ω_j^2 are then real positive numbers. The polarisation vectors are orthogonal; i.e., when normalised

$$\sum_{\alpha k} \xi_{k,i}^\alpha \, \xi_{k,j}^\alpha = \delta_{ij}$$

The wave solutions are known as normal modes of vibration.

2.3 The Direct and Reciprocal Lattices

The positions specified by the vectors $\boldsymbol{r}_l$ form a regular lattice of points, known as the direct lattice, which is uniquely determined by the crystal structure. If we choose a lattice point as origin, we may express all lattice vectors $\boldsymbol{r}_l$ as multiples of three lattice vectors $\boldsymbol{a}_1$, $\boldsymbol{a}_2$, and $\boldsymbol{a}_3$, known as the basis vectors.

$$\boldsymbol{r}_l = l_1 \boldsymbol{a}_1 + l_2 \boldsymbol{a}_2 + l_3 \boldsymbol{a}_3$$

where l_1, l_2 and l_3 are integers. The basis vectors are not unique.

We define basis vectors of the reciprocal lattice by

$$\boldsymbol{b}_1 = \boldsymbol{a}_2 \wedge \boldsymbol{a}_3 / v \qquad \boldsymbol{b}_2 = \boldsymbol{a}_3 \wedge \boldsymbol{a}_1 / v \qquad \boldsymbol{b}_3 = \boldsymbol{a}_1 \wedge \boldsymbol{a}_2 / v$$

where $v = \boldsymbol{a}_1 \cdot (\boldsymbol{a}_2 \wedge \boldsymbol{a}_3)$ and is the volume of the unit cell.

The reciprocal lattice basis vectors have the following properties:

$$\boldsymbol{b}_i \cdot \boldsymbol{a}_j = \delta_{ij}$$

The scalar product between a vector in the direct and a vector in the reciprocal lattice is simply expressed in terms of their components in direct and reciprocal lattice basis vectors.

$$\text{If} \qquad \boldsymbol{r} = r_1 \boldsymbol{a}_1 + r_2 \boldsymbol{a}_2 + r_3 \boldsymbol{a}_3 \quad \text{and} \quad \boldsymbol{q} = q_1 \boldsymbol{b}_1 + q_2 \boldsymbol{b}_2 + q_3 \boldsymbol{b}_3$$
$$\text{then} \quad \boldsymbol{r} \cdot \boldsymbol{q} = r_1 q_1 + r_2 q_2 + r_3 q_3$$

Again, although the basis vectors arc not unique, the reciprocal lattice is uniquely determined by the crystal structure. Reciprocal lattice vectors; will be denoted by $\boldsymbol{\tau}$.

$$\boldsymbol{\tau} = h_1 \boldsymbol{b}_1 + h_2 \boldsymbol{b}_2 + h_3 \boldsymbol{b}_3$$

where h_1, h_2 and h_3 are integers. The scalar product between a direct lattice vector and a reciprocal lattice vector is an integer as

$$\boldsymbol{r}_l \cdot \boldsymbol{\tau} = l_1 h_1 + l_2 h_2 + l_3 h_3$$

2.4 The Phonon Dispersion Relation

Consider the effect on the dynamical matrix of adding a reciprocal lattice vector $\boldsymbol{\tau}$ to $\boldsymbol{q}$. The factor $e^{-2\pi i \boldsymbol{q} \cdot \boldsymbol{r}_l}$ in the sum in equation 2.1 is unchanged as $\boldsymbol{\tau} \cdot \boldsymbol{r}_l$ is an integer. The only effect is to multiply rows and columns of the

dynamical matrix by factors like $e^{-2\pi i \boldsymbol{\tau} \cdot \boldsymbol{r}_k}$. This will not alter the eigenvalues although the eigenvectors will be changed. (Some authors define the polarisation vectors as $(\xi_k^\alpha e^{2\pi i \boldsymbol{q} \cdot \boldsymbol{r}_k})$. In this case the eigenvectors also remain unchanged on adding a reciprocal lattice vector to the wave vector.)

A quantum of vibrational energy associated with a particular normal mode is known as a phonon. It has energy $\hbar\omega$ and wave vector $\boldsymbol{q}$. The frequency $\omega_j(\boldsymbol{q})$ as a function of $\boldsymbol{q}$ is known as the phonon dispersion relation. There are $3n$ branches of this relation corresponding to the $3n$ values of j. We have just shown that the dispersion relation is periodic in the reciprocal lattice, as $\omega_j(\boldsymbol{q})$ is unchanged when a reciprocal lattice vector is added to $\boldsymbol{q}$. All possible solutions are then obtained if $\boldsymbol{q}$ is restricted to a unit cell of the reciprocal lattice. This cell is normally chosen to be the first Brillouin zone. This is the region surrounding the origin enclosed by the planes which are the perpendicular bisectors of the reciprocal lattice vectors. The volume of the Brillouin zone is $1/v$, the unit cell volume of the reciprocal lattice.

If the crystal as a whole is displaced, there is no change in the potential energy. This leads to the relation

$$\sum_{l,k'} \Phi_{l,k,k'}^{\alpha,\beta} = 0$$

If the dynamical matrix is expanded for small $\boldsymbol{q}$, and this relation used, it can be shown that 3 branches of the dispersion relation pass through the origin, and in any particular direction, $\omega_j(\boldsymbol{q})$ is proportional to $|\boldsymbol{q}|$ for small $|\boldsymbol{q}|$. These solutions correspond to sound waves, where the crystal is behaving as a continuum. The normal modes described by these three branches are accordingly known as the acoustic modes. The other $(3n - 3)$ branches have non-zero frequencies and zero gradient when $\boldsymbol{q} = 0$. The corresponding normal modes are known as optic modes as, in ionic crystals, they can interact with infra-red radiation. In an acoustic mode of small $\boldsymbol{q}$, all particles in a unit cell are displaced by an equal amount in the same direction, but in an optic made of small $\boldsymbol{q}$, the centre of mass of the cell remains static.

2.5 Some Effects of Crystal Symmetry

The symmetry of the crystal will determine some features of the normal modes. The phonon dispersion relation shows the full symmetry of the crystal. Except for the acoustic modes at $\boldsymbol{q} = 0$, the dispersion relation is smooth and
continuous. For points lying on a mirror plane of the reciprocal lattice, the dispersion relation must, therefore, have zero gradient in a direction perpendicular to the mirror plane. It should be noted that the zone boundary frequently coincides with such a mirror plane.

For general values of $\boldsymbol{q}$, the directions of the polarisation vectors are determined by the details of the forces between the particles in the crystal. However, for some value of $\boldsymbol{q}$, the polarisation vectors lie parallel to $\boldsymbol{q}$ (longitudinal modes), or perpendicular to $\boldsymbol{q}$ (transverse modes), no matter what these forces are. This is the case for the optic modes with small $\boldsymbol{q}$, and for all modes in certain directions of high symmetry. With a suitable choice of axes, one axis (denoted by the superscript 1) lying in the direction of $\boldsymbol{q}$, the only non-zero

components of the polarisation vectors in the latter case are

Longitudinal $\xi_{k,j}^1$ $j = 1, 4, \ldots, 3n - 2$ $k = 1, 2, \ldots, n$

Transverse 1 $\xi_{k,j}^2$ $j = 2, 5, \ldots, 3n - 1$ $k = 1, 2, \ldots, n$

Transverse 2 $\xi_{k,j}^3$ $j = 3, 6, \ldots, 3n$ $k = 1, 2, \ldots, n$

With this choice of axes, the dynamical matrix is already diagonal in its cartesian indices: i.e.,

$$M_{k,k'}^{\alpha,\beta} = 0 \qquad \text{for } \alpha \neq \beta$$

Since the axes are determined solely by the symmetry of the crystal, the problem of calculating the eigenvalues for $\boldsymbol{q}$ in these symmetry directions is very much simplified. If $\boldsymbol{q}$ lies in a mirror plane of the crystal, one third of the modes will be polarised perpendicularly to this plane, but the other modes will be polarised in general directions in the plane.

For general values of $\boldsymbol{q}$, no classification into longitudinal and transverse types is possible. In fact the branches of the dispersion relation frequently mix, so that it is possible to find a continuous smooth path in the dispersion relation linking a point on one branch with a point on another.

The symmetry of the crystal may cause same of the solutions to be degenerate. For instance, the transverse modes in a (1,0,0) direction in a cubic crystal describe exactly equivalent motions of the particles, and must, therefore, have the same frequencies.

Some of the features of the phonon dispersion relation discussed in the last two sections are shown in the following diagram. This shows a dispersion relation in the (1,0,0) direction for sodium chloride ($n = 2$) calculated by Kellermann (1940).
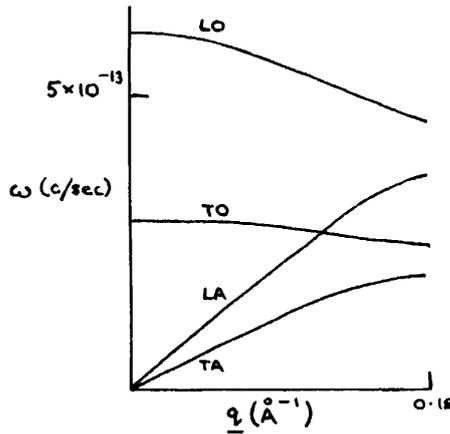
Figure 2.1: Phonon dispersion relation for sodium chloride

A denotes an acoustic mode, O an optic mode, L a longitudinally polarised mode and T a transversely polarised one. The transverse modes are degenerate, and all modes have zero gradient at the zone boundary.

6

2.6 Periodic Boundary Conditions

When discussing the energy of a crystal, or the quantum mechanics of lattice dynamics, it is desirable to consider a crystal of finite size. We impose periodic boundary conditions to maintain the translational symmetry of the lattice and to enable the equations of motion to be reduced as before. It is reasonable to suppose that, for a large enough crystal, the conditions at the boundary will have little effect on the normal modes of vibration. In fact it can be shown that the number of normal modes with frequencies between two given values will be changed by a fraction of order $1/\sqrt[3]{N}$ by a change in boundary conditions for a crystal containing N particles (Born and Huang, 1954).

Suppose that the crystal is a parallelepiped with edges parallel to the basis vectors, and contains N_1, N_2, and N_3 unit cells in the directions of the three basis vectors. Imagine this crystal repeated to form an infinite crystal. We apply our previous theory to this infinite crystal, but the motions of the unit cell with position

$$\boldsymbol{r}_{l+N} = (l_1 + N_1)\boldsymbol{a}_1 + (l_2 + N_2)\boldsymbol{a}_2 + (l_3 + N_3)\boldsymbol{a}_3$$

are to be identical with the motions of the cell at

$$\boldsymbol{r}_l = l_1\boldsymbol{a}_1 + l_2\boldsymbol{a}_2 + l_3\boldsymbol{a}_3$$

for all integral l_1, l_2 and l_3. This implies that

$$e^{2\pi i\,\boldsymbol{q}\cdot\boldsymbol{r}_{l+N}} = e^{2\pi i\,\boldsymbol{q}\cdot\boldsymbol{r}_l}$$

or $q_1 N_1$, $q_2 N_2$, and $q_3 N_3$ must be integers, where

$$\boldsymbol{q} = q_1\boldsymbol{b}_1 + q_2\boldsymbol{b}_2 + q_3\boldsymbol{b}_3$$

$\boldsymbol{q}$ is then restricted to the points of a sub-reciprocal lattice. There are N allowed values of $\boldsymbol{q}$ in the Brillouin zone, where $N = N_1 N_2 N_3$ and is the number of unit cells in the crystal. It is interesting to note that we now have $3Nn$ normal modes to describe the motion of Nn particles, which is equal to the number of degrees of freedom of the system.

2.7 Experimental Methods of Investigating the Phonon Dispersion Relation

The dispersion relation may be calculated if the interactions between the particles forming the crystal are known. A knowledge of the dispersion relation from experiment will provide a fairly direct test of the correctness of the theoretical interactions. The calculation can be reversed to some extent so that the force constants are deduced from the dispersion relation. In particular Foreman and Lomer (1957) have shown that the range of the forces may be found by a Fourier analysis of the dispersion relation in symmetry directions. An experiment to determine the dispersion relation will, then, give considerable information about the forces coupling the particles in a crystal.

Some information is available from quantities depending on the frequency distribution function $f(\nu)$, where $\nu = {}^{\omega}\!/_{2\pi}$. If there are $F(\nu)$ modes with frequency between ν and $\nu + \Delta\nu$, we may write

$$f(\nu) = \frac{1}{3n} \lim_{\Delta\nu\to 0} \left\{ \frac{1}{\Delta\nu} \lim_{N\to\infty} \left(\frac{F(\nu)}{N} \right) \right\}$$

7

where $f(\nu)$ has been normalised so that

$$\int_0^\infty f(\nu)\, d\nu = 1$$

$f(\nu)$ may be written as a surface integral over the branches of the dispersion relation (Born and Huang, 1954):

$$f(\nu) = \frac{v}{3n} \sum_j \iint \frac{dS_j}{|\mathrm{grad}\, \nu_j(\boldsymbol{q})|}$$

Here dS_j is an element of area of the surface $\nu_j(\boldsymbol{q}) = \nu$

The frequency distribution function has the advantage that it contains information about the dispersion relation for all values of $\boldsymbol{q}$, whereas direct methods of obtaining the dispersion relation are usually restricted to a coarse sample of $\boldsymbol{q}$ by the limited volume of experimental data it is possible to handle. However, it is impossible to obtain the dispersion relation from the frequency distribution, and it does not provide a very detailed check on theories of the forces linking particles in the crystal.

The frequency distribution function is an important factor in incoherent neutron scattering, defect induced and two phonon infra-red absorption, and, of course, the specific heat as a function of temperature. However, it is not usually possible to reconstruct the frequency distribution function unambiguously from the experimental data, although this has been done in some cases (Turberfield and Egelstaff, 1960).

The expression given for $f(\nu)$ contains the gradient of the dispersion relation in the denominator of the integrand. Discontinuities in the slope of $f(\nu)$ occur at frequencies corresponding to the critical points where this gradient vanishes. The shape of the curve in the region of the singularity depends on whether the critical point is a maximum, minimum, or a type of saddle point (Van Hove, 1953). The wave vectors for many critical points are determined by the crystal symmetry. Such singularities have been seen in the two phonon infra-red absorption spectrum of diamond (Hardy and Smith, 1961). The singularities have been allocated to the known critical points, so that the frequencies of some normal modes have been determined.

The most direct information about the dispersion relation comes from experiments in which a photon or a neutron interacts coherently with one phonon. In this type of interaction energy and quasi-momentum are conserved according to the following equations:

$$E_1 - E_0 = \pm h\nu$$
$$\boldsymbol{k}_1 - \boldsymbol{k}_0 = \boldsymbol{Q} = \pm\boldsymbol{q} + \boldsymbol{\tau} \tag{2.2}$$

E_1, $\boldsymbol{k}_1$ are the energy and wave vector of the scattered particle, and E_0, $\boldsymbol{k}_0$ are the corresponding quantities for the incident particle. The equations describe the annihilation $(+)$ or the creation $(-)$ of a phonon. If the energy and wave vector of the particle are known both before and after scattering, the energy and wave vector of the interacting phonon can be determined. This calculation can be made with any precision only if the particle energy and wave vector are similar to that of the phonon. The energy wave vector relationships for photons, neutrons and phonons are shown in fig 2.2. The suitability of thermal neutrons
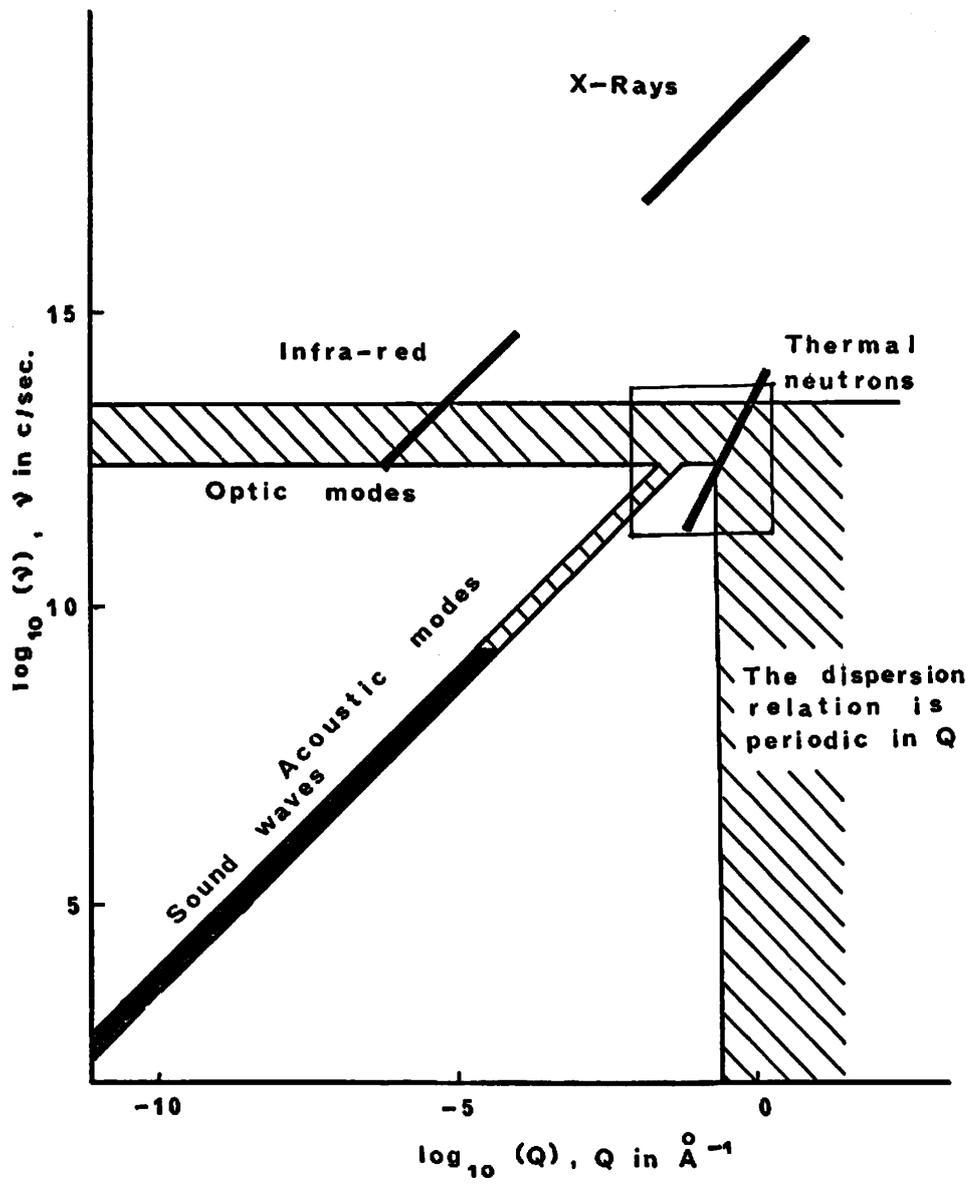
Figure 2.2: Phonon frequencies and wave vectors

for these measurements is obvious. Infra-red radiation interacts with the optic modes of small q, in ionic crystals, and the frequencies of these modes may be determined from the infra-red absorption spectrum. X-rays interact with a useful range of wave vectors, but the energy change is far too small to be observed. Dispersion relations have, however, been determined from the diffuse X way scattering, as the energies may be obtained from the scattered intensity if the polarisation vectors are known. In practice this restricts the measurements to the dispersion relations in symmetry directions of crystals with one atom per unit cell. Walker (1956) has determined the dispersion relation for aluminium in this way. The most useful region in which to obtain information about the dispersion relation away from the limits of small q is shown in the figure by the red square*. The Energy wave vector relation for thermal neutrons is seen to pass through this region.

The gradients of the acoustic modes for small q are of course the velocities of sound in the crystal which may be measured by means of ultrasonic techniques or may be calculated from the elastic constants measured in some other way.

2.8 Methods for Neutron Spectroscopy

The only practicable source of thermal neutrons for this type of inelastic scattering experiment is a nuclear reactor. A collimator let into the shielding wall of a reactor allows a beam of thermal neutrons to emerge. Two methods may be use to monochromate this beam. In the first, the beam is Bragg-reflected from a single crystal monochromator, and in the second the beam is passed through a mechanical velocity selector. The monochromatic beam impinges on the single crystal sample, and some of the neutrons are inelastically scattered. There are again two methods of determining the energy of these scattered neutrons. They may be Bragg-reflected by a single crystal analyser, or the beam may be pulsed, and the neutrons timed over a flight path to the detectors. Peaks will be observed in the scattered energy spectrum, corresponding to neutrons satisfying equations 2.2. These peaks have a width depending an the resolution of the apparatus and on anharmonic effects (caused by the inadequacy of the harmonic approximation).

The three axis spectrometer (Brockhouse, 1960) makes use of Bragg reflection both to define the incident neutron energy and to determine the scattered neutron energy. In the chopper-time of flight apparatus used in the present experiments, the mechanical velocity selector also pulses the beam, allowing the energy of the scattered neutrons to be determined by the time of flight technique. These instruments are shown schematically in f1g 2.3.

The three axis spectrometer uses a continuous beam, but only analyses one scattered energy at once, whereas time chopper-time of flight apparatus uses an interrupted beam, all energies of scattered neutrons being analysed simultaneously. The times taken to determine a phonon frequency by these two techniques are similar. The main advantage of the three axis spectrometer is that the energy and wave vector change undergone by a neutron arriving at the detector is completely under the experimenter's control. By suitable manipulation of the instrument, the energy change may be varied while the wave vector change remains constant. If the energy change is scanned in small steps, a peak intensity will be observed for energies corresponding to the energies of phonons with this

---

black in this copy

Sample

Detector

Reactor

Collimator

Analyser

Monochromator
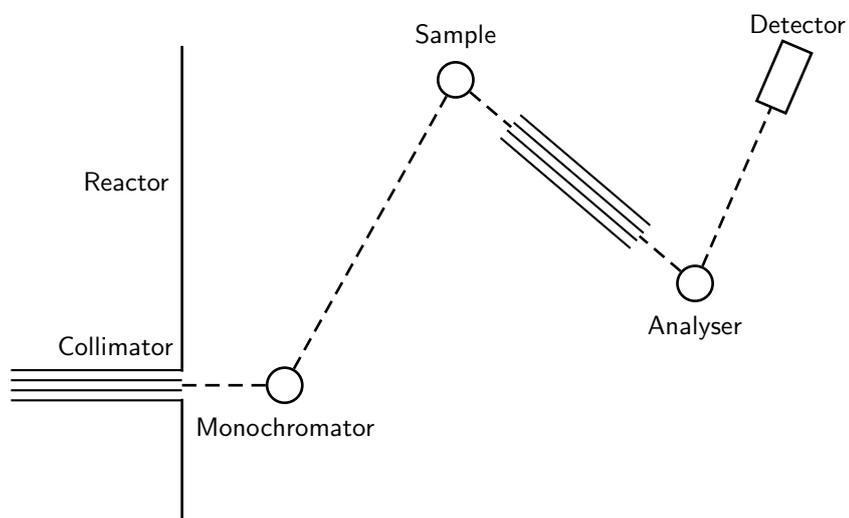
Figure 2.3a: Triple axis spectrometer

Detector

Reactor

Flight path

Rotor

Collimator

Sample
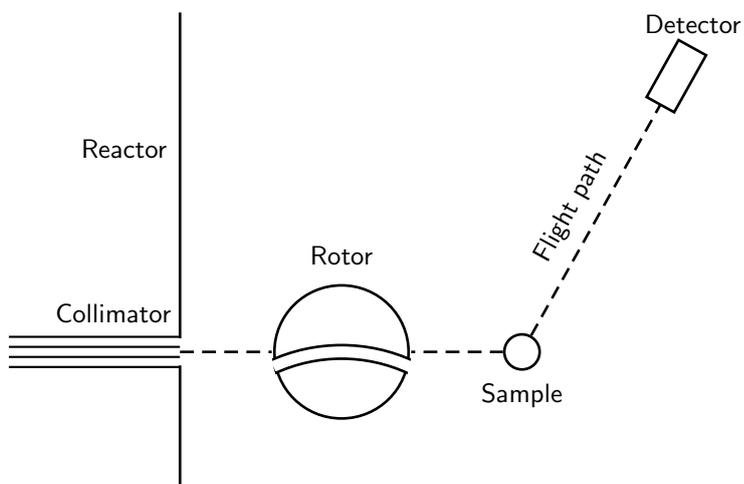
Figure 2.3b: Chopper-time-of-flight apparatus

wave vector. This method of using the spectrometer is known as the constant $\boldsymbol{Q}$ method (Brockhouse, 1960). It is a very convenient method for obtaining the dispersion relation in symmetry directions of the crystal. With the time of flight apparatus, such exact control of the wave vector is not possible, and the best that normally can be done is to ensure that the phonon wave vectors lie in a mirror plane of the crystal. The main advantage of the time of flight apparatus is that many detectors my be used simultaneously, and in this case information is obtained considerably faster than with the three axis instrument. The three axis spectrometer can also give misleading results due to second order contamination in either the monochromator or the analyser, or both. The time of flight apparatus is, of course, not subject to this trouble.

2.9 The Neutron Cross Section Formula

The theory of the inelastic scattering of thermal neutrons by a single crystal has been given by Placzek and Van Hove (1954) and by Waller and Fröman (1952). The scattering cross section per unit solid angle per unit cell for a coherent scattering process in which one phonon is created or destroyed may be written as

$$\frac{d\sigma}{d\Omega} = \frac{h}{2(2\pi)^3} \frac{|k_1|}{|k_0|} \frac{1}{\nu_j} P_j \frac{g_j^2}{J_j} \tag{2.3}$$

The population factor P_j is equal to $\left\{ \exp\left(\frac{h\nu_j}{k_B T} \right) - 1 \right\}^{-1}$ when a phonon is annihilated, and to one plus this expression when a phonon is created. k_B is Boltzmann's constant, and T is the absolute temperature of the sample. J_j is the Jacobian factor giving a measure of the number of normal modes contributing to the process.

$$J_j = \left| 1 \mp \frac{h}{2E_1} \left(\boldsymbol{k}_1 \cdot \boldsymbol{\nabla} \nu_j(\boldsymbol{q}) \right) \right|$$

The $(-)$ sign is used when a phonon is annihilated, the $(+)$ sign when a phonon in created.

$$g_j^2 = \left| \sum_k \frac{b_k \boldsymbol{Q} \cdot \boldsymbol{\xi}_{k,j}}{m_k^{\frac{1}{2}} e^{W_k}} e^{2\pi \, i\boldsymbol{\tau} \cdot \boldsymbol{r}_k} \right|^2$$

where b_k is the bound scattering length of the kth type of nucleus averaged over all the unit cells and e^{-2W_k} is the Debye Waller factor for the kth type of particle.

The factor $e^{2\pi \, i\boldsymbol{\tau} \cdot \boldsymbol{r}_k}$ would be replaced by $e^{2\pi \, i\boldsymbol{Q} \cdot \boldsymbol{r}_k}$ if the polarisation vectors were defined in the alternative way suggested in section 2.4

P_j becomes very small for high frequencies or low sample temperatures. In these cases, the experiment must involve the creation of phonons in order to obtain a reasonably large cross section.

The integrated intensity under a peak in a time of flight spectrum is proportional to the cross section given. The integrated intensity under a peak obtained in a constant $\boldsymbol{Q}$ experiment using a triple axis spectrometer, however, does not depend on the Jacobian term J_j. This is an advantage if the intensities are to be used to give information about the polarisation vectors (Brockhouse et al., 1962).

Chapter 3

Cold Neutron Apparatus

3.1 Introduction

Both the experiments described in this thesis made use of the Cold Neutron Apparatus on D.I.D.O. reactor. This consists basically of a mechanical chopper with associated apparatus for time at flight analysis. It was designed and is run by members of the P.N.R. group of the Nuclear Physics Division at A.E.R.E. Harwell primarily as an instrument to study inelastic neutron scattering from liquids and polycrystalline solids. The apparatus has been described by Harris, Cocking, Egelstaff and Webb (1962), and only a brief description will be given here.

The scattering from a liquid or polycrystalline solid does not depend on the orientation of the sample. Consequently the scattering is the same in all directions lying on a cone of constant scattering angle. The detectors are divided into several banks each consisting of detectors placed around such a cone. This arrangement is not suitable for observing the scattering from a single crystal sample. We have, therefore, added a second array of detectors which have good angular resolutions both in the scattering plane and perpendicular to it. These detectors all lie in the vertical plane through the sample. A goniometer has been constructed which allows adjustment of the sample orientation. The theory of the transmission of a curved slot rotor is treated in some detail as it is fundamental to a discussion of the resolution of the apparatus. It is not claimed that this treatment is original. Collins (1961) ascribes the fundamental approximation of the method to Butterworth. The use of slots in the form of a circular arc is justified in spite of the very narrow slot width ($^1/_{10}$ ins), and the effects of the off centre slots are considered, in Appendices I and II.

The resolution of the apparatus and the factors governing the choice of a detector are also discussed.

3.2 The Cold Neutron Apparatus

The general layout of the apparatus is shown in fig. 3.1. The appearance of the apparatus with the original detector shielding is shown in fig. 3.2, and with the extended shielding for twelve detectors in fig. 3.3.

The low energy neutron flux in the reactor is increased by a liquid hydrogen moderator. The moderator chamber is only 3 ins in diameter so full thermalisation to liquid hydrogen temperatures is impossible. In practice a fourfold increase in flux at 4 Å is observed when the chamber is filled. The moderator chamber is refrigerated by circulating liquid hydrogen through cooling coils in the chamber. The liquefying apparatus is designed to run continuously and largely automatically for a reactor cycle of three weeks. The cold neutron source has been described by Webb and Pearce (1962).

Neutrons of wavelength less than 4 Å are scattered from the beam before it emerges from the reactor shield by a polycrystalline beryllium filter. This

13
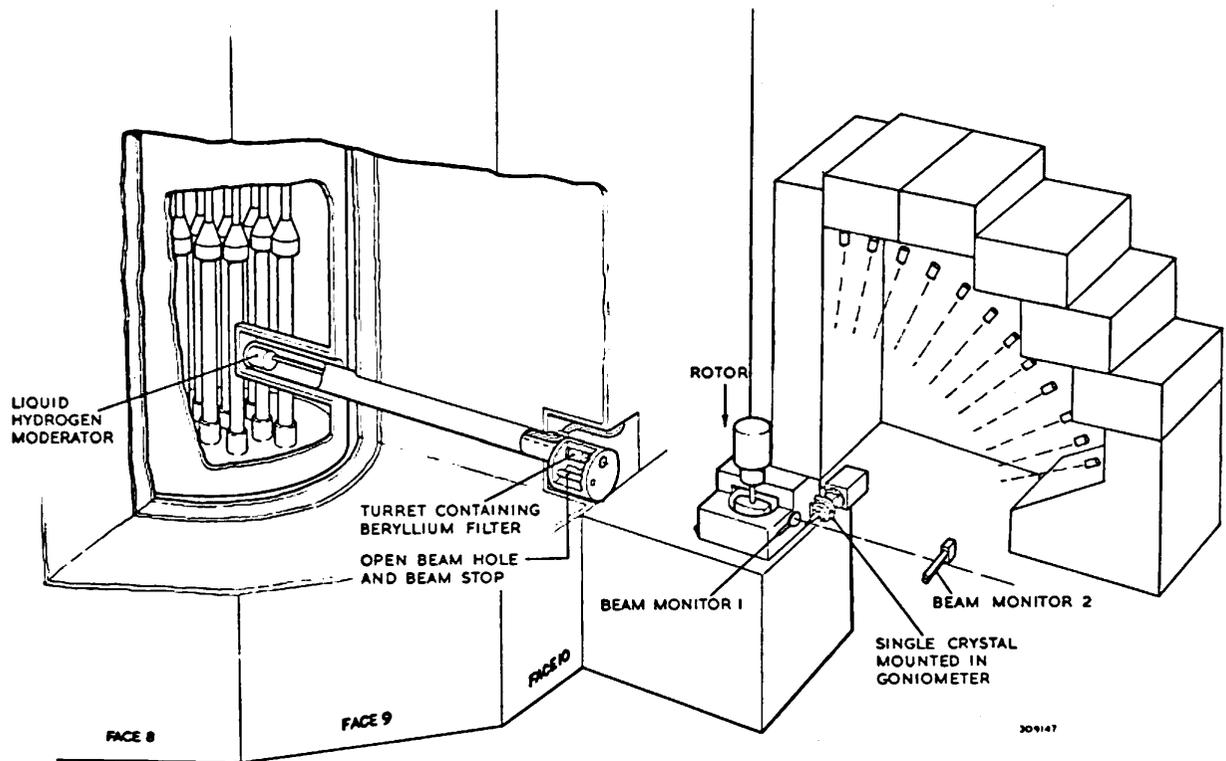
Figure 3.1: Cold neutron apparatus (diagram)

Figure 3.2: Cold neutron apparatus (photo)

Figure 3.3: Cold neutron apparatus (photo)

REACTOR SPECTRUM

SPECTRUM FROM
LIQUID H_2 MODERATOR

Be FILTERED SPECTRUM

SPECTRUM TRANSMITTED
BY ROTOR $(\times 500)$

NUMBER OF NEUTRONS PER SECOND PER UNIT WAVELENGTH RANGE

NEUTRON WAVELENGTH IN Å
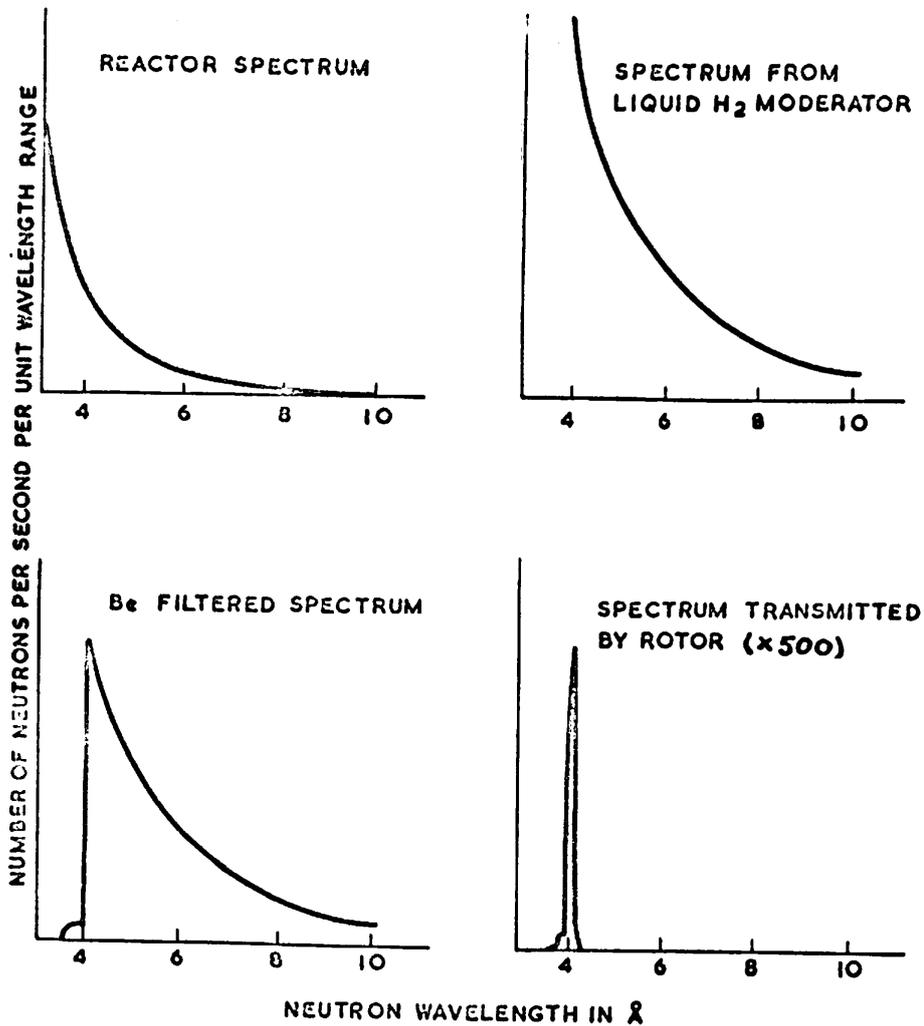
Figure 3.4: Neutron spectra – cold neutron apparatus DIDO

filter is cooled with liquid nitrogen to increase its transmission for neutrons of wavelength greater than 4 Å. A bismuth single crystal is also placed in the beam, and this, together with the beryllium filter, considerably reduces the flux of fast neutrons and γ rays emerging from the reactor. The filter is mounted in a turret so that it can be swung out of the beam and replaced either by a beam stop, or by a collimator allowing an unfiltered beam to be obtained. The unfiltered beam is $1/4$ ins in diameter and is attenuated by 2 ins of lead. It is used in aligning the sample as described in Appendix III.2.

The low energy neutron beam emerging from the reactor is pulsed and rendered monochromatic by a curved slot rotor spinning at high speed. The action of the rotor is considered later in this chapter. Neutron spectra at various points in the incident beam are shown in fig. 3.4. The bursts of monochromatic neutrons are scattered by the sample which is placed as near the rotor as possible,

17
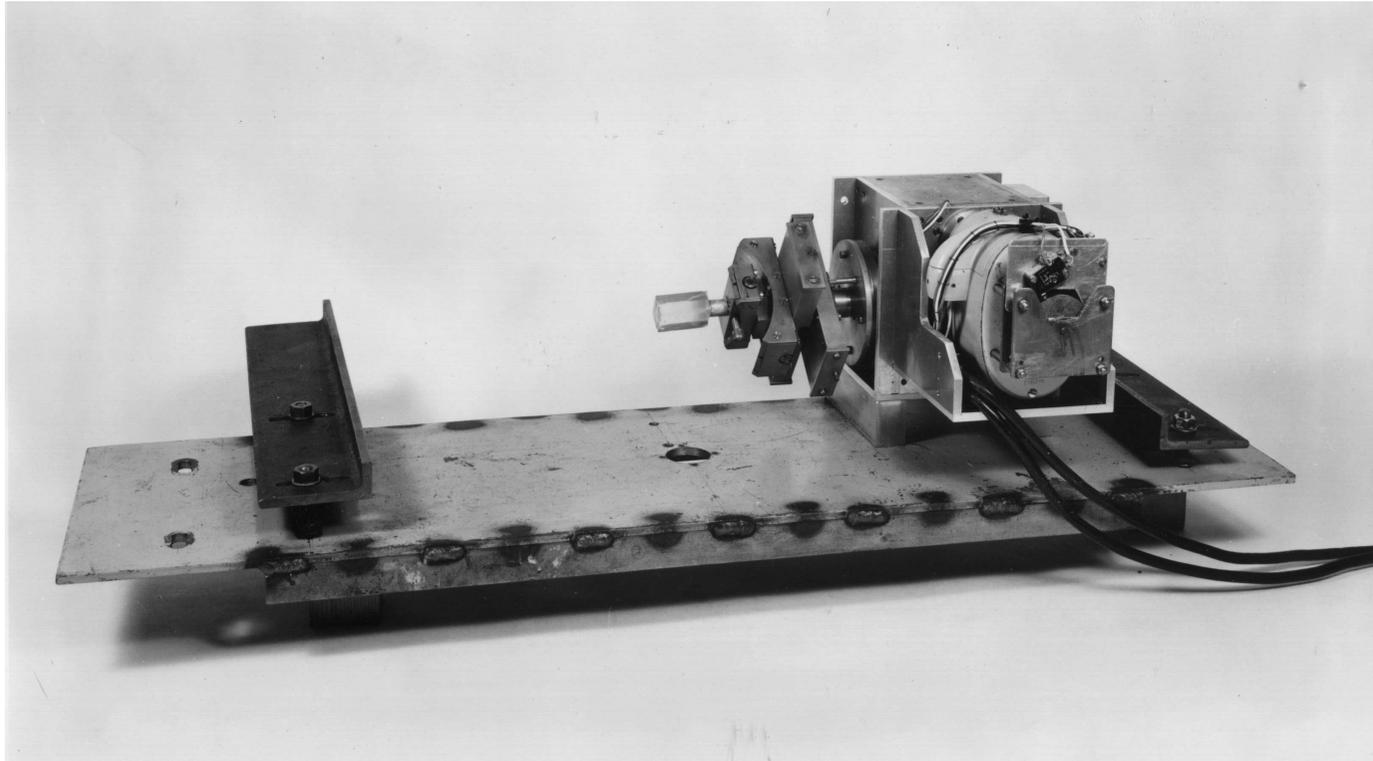
Figure 3.5: Goniometer

and the neutrons then travel over a 2.3m flight path before reaching the detectors. The goniometer on which the single crystal sample is mounted is described elsewhere (Peckham, 1964c) and the detectors are Li-ZnS scintillators described later in this chapter.

Two monitor detectors are placed in the beam, one just before the sample, and the second $1^1/2$ m away at the beam stop.

The massive detector shielding seen in the photographs consists of one foot thick water tanks at the side topped with tanks containing a mixture of borax and wax. The side tanks are also lined with 3 ins pockets filled with borax. The inside surface of the shielding is covered with 0.05 ins cadmium sheet. It is preferable to absorb the bulk of the neutrons in boron rather than cadmium as the high energy γ ray emitted by the cadmium may be detected by the scintillator.

The time of arrival of the neutrons at the detectors is measured by means of a crystal oscillator driving dividing circuits which are released by a start pulse from the rotor. The time of arrival is recorded on magnetic tape together with an indication of which detector registered the neutron. This tape may subsequently be analysed to give a time of flight spectrum for each detector. A time of flight spectrum is also obtained from the beam monitors from which the time of arrival of the neutron burst at the sample may be deduced. The tape recorder time of flight analyser is more fully described in the next chapter.

3.3 Rotor Theory

A beam of thermal neutrons may be pulsed and rendered monochromatic by means of a mechanical rotor spinning in the beam. The type used in these experiments consists of a disc of magnesium-cadmium alloy in which a number of curved slots have been cut. When the disc is spinning, only neutrons with velocities within a limited range can pass through the slots without striking the walls where they would be absorbed by the cadmium in the magnesium-cadmium alloy. In practice there may be as many as 12 slots.
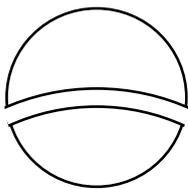
Figure 3.7: The rotor (diagram)

The slots are cut as arcs of a circle all on the same centre. It is shown in Appendix I that a circular arc is a good approximation to the path of a neutron relative to the rotor, but the fact that all the slots have the same centre of curvature does cause some extra spread in the velocities passed (see Appendix II). The rotor is suspended in a vacuum tank and is spun at high speed (up to about 600 revolutions per second) by a hysteresis motor. The calculation of the transmission function is simplified if it is assumed that all neutrons whose paths relative to the rotor pass through both ends of the slot are transmitted. This is

Figure 3.6: The rotor (photo)

not strictly true as it is possible for some of these neutrons to strike the walls of the slot en route. However, the results obtained agree substantially with those of Marseguerra and Pauli (1959) who make an exact calculation for parabolic slots. The method used by these authors and the method used in the present treatment involve approximations when the slots are circular arcs and it is not obvious that one method is more accurate than the other. With this assumption, the rotor may be replaced by two shutters in the beam, separated by a rotor diameter, and moving with opposite velocities across the beam. The following diagram (fig. 3.8) shows the shape in space of the groups of neutrons passed by the two shutters when a beam of neutrons of a given velocity is incident on either of them. Obviously the beam will only be transmitted through the pair of shutters if the two groups overlap, and the transmission will be proportional to the area of overlap.
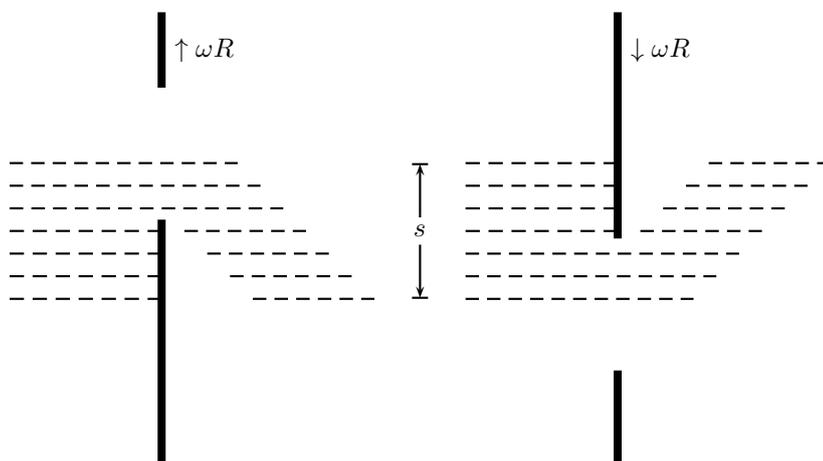
Figure 3.8: Neutron groups formed by moving shutters

In the following analysis,

R is the rotor radius
ω is the rotor angular velocity
s is the rotor slot width
n is the neutron inverse velocity
t is the time of arrival of the neutron at the rotor centre.

The shutter speed is ωR and the length of the neutron group in time at a given position across the slot is $\tau_1 = s/\omega R$

Let shutter 1 be fully open at a time $-\tau$, and shutter 2 be fully open at time τ.

The centre of the group passed by shutter 1 will arrive at the rotor centre at time $-\tau + Rn = -\tau_2$

The centre of the group passed by shutter 2 passed the rotor centre et time $\tau - Rn = +\tau_2$

We may now show the various degrees of overlap between the two groups, plotting time at the rotor centre instead of distance along the beam. Thus overlapping areas are shaded (fig. 3.9).

21

Group passed by 1st shutter

Group passed by 2nd shutter

Distance across slit

A

B

C
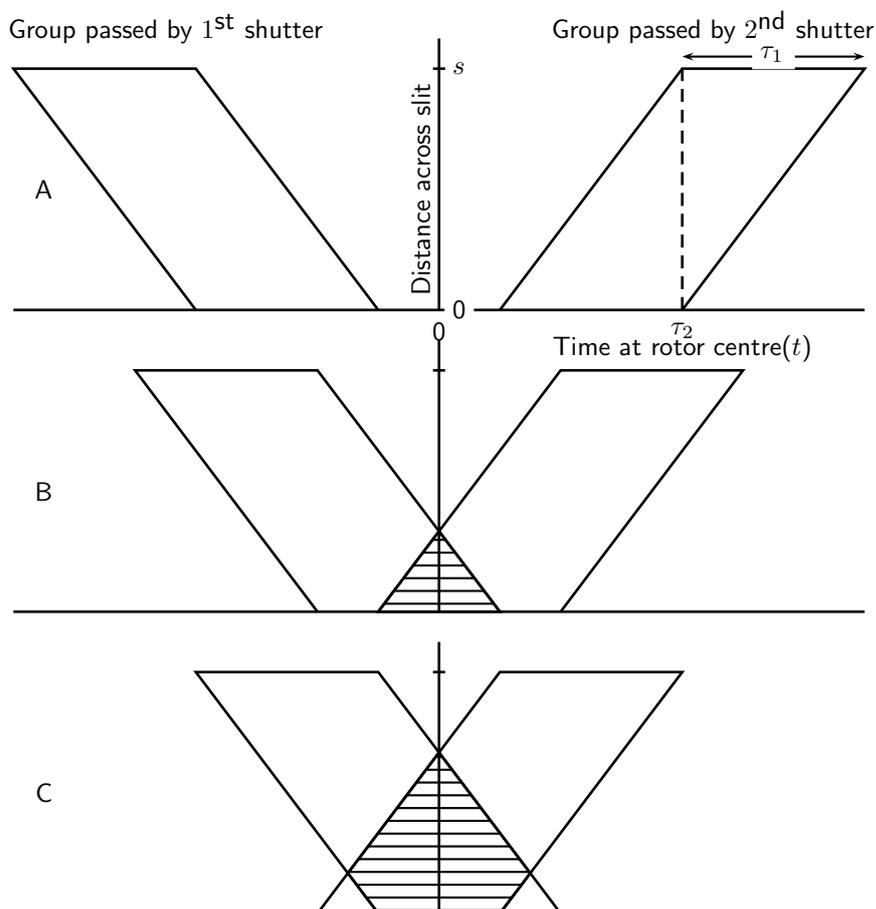
Figure 3.9: The three degrees of overlap between the neutron groups passed by the two shutters

The transmission function, f, is a function of n and t, or of τ_2 and t. f is proportional to the height of the shaded areas in the diagrams, and is equal to 1 when this height is s, i.e., when neutrons are allowed through across the whole width of the slot. f is plotted as a function of t for two values of τ_2, corresponding to the two degrees of overlap shown for the neutron groups. If we combine these cases, f as a function of τ_2 and t is found to form the hexagonal pyramid shown in plan in the last diagram (fig. 3.10).

If the transmission function is expressed as a function of t only by integrating over τ_2, the following form is obtained (fig. 3-11)

22

Case A, $\tau_2 \geq \tau_1$, $f = 0$

Case B, $\tau_1 \geq \tau_2 \geq \tau_1/2$

Case C, $\tau_1/2 \geq \tau_2 \geq 0$

$$f = 1 - \frac{2t}{\tau_1} \qquad f = 1 - \frac{\tau_2 + t}{\tau_1}$$
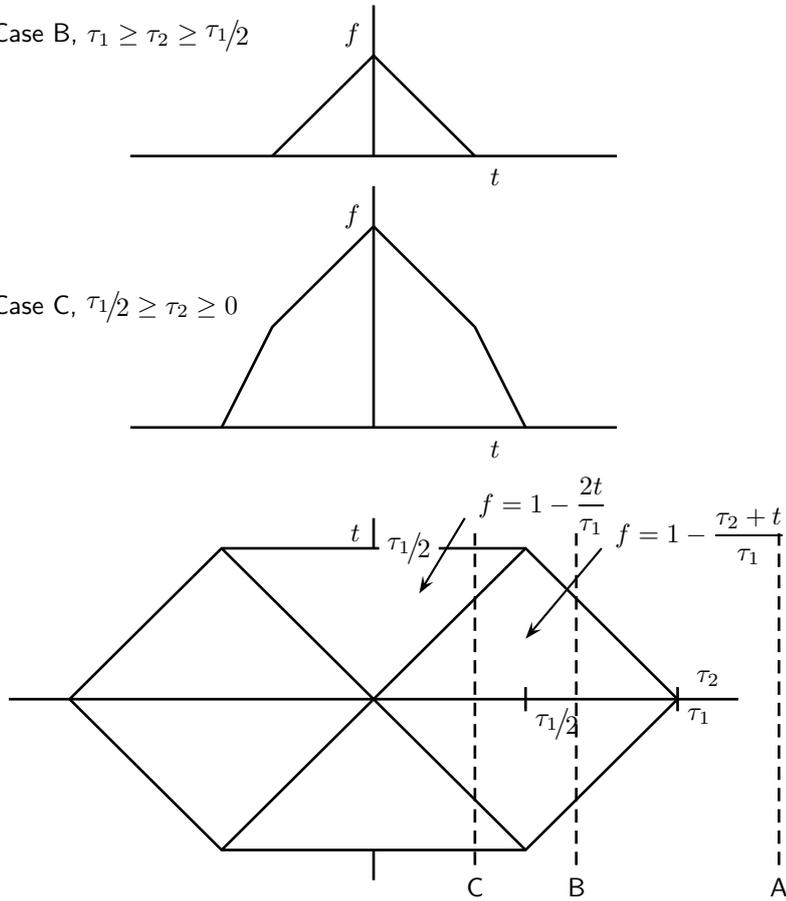
Figure 3.10: The rotor transmission function $f(\tau_2, t)$
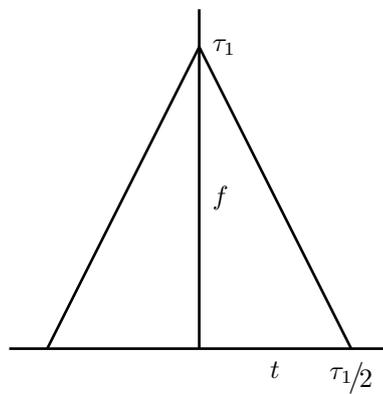
Figure 3.11: Rotor transmission as a function of t

23

The second moment of this function is $\tau_1^2/24$.

The transmission function may also be expressed as a function of τ_2 by integrating over t.
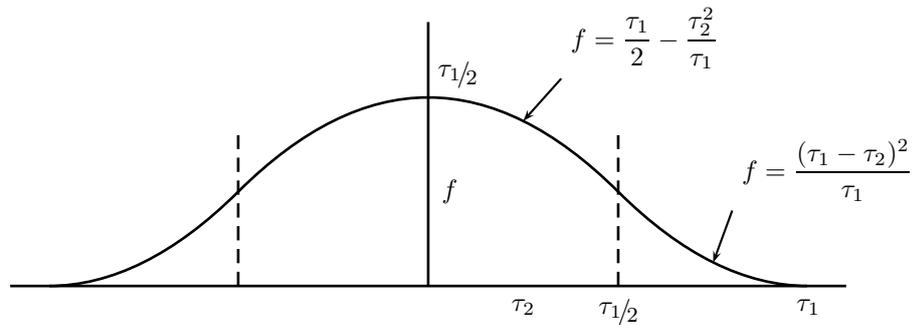
Figure 3.12: Rotor transmission as a function of τ_2

The second moment of this function is $\tau_1^2/8$.

The total transmission is found by integrating either of the above curves to be $\tau_1^2/2$.

The results may be expressed in terms of n_0, the neutron inverse velocity for which the transmission function is a maximum ($n_0 = \tau/R$). Let the ratio of the best transmitted neutron speed to the rotor tip speed be p.

$$p = 1/\omega R n_0$$

Now $\quad \tau_1 = s/\omega R$

Hence $\quad \tau_1 = s p n_0$

We may define a time spread δt at the centre of the rotor by

$$(\delta t)^2 = \frac{\int_{-\infty}^{\infty} t^2 f(t)\, dt}{\int_{-\infty}^{\infty} f(t)\, dt}$$

where $\quad f(t) = \displaystyle\int_{-\infty}^{\infty} f(n, t)\, dn$

The spread in inverse velocities δn is similarly defined. If the number of incident neutrons falling on area dA in time dt with inverse velocities in the range n to $n + dn$ is $(N\, dA\, dt\, dn)$, then the number of neutrons passing the rotor in time dt is $(Ng\, dt)$, where g is the rotor transmission. g is averaged over time.

Using the expressions found for the second moments of the transmission function, and remembering that $\tau_2 = \tau - Rn$, the following expressions are

found for δt, δn and g.

$$\delta t = \frac{1}{2\sqrt{6}} s p n_0 \qquad (3.1)$$

$$\delta n = \frac{1}{2\sqrt{2}} \frac{sp}{R} n_0 \qquad (3.2)$$

$$g = \frac{As^2 p}{4\pi R^2} n_0 \qquad (3.3)$$

where A is the total cross sectional area of the slots in the rotor.

Values of these quantities are listed for three rotors which have been used by the Cambridge Slow Neutron Group.

Table 3.1: Rotor Parameters

Rotor	p	s (ins)	R (ins)	A (ins^2)	$\delta t/n_0$ (cms)	$\frac{\delta n}{n_0}$	g/n_0 (cms^2)
1	4	.5	5	1.25	1.04	.14	.026
2	4	.25	5	.563	.52	.071	.0029
3	3	.1	4	1.15	.156	.0265	.00115

Rotor 1 was used by Collins (1961) and Dolling (1961) in their experiments on magnesium and silicon, rotor 2 by myself in the experiment on lead (Chapter 5), and rotor 3 by Sinha and myself in experiments on copper and magnesium oxide.

Marseguerra and Pauli (1959) have calculated the transmission of a curved slot rotor, assuming the slot to be parabolic. Their results differ little from the present ones. Their transmission function is shown in the following diagram in our notation.
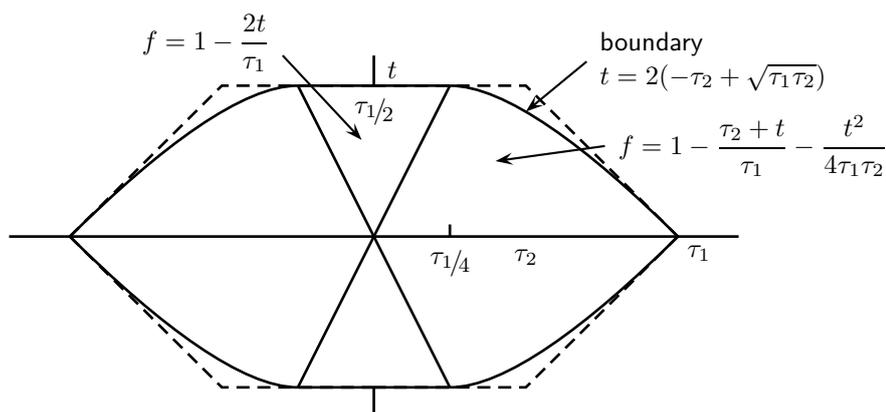
Figure 3.13: Marseguerra and Pauli rotor transmission function

The only difference is seen to be the addition of the extra term to one of the expressions for f and consequent slight changes in the boundaries of the

function. The total transmission is now $\tau_1^2/2.12$ instead of $\tau_1^2/2$, and, as a function of τ_2, the second moment is $\tau_1^2/8.25$ instead of $\tau_1^2/8$.

3.4 The Time Spread at the Sample

Let the time of arrival of the neutron at the sample be t_1, and the distance from the centre of the rotor to the sample be d. With our previous notation,

$$t_1 = t + \frac{d}{R}\tau_2$$

If the distribution of neutrons at the sample is $h(\tau_2, t_1)$,

$$h(\tau_2, t_1) = f(\tau_2, t)$$

The second moment of the time distribution at the sample is

$$(\delta t_1)^2 = \frac{\iint_{-\infty}^{\infty} t_1^2 h(\tau_2, t_1)\, d\tau_2\, dt_1}{\iint_{-\infty}^{\infty} h(\tau_2, t_1)\, d\tau_2\, dt_1}$$

$$= \frac{\iint_{-\infty}^{\infty} (t + \frac{d}{R}\tau_2)^2 f(\tau_2, t)\, d\tau_2\, dt}{\iint_{-\infty}^{\infty} f(\tau_2, t)\, d\tau_2\, dt}$$

$$= \frac{\tau_1^2}{24} + \left(\frac{d}{R}\right)^2 \frac{\tau_1^2}{8} + \frac{\iint_{-\infty}^{\infty} \frac{2d}{R} t\tau_2 f(\tau_2, t)\, d\tau_2\, dt}{(\tau_1^2/2)}$$

The last integral is zero as f is symmetrical about the axes. In fact we could have treated the time spreads at the sample due to the velocity spread, and due to the time spread at the centre of the rotor, as being independent.

Hence $\quad (\delta t_1)^2 = \frac{\tau_1^2}{24}\left(1 + 3\left(\frac{d}{R}\right)^2\right)$

or $\qquad \delta t_1 = \frac{spn_0}{2\sqrt{6}}\sqrt{1 + 3\left(\frac{d}{R}\right)^2}$ (3.4)

d/R must be greater than 1 for physical reasons, hence the part of t_1 due to velocity spread is always dominant. In a practical case, d/R is likely to be about 2, when the part of t_1 due to time spread at the rotor centre is only 5.9% of the whole. The transmission of the rotor could therefore be considerably improved by increasing δt, the time spread at its centre, without appreciably increasing δt_1, as the transmission is proportional to δt. Unfortunately, for a single rotor, δt can only be increased for a given δn by increasing the rotor radius. Little is to be gained from this, however, as the sample is then forced further from the rotor centre, the ratio d/R is not appreciably reduced and the fraction of δt_1, due to the time spread at the rotor centre is not significantly increased. This situation can be improved by the use of twin rotors. With such an arrangement it is possible to obtain increased transmission for the same velocity resolution (Cocking, 1960).

Some improvement is possible with a single rotor by the use of a beryllium filter to reduce the velocity spread δn without affecting δt. If the rotor is run

at such a speed that the best transmitted neutron energy coincides with the beryllium out off, δn is given by

$$\delta n = \frac{\sqrt{23}}{24} \frac{sp}{R} n_0 \tag{3.5}$$

and the corresponding formula for time spread at the sample is

$$\delta t_1 = \frac{spn_0}{2\sqrt{6}} \sqrt{1 + 0.942 \left(\frac{d}{R}\right)^2} \tag{3.6}$$

If this sample time spread were achieved by reducing the rotor slot width instead of by using a filter, the transmission would be only 0.735 of that of the filter-rotor system, and the velocity spread would be 1.07 times greater (this assumes $d/R = 2$). It might be argued that the filter transmission offsets this gain, but even if the filter cut off is not used to reduce δn, the filter is necessary to remove fast neutrons from the beam which would otherwise be a troublesome source of background counts in the detectors.

3.5 Resolution of the Apparatus

The cross section for one phonon coherent scattering contains delta functions of both energy and momentum. This is due to the fact that this cross section was derived using the harmonic approximation. In higher order approximations, the phonons are allowed to interact with each other and with imperfections in the crystal. The delta functions then broaden and have a finite width inversely proportional to the lifetime of the phonon. The peak we observe in the time of flight spectrum has the natural line shape of the phonon convolved with the various resolution functions of the apparatus.

If the observed number of neutrons as a function of time is $p(t)$, we may write

$$p(t) = \iiint \cdots \int p_1(t_1) p_2(t_2 - t_1) p_3(t_3 - t_2) \ldots p_n(t - t_{n-1}) \, dt_1 \ldots dt_{n-1}$$

where $p_1(t)$ is the distribution which would be observed in the absence of all resolution broadening, $p_2(t)$ the distribution if the spread in incident wave vector were the only cause of broadening, etc. Let us define a resolution width r by

$$r^2 = \frac{\int_{-\infty}^{\infty} (t - \bar{t})^2 dt}{\int_{-\infty}^{\infty} p(t) \, dt}$$

where $\bar{t}$ is the mean of $p(t)$. If r_i is similarly related to $p_i(t)$, it can be shown that

$$r^2 = \sum_i r_i^2 \tag{3.7}$$

The number of neutrons observed in a peak in a given time is proportional to the product of powers of the resolution widths. For example the intensity is proportional to the counter area and so is proportional to the width multiplied by the length, or to the diameter squared

$$I = \prod_i (r_i)^{\alpha_i} \tag{3.8}$$

We wish to obtain the maximum intensity I for a given overall resolution r. Introducing the Lagrange multiplier λ, we must maximise

$$\prod_i (r_i)^{\alpha_i} + \lambda \left(\sum_i r_i^2 - r^2 \right)$$

with respect to the r_j,

whence $\quad \dfrac{\alpha_i}{r_j} I + 2\lambda r_j = 0$

or $\qquad\qquad r_j \propto \sqrt{\alpha_j}$ $\hfill$ (3.9)

when the resolution widths are proportioned according to this relation, we shall say that they are balanced. we shall now calculate the ratio of the intensity obtained with one resolution width out of balance to that obtained with all widths balanced and the same overall resolution. This will indicate how accurately resolution widths should be balanced in practice.

(a) Balanced resolutions

From equation 3.9, $r_i \propto \sqrt{\alpha_i}$ $\hfill$

Put $\quad r_i = r_0 \sqrt{\alpha_i}$

The overall resolution, r, is given by

$$r^2 = r_0^2 S$$

where $S = \sum_i \alpha_i$, and the intensity, I_0, by

$$I_0 = r_0^S \prod_i \alpha_i^{\alpha_i/2}$$

(b) One resolution out of balance

Assume that we have

$$r_i = r' \sqrt{\alpha_i} \qquad\qquad \text{for } i \neq 1$$

where r' is a constant, and

$$r_1 = p\, r' \sqrt{\alpha_1} \qquad\qquad \text{where } p \neq 1$$

The overall resolution, r, is given by

$$r^2 = r'^2 \left(S + (p^2 - 1)\alpha_1 \right)$$

and the intensity, I', is given by

$$I' = p^{\alpha_1} r'^S \prod_i \alpha_i^{\alpha_i/2}$$

Comparing these with the equations for balanced resolutions,

$$\left(\frac{r'}{r_0}\right)^2 = \frac{1}{1 + \frac{\alpha_1}{S}(p^2 - 1)}$$

and the ratio of the intensities is

$$\frac{I'}{I_0} = p^{\alpha_1}\left(1 + \frac{\alpha_1}{S}(p^2 - 1)\right)^{-\frac{S}{2}}$$

Put $p = 1 + q$ and expand the above equation in powers of q

$$\frac{I'}{I_0} = 1 - \alpha_1\left(1 - \frac{\alpha_1}{S}\right)q^2 + \cdots$$

For the present experiment, considering time spreads at the sample, $S = 6$, and the following values are obtained for I'/I_0:

Table 3.2: The Effect of Unbalanced Resolutions on the Intensity

α_1	p	I'/I_0
1	1 ± 0.25	0.95
1	0.31	0.5
1	2.2	0.5
2	1 ± 0.25	0.92
2	0.44	0.5
2	2.0	0.5

It is seen that the intensity does not change appreciably if one resolution width is allowed to become more or less than the others by about $1/4$, but no $\left(r_i/\sqrt{\alpha_i}\right)$ should be greater than twice the others if an appreciable loss of intensity is to be avoided.

The following table shows the various contributions to the spread in the time at which neutrons are scattered by the sample (δt). This time spread limits the accuracy with which the time of flight of the scattered neutrons can be measured. Contributions to spreads in the incident wave vector components are also shown (δk_{0x}, δk_{0y}, δk_{0z}). α has the same significance as in the above analysis.

The effects of the rotor slot width and of the beam width were calculated using equations 3.5, 3.6 and II.2 with $d/R = 2.2$. The time spread due to the sample diameter assumes a scattered neutron inverse velocity of 400μ secs/m, but is not very sensitive to this value as incident neutrons are slower and most of the time spread is due to the time it takes an incident neutron to traverse the sample. The time at which the rotor allows a neutron to pass depends on the direction from which it approaches, and so the collimation of the incident beam in the horizontal plane contributes to the time spread. The incident beam collimation was calculated from the size and position of the liquid hydrogen source.

If the contributions to the time spread were exactly balanced, each $\delta t/\sqrt{\alpha}$ would equal 3.76 for the same overall resolution. From equation 3.8, we find

29

Table 3.3: Contributions to the Resolution of the Apparatus

		α	δt (μ secs)	$\delta t/\sqrt{\alpha}$	δk_{0x}	δk_{0y} (Å^{-1})	δk_{0z}
Incident beam collimation	horizontal .40°	1	2.3	2.3			.0017
	vertical .36°	1				.0015	
Rotor slot width .1″		2	3.8	2.7	.0037		
Beam width (effect of off centre slots)	2″	1	2.9	2.9	.0031		
Sample diameter	2.4 cms	2	7.6	5.4			
Total			9.2		.0048	.0015	.0017

that the intensity obtained with the resolution widths in the table is 0.50 of the intensity in this ideal case. This reduction in intensity is almost entirely due to the time spread caused by the sample diameter being out of balance. However, the incident beam collimation could not conveniently be changed, and changes in the rotor parameters and in the sample size could only be made by using different rotors or samples and the alternatives were grossly different from those used. The balance of resolutions achieved was therefore considered to be satisfactory.

The uncertainty that the time spread at the sample introduces into the measurement of the scattered neutron energy depends on the length of the flight path to the detectors. This flight path should be long enough to make the uncertainty in the scattered neutron wave vector at least as small as that in the incident wave vector. The angle subtended by the detectors at the sample should also give uncertainties in scattered wave vector of the same order. Two factors limit the length of the flight path. The further the detectors are from the sample, the larger area they must have to subtend the same angle at the sample, and consequently the greater the background count rate will become. The flight path should not be so great that the fastest neutrons from one burst can overtake the elastically scattered neutrons from the previous burst.

The resolution widths in scattered wave vector are summarised in the following table for two scattered wave vectors corresponding to typical phonon energies in magnesium oxide. (In these tables, the incident beam is in the direction of the X axis, and the scattered beam is assumed to be in the direction of the Y axis).

Table 3.4: Resolution of the Scattered Neutron wave Vector

Incident beam energy spread .046 × 10^{12} c/sec					
Phonon frequency for overlap 81 × 10^{12} c/sec					
Phonon freq. (c/s)	k_1(Å^{-1})	δE_1 (10^{12}c/s)	δk_{1x}(Å^{-1})	δk_{1y}(Å^{-1})	δk_{1z}(Å^{-1})
5 × 10^{12}	.559	.11	.0060	.0049	.0060
10 × 10^{12}	.752	.26	.0081	.0088	.0081

In this table, k_1 is the scattered neutron wave vector, δE_1 is the spread in energy of the scattered neutrons, and δk_{1x} etc. are the spreads in scattered neutron wave vector components.

It is seen that the spreads in scattered neutron energy and wave vector are larger than the spreads in incident neutron energy and wave vector. A longer flight path, therefore, could profitably have been used. However a longer flight path would have resulted in danger of overlap of the neutron bursts, and since the only place there was room to mount the detectors was above the sample, a very large and expensive tower would have been necessary to support the detectors and shielding.

The overall energy resolution of the apparatus is shown in fig. 3.14 as a function of phonon frequency. The population factor, P_j, in the cross section formula 2.3 is also shown. The apparatus is useful in a range of phonon frequencies from about 1.0×10^{12} c/sec to 14×10^{12} c/sec. The lower limit is set by the rapid deterioration in the resolution due to the incident beam energy spread, and the upper limit by the falling off of the population factor P_j.

The overall resolution of the apparatus for phonons of frequency 10×10^{12} c/sec is found to be 2.6% in energy, and 0.0089 Å^{-1} in wave vector (averaging over the three components). The radius of the Brillouin zone of MgO is 0.238 Å^{-1}, and the wave vector resolution is 3.7% of this. It should be possible to measure energies and wave vectors more accurately than this as the resolution determines the width of the peak in the time of flight spectrum, and it is possible to fine the mean of the peak with an error considerably less than the width of the peak.

The spread in $\boldsymbol{k}_0$ causes a spread in $\boldsymbol{k}_1$ depending on the gradient of the dispersion relation. This spread may add to or subtract from the resolution spread already calculated. For instance, neutrons incident on the sample with greater velocity than average arrive earlier. If these neutrons after scattering have less than the average scattered velocity, they will take longer to reach the detector and may in fact arrive at the same time as average neutrons which were scattered later. This is a focussing effect and would reduce the width of the peak in the time of flight spectrum. Obviously, if the dispersion relation were estimated before the experiment, we could make use of this effect to improve the resolution. However, the apparatus would only be focussed for one angle of scatter and since twelve detectors were used it was not considered worth while to try to focus the peaks.

3.6 Optimum Detector Efficiency

Near a reactor there is always a considerable flux of fast neutrons, some of which will penetrate the shielding around the detectors and give rise to a back-

ground count rate. The detector is thin to this fast neutron background, i.e., if the detector thickness is doubled, other factors remaining the same, the number of fast neutrons detected will also be doubled. However, we wish to detect thermal neutrons, and if the detector efficiency were already 90% for thermal neutrons, doubling its thickness would increase its efficiency to 99%. We have then doubled the background count rate for a marginal (10%) increase in the number of thermal neutrons detected. There is an optimum detector efficiency which is less than 100% due to the presence of this fast neutron background. The criterion which determines this optimum efficiency may be obtained by considering features in a time of flight spectrum which are only just distinguishable from the background. The same criterion is obtained in two different ways.

We accept the presence of a feature in a time of flight spectrum only if the feature is large compared with the fluctuations in the background. If the feature contains N counts, and the background under it contains B counts, the fluctuations in the background are proportional to $\sqrt{B}$ and the feature is accepted only if $N/\sqrt{B} > g$ where g depends on the degree of certainty we require. we should then choose our detector efficiency to maximise $N/\sqrt{B}$.

We may obtain the position of such a feature by first subtracting a smoothed background, and then taking the mean time of flight. If the second moment of the feature is σ^2, and we take the mean over a range of time 3.5σ, it can be shown that the standard deviation of the mean is $(\sigma^2/N + B\,\sigma^2/N^2)^{1/2}$. In the case of a small feature on a large background ($B \gg N$), this reduces to $\sqrt{B}\,\sigma/N$. To obtain the positions of these small features most accurately, we should again choose our detector efficiency to maximise $N/\sqrt{B}$.

The efficiency of a detector for thermal neutrons is $(1 - e^{-x})$ where x is proportional to the detector thickness. Its efficiency for fast neutrons is γx, where γ is the ratio of fast neutron to thermal neutron cross section. To satisfy either of the above criteria, we must maximise $N/\sqrt{B}$ or $(1 - e^{-x})/\sqrt{x}$ This leads to the equation $2x + 1 = e^x$, the solution of which is $x = 1.256$, corresponding to a detector efficiency for thermal neutrons of about 72%. This maximum is not very sharp. Over a range of efficiencies from 44% to 92%, the value of $N/\sqrt{B}$ does not fall below 90% of its maximum.

It is seen that the detector efficiency is not critical, but if we are interested in features in the time of flight spectrum near the background level, the efficiency should be in the range 40 to 90%. In practice it is difficult to obtain detectors with an efficiency of more than 40 or 50% for thermal neutrons and insensitive to γ radiation.

3.7 Choice of Detector

There are two main types of detector for thermal neutrons: the BF_3; proportional counter and various types of scintillator. Each type has advantages and disadvantages in use.

BF_3 proportional counter

Advantages–

The detector is insensitive to γ radiation.

The E.H.T. voltage and the discriminator setting are not critical, and it is easy to determine the correct values.

BF$_3$ counters and the equipment to run them are readily available at Harwell.

Disadvantages–

For reasonable efficiency the detector has to be so thick that the time of flight resolution is poor. For example, a 9EB70 detector side on to the beam has an efficiency of 17% to thermal neutrons, and a thickness of 2.54 cms. The same detector used end on has an efficiency of 49%, but the thickness is now 9 cms, or about 4% of the flight path.

BF$_3$ counters are available only in the form of cylinders 1 or 2 in in diameter and of various lengths. It is often difficult to arrange the detectors to cover a given area and no more. If the detector is masked with cadmium to reduce the area to that desired, the background is not reduced in proportion. '

Scintillators

Advantages–

A scintillator can be made with an efficiency of 40 or 50% and a thickness of only a few millimetres.

A mask may be placed between the scintillator and the photomultiplier tube to reduce the area of the detector, or the scintillator may be cut to any desired shape.

Disadvantages–

Scintillators are more sensitive to γ radiation than BF$_3$ counters. Some types are so sensitive that they cannot be used in the high energy γ flux near a reactor.

The E.H.T. voltage on the photomultiplier tube, and the discriminator setting must be very near the optimum values to discriminate against the γ rays.

It is seen that a scintillator has much to recommend it if it can be made sufficiently insensitive to γ radiation.

Tests of Scintillators

Our first tests on scintillators in the conditions in which they were to be used were disappointing. A comparison was made between a lithium glass scintillator, a lithium iodide scintillator and a BF$_3$ proportional counter. The detectors were mounted in neutron shielding consisting of 1 ft. thick tanks of water lined with a 5 in. pocket containing borax powder. When using scintillators it is preferable to absorb neutrons in boron rather than cadmium, as the scintillator may detect the high energy γ ray emitted by cadmium on absorbing a neutron. The assembly was placed about 5 ft. from the DIDO reactor face. No attempt was made to shield the detectors against γ radiation. A kicksorter was used to obtain a pulse height spectrum from each detector. Fig. 3.15 shows the pulse height spectra obtained from background alone (full line), and with a Po–Be neutron source placed inside the shielding near the detectors (broken line where this differs from the full line). Also shown is the spectrum obtained from the scintillator detectors when a Co$^{60}\gamma$ source was placed near them. This has been reduced in scale.

Optimum discriminator levels (both upper and lower for the scintillators) have been determined from the pulse height spectra, and counts to background ratios calculated for each detector.

Table 3.5: Counts to Background Ratios for 3 Types of Detector

Type of detector	Counts / background
Lithium glass scintillator (1/8 in thick)	0.4
Lithium iodide scintillator	1
BF_3 proportional counter	16

The BF_3 proportional counter is seen to have a very much higher counts/background ratio than either of the scintillators, and was accordingly chosen as the most suitable detector for our first experiment. It is seen that the γ ray cut off in the pulse height spectrum is well below the pulse heights given by the more energetic γ ray background near the reactor. The performance of scintillators in discriminating against γ rays from a Co^{6O} source is accordingly a poor guide to the performance of such a detector in the conditions encountered near a reactor.

Two designs for banks of BF_3 counters are shown in fig. 3.16. The first consisted of 7 9EB7O counter tubes placed end on to the incident neutrons. Detectors of this type were used in the lead experiment. The efficiency for the detection of thermal neutrons was 49%, but the active length of 9 cm gave poor time of flight resolution. The second design was intended to reduce this active length. 3 9EB7O counter tubes were placed side on to the incident neutrons. The electrical components and the ends of the counter tubes were encased or potted in Araldite resin to make a very compact assembly. The detectors could be double banked, the pulses from the front bank being delayed to improve the time of flight resolution. The efficiency of the double bank for the detection of thermal neutrons would be 50%. Some trouble was experienced with the potted electrical circuit, and, before this was corrected, we had obtained a satisfactory scintillator. The potted counter assembly accordingly was never used.

Sun et. al. (1936) describe a scintillator which consists of a boron-containing plastic mixed with zinc sulphide. Stedman (1960) has more recently developed a similar type consisting of lithium fluoride enriched in Li^6, again mixed with zinc sulphide. Both these types give good neutron detection efficiency with low sensitivity to γ radiation. Furthermore, γ rays give a very much shorter pulse than neutrons, and various electronic circuits are available to make use of this fact in discriminating against γ rays. We used a circuit developed by Wraight (1964). A discussion of the merits of various types of scintillator is Given by Harris, Wraight and Duffil (1962).

Tests of a LiF–ZnS scintillator supplied by Harris showed that it had a similar efficiency and background count rate to the BF_3 proportional counters we were then using, and was thin enough to give a negligible contribution to the time of flight resolution width. It was therefore decided to adopt this type of detector. We were able to obtain these scintillators commercially from Nuclear Enterprises (type NE42l). The detector units containing a scintillator, photomultiplier tube and pulse shape discriminator are shown in fig. 3.16. Three such units were in use for the first part of the magnesium oxide experiment, but the counter shielding was subsequently extended to take the twelve units used in the second part of the experiment.

A lithium glass scintillator detector has a very well defined plateau in its

discriminator bias curve and forms a convenient absolute standard for detector efficiency measurements. The absorption of the glass is assumed to equal its efficiency as a detector. A crystal spectrometer on the BEPO reactor provided a beam of neutrons of wavelength 1.7 Å(thermal energy). The absorption of the lithium glass was found to be 77%, and by comparing the count rates given by the lithium glass detector and by one of the LiF–ZnS detectors when each in turn was placed in the beam, the efficiency of the LiF-ZnS detector was calculated to be 45%. No allowance has been made for second order contamination of the neutron beam, which might reduce this calculated efficiency by a small amount.
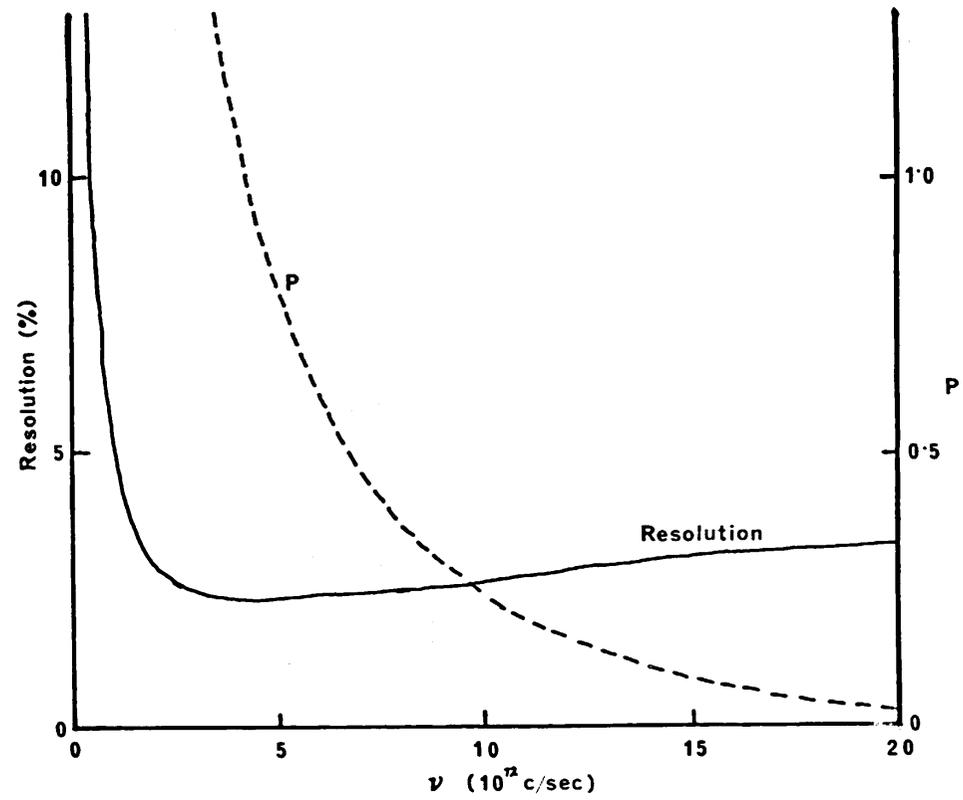
Figure 3.14: Energy resolution and population factor (P) as functions of phonon frequency (ν)
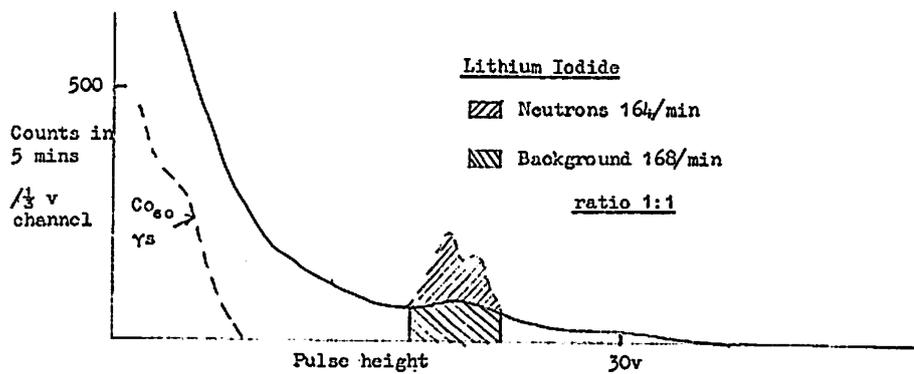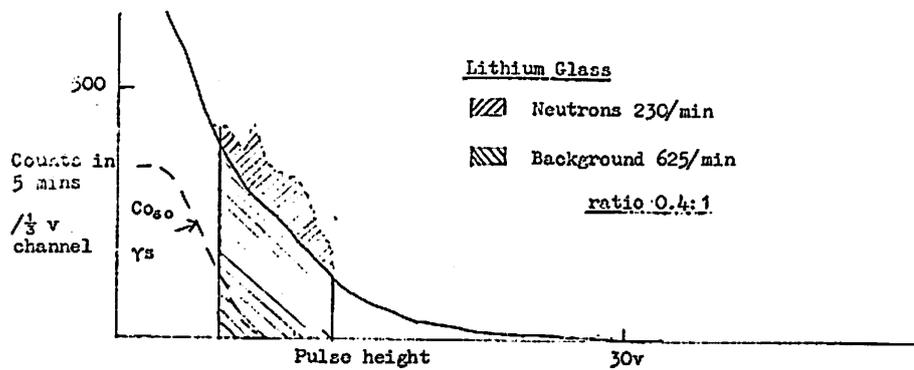
Scintillators in Dido

Figure 3.15: Scintillators in DIDO

DETECTOR 1
(COVER REMOVED)

DETECTOR 3
(SECTION)

E.H.T.
DECOUPLING
CIRCUIT

PULSE SHAPE
DISCRIMINATOR

PHOTOMULTIPLIER
TUBE

7 BF_3 COUNTER
TUBES
TYPE 9EB70/G

LiF–ZnS
SCINTILLATOR

ALUMINIUM
WINDOW

DETECTOR 2

E.H.T.
DECOUPLING
CIRCUIT
POTTED IN
ARALDITE
RESIN

2 ins
SCALE

3 BF_3 COUNTER TUBES
TYPE 9EB70/G
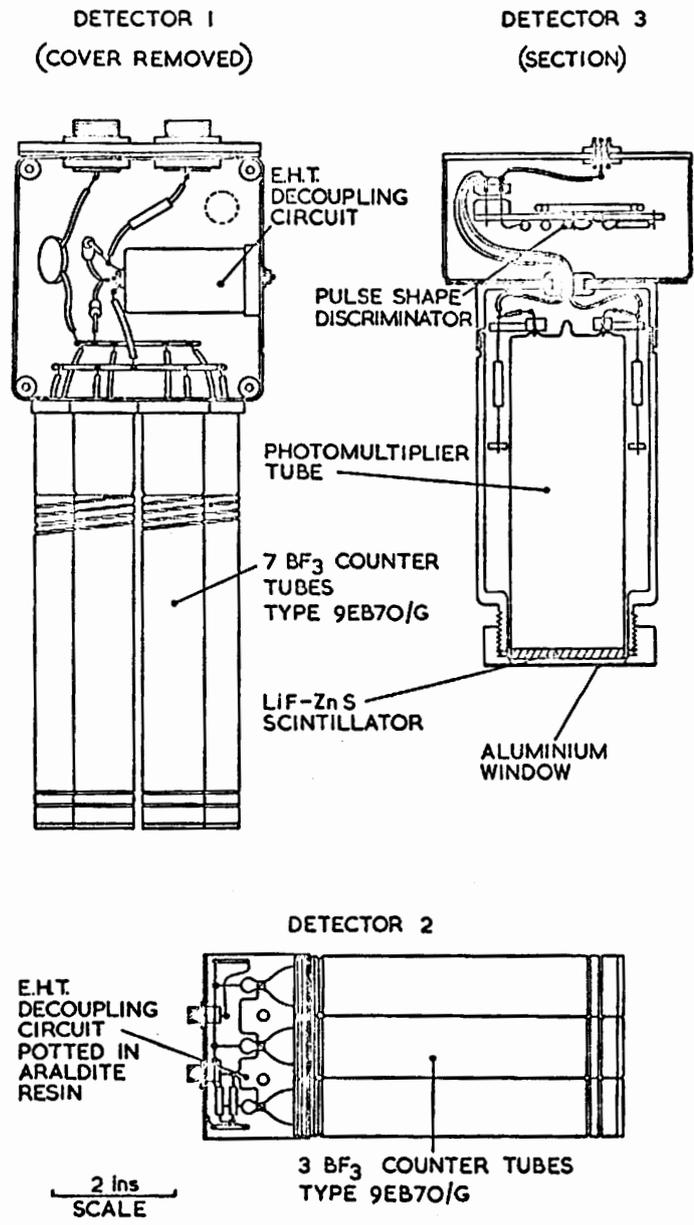
Figure 3.16: Neutron detectors

38

Chapter 4

Data Processing

4.1 Introduction

One of the advantages of the time of flight method is that many detectors may be used to observe the scattering from a sample at many different angles simultaneously. We used 12 detectors mounted in the vertical plane containing the sample. Modified kicksorters have been used to record time of flight spectra from single detectors. However, it would have been a very expensive solution to the problem to have used 12 kicksorters to record the time of flight spectra from our 12 detectors. The kicksorter is essentially a one parameter recorder, i.e., it classifies the pulses from the detector according to a single criterion. A far more economical solution was to use a magnetic tape recorder, which could record two parameters for each pulse as it arrived, namely, its time of arrival and
the identity of the detector concerned. Subsequently the tape was analysed by passing it many times through a one parameter analyser, each pass producing a time of flight spectrum for a particular detector. The analyser could read the tape at about 100 times the recording speed.

Because of the heavy demand for time on the Cold Neutron Apparatus, it was run continuously day and night. We designed and built a goniometer and control units which automatically changed the crystal orientation after a pre-set number of beam monitor counts had been accumulated. Many angles could be programmed in advance, so that the experimenter had only to intervene every 48 hours to change the magnetic tape.

Computer programmes were written to determine points on the phonon dispersion relation from the spectra produced by the time of flight analyser. The I.B.M. 7090 programme *Fit and Search* found peaks in the time of flight spectra and estimated their position. The Ferranti Mercury programme *Phonon Reduction* determined the energy and wave vector of a phonon from the peak position given by *Fit and Search*. Fig. 4.1 shows the various stages in the analysis of the data from the detection of the neutrons to the deduction of points on the
phonon dispersion relation.

4.2 Time of Flight Recorder

The time of flight recorder (Hall, 1959) contained a crystal oscillator driving scaling circuits which were started from zero on receipt of a start pulse derived from the rotor. When a neutron was detected, the scaling circuits were stopped and they then indicated the time of arrival of the neutron at the detector. This time was recorded on 1 inch magnetic tape together with a number identifying the detector. A single line was recorded across the 16 tracks on the tape as
follows: A record in track 10, the clock track, indicated to the analyser that the other tracks contained information and were to be read. Pulses from the beam monitor were recorded in track 16 and, in the event of failure of the apparatus, could show where this occurred on the tape. Track 15 is normally
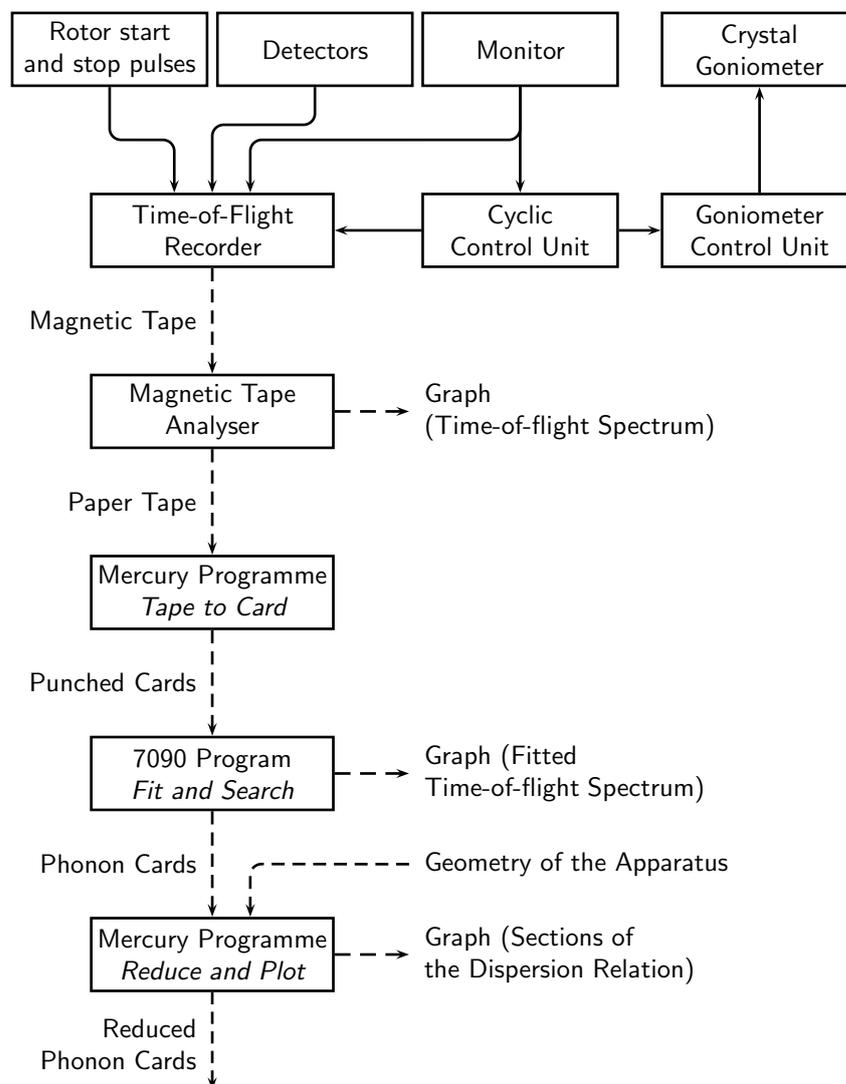
Figure 4.1: The data reduction scheme

used to record the most significant digit of the detector address, but as we used only 12 detectors, 4 digits were sufficient for this address and track 15 was used to separate adjacent recordings made with different crystal orientations.

Only the first neutron to arrive after a start pulse was recorded. This meant that there were fewer counts in the later time channels than there would have been had all counts been recorded. The effects of this on the area and mean of a peak can be shown to be negligible for the count rates we experienced. If the peak is at time t after the start pulse, its width is σ, and the total count rate in all detectors is c, an order of magnitude calculation shows that the area of the peak is reduced by a fraction ct, and its mean is altered by $c\sigma^2$. In our

40

Table 4.1: Contents of the Tape Tracks

Track	Content	
1	2^8	
$\vdots$	$\vdots$	Time channel number
9	2^0	
10	Clock	
11	2^0	
$\vdots$	$\vdots$	Detector address
14	2^3	
15	Crystal angle	
16	Monitor	

experiment, c was of order 10 counts per second, the maximum value of t was about 2,100 μ secs, and σ was about 20 μ secs. The reduction in area was then not more than about 2%, and the change in the mean was of order 0.0002σ.

The 9 tracks allocated to the time channel number allowed up to 512 time channels to be used. However, the counting statistics and resolution of the apparatus did not warrant the use of this many time channels. We used time channels 8 μ secs wide. The rotor period was 2120 μ secs, but the tape recorder was reset by a stop pulse occurring about 20 μ secs before the start pulse. We thus used 262 time channels, leaving 24 μ secs dead time before the next start pulse.

The start and stop pulses were generated by a magnetic shim attached to the rotor shaft passing close to stator pickup coils. The stator could be rotated about the shaft to change the phase of these pulses with respect to the neutron burst passing through the rotor. Beam monitor 1, placed between the rotor and the sample, was used to determine the time of arrival of the neutron burst. As was explained earlier, there was a dead time of 24 μ secs between the end of the last time channel and the start of the first. It was desirable that this

dead time should occur outside the range of time in which phonon peaks would be observed. The start pulse was so phased that elastically scattered neutrons would arrive at the detectors in the last few time channels. Neutrons which had gained energy by interaction with a phonon would arrive earlier than this and so would not arrive during the dead time.

A second monitor was placed in the beam about 1.5 metres beyond the sample. The outputs from both beam monitors were time analysed during the experiment. The time zero correction necessary to convert time channel number into time of flight from the sample to the detector and the mean incident neutron velocity were determined from the monitor time of flight spectra.

4.3 Crystal Goniometer and Control Units

We wished to determine the phonon dispersion relation in a mirror plane of the crystal. The crystal was held in a goniometer which was adjusted so that this plane coincided with the plane of scattering. Measurements were made with the crystal at various orientations about an axis perpendicular to the plane of

41

scattering. The goniometer was rotated about this axis by an electric motor controlled from the Programming Unit. The angles required were set up on a patchboard, and the goniometer was moved on to the next position on receipt of a signal from the Cyclic Control Unit.

The Cyclic Control Unit is designed to control any sample changing mechanism. It allows up to four different samples to be placed in the beam one after the other for short periods, repeating the cycle indefinitely for the duration of the experiment. The Cyclic Control Unit also controls recording on track 15 of the tape recorder, or on both tracks 15 and 14 if more than 2 samples are used. The number recorded in these tracks identifies the particular sample in the beam and allows the results for different samples to be separated on analysing the tape. The sample is changed after a pre-set number of beam monitor counts have been received.

In our case, the Cyclic Control Unit changed the digit recorded in track 15 each time the orientation of the crystal was changed. This made it easy to separate adjacent recordings when the tape was analysed.

The goniometer and its control units are described fully elsewhere (Peckham, 1964 b and c).

4.4 The Magnetic Tape Analyser

The magnetic tape analyser produced the time of flight spectra punched on paper tape as octal based numbers. The mercury computer was used to transform these numbers to decimal form, and to punch them on cards which could be listed to obtain the time of flight spectra. The analyser also produced graphs of the time of flight spectra which provided a valuable check on the correct functioning of the equipment.

4.5 The Computer Programme 'Fit and Search'

We were producing about 18 time of flight spectra a day and to examine each spectrum by hand would have been extremely laborious. It was considered desirable to use a definite statistical criterion to decide whether a particular group of time channels contained more neutrons than could be accounted for by background alone. Also we required the mean of a peak and not its maximum or other simply observed feature. By using the mean peak position, mean incident wave vector, mean counter angles etc, we obtained an answer correct to first order. That means we ignored the curvature of the scattering surface over the angle subtended by the counter, for instance, and the change in cross section over this angle. A computer programme was written which automatically searched for peaks which were statistically significant and estimated their means.

This programme originated as a technique for obtaining the positions of peaks which considerably overlapped each other. The time of flight spectrum was assumed to consist of Gaussian peaks on a flat background and the parameters of the Gaussian were adjusted to minimise the weighted square deviations from the observed spectrum. Perhaps the use of Gaussians needs some justification. The peak we observed had the natural line shape of.a phonon convolved with all the various resolution functions of the apparatus. For instance, if the probability of a neutron arriving at the centre of the sample at time t is $p(t)$ and if the probability of it then being scattered at time $t'' = t + t'$ is $q(t')$ (depending on the size and shape of the sample), then the probability of any neutron being

42
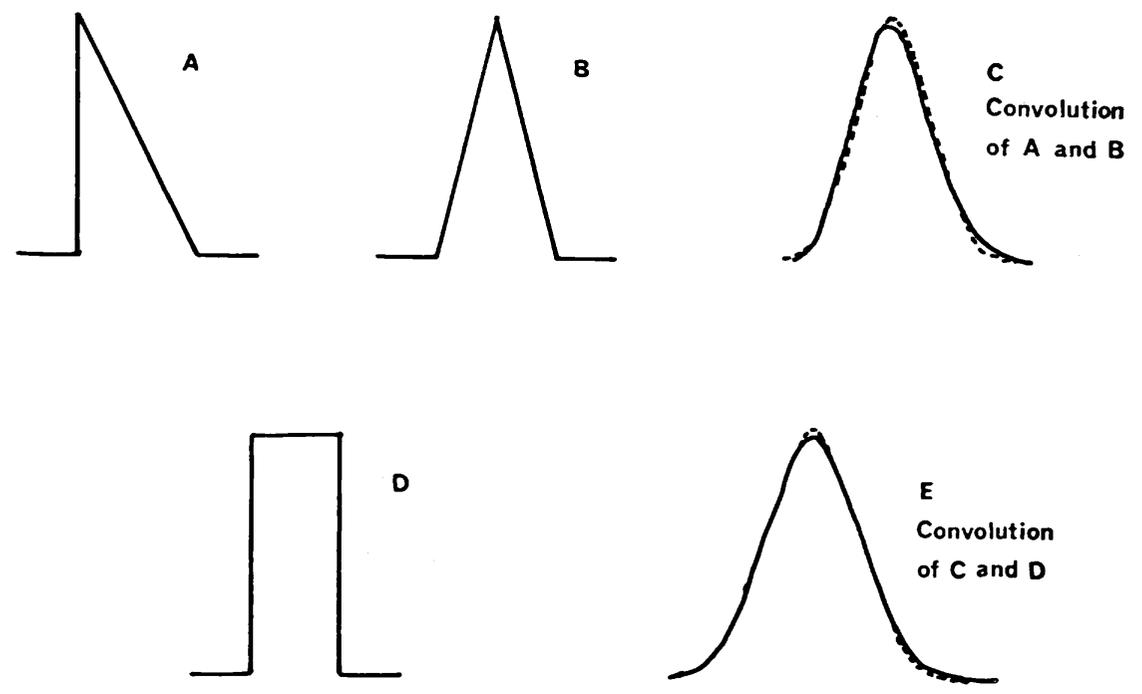
Figure 4.2: Convolutions

scattered at time t'' is $\int_{-\infty}^{\infty} p(t)q(t'' - t)\,dt$; i.e., the convolution of p and q. The more functions we convolve together, in general the nearer we get to a Gaussian shape. The central limits theorem of statistics bears on this, but the rapidity with which this occurs is best seen by an example. In fig.4.2 the solid curve C has been obtained by convolving curve A with curve B. The dotted curve U is a Gaussian of the same area, mean and second moment as the solid curve. It is seen that little of the asymmetry of curve A remains. C is again convolved with D to give E and the difference from a Gaussian shape is seen to be very small. This, of course, would not happen so quickly if the curves were not of similar width. However, the resolutions of the apparatus have been carefully matched to optimise the count rate and we would therefore expect the observed peaks to be very close to Gaussian form. In practice a Gaussian was found to fit the peaks well (see fig. 7.1, the fitted spectrum is shown as a full line).

The fitted Gaussians performed a second duty in providing a theoretical time of flight spectrum which could be compared with the observed spectrum to check that no further peaks were present. The time channels were grouped, first in threes, then in sevens and fifteens, the groups being moved through the time channels in steps of 1, 3 or 7 channels at a time. In each position, the sum of observed counts in the group was compared with the sum of theoretical counts. If there were significantly more, the parameters of a new peak were estimated and the least squares fitting repeated with the extra peak. Since this involved perhaps 100 trials in each time of flight spectrum and there were several hundred time of flight spectra in the experiment, a group was only counted as significant if it could have arisen by chance with a probability of 1 in 10^5 or less. If the sum of theoretical counts was m, the sum of observed counts had to exceed $m + 4.27\sqrt{m} + 3.1$ to be significant on the above criterion. This formula gives the correct limit according to the Poisson distribution within ± 1 certainly in the range $1 \le m \le 1,000$.

The mean of the Gaussian was taken as the mean peak position. There are some difficulties in taking a true mean, such as the presence of background counts and the nearness of other peaks, but in several cases this was done and the true mean was found to agree with the Gaussian mean within the limits of statistical error. The programme *Fit and Search* accepted the time of flight cards from Mercury. Provision was made for the addition of runs or the grouping of time channels, and comprehensive checks were made to ensure that the correct time of flight cards had been used. Graphs of the fitted and observed time of flight spectra were produced and also one card for each peak bearing an identification number, the crystal goniometer setting, the peak position and width, the standard deviation the peak position and the relative intensity of the peak.

4.6 The Computer Programme 'Phonon Reduction'

From the peak positions, the frequencies and wave vectors of the phonons with which the neutrons interacted, could be deduced. This was conveniently done using another Mercury programme *Phonon Reduction*. Phonon wave vectors were reduced to the most elementary sector of the first Brillouin zone. This reduction was done using the two-dimensional lattice which is the section of the reciprocal lattice in the plane of scattering. The lattice was specified by generating vectors and the symmetry automatically determined by inspection of

these vectors. This programme accepted cards produced by *Fit and Search* and produced one card for each phonon bearing the identification number, intensity, unreduced wave vector, reduced wave vector, frequency and the standard deviations in these quantities. The Brillouin zone was also divided into narrow sectors and the frequency of phonons lying in each sector was plotted as a function of the wave vector amplitude to give a section of the dispersion relation. The velocity of sound was calculated and the corresponding straight line dispersion relation plotted in the region of the origin.

Only one error has been considered, that is the error in determining the position of the peak in the time of flight spectrum. However, if we write down estimates of the errors introduced by errors in other quantities, we see that this was the dominant error.

This is as it should be as these other quantities are measured much more easily than the peak position which needs perhaps a day of counting to determine it. It was not clear how these other errors should be treated, as quantities such as counter angle or incident wave vector were common to the whole experiment.

However inaccuracies in these quantities would give rise to scatter of the points

Table 4.2: Sources of Error

Source of error	error	Equivalent error in scattered wave vector
Incident wave vector	0.2%	0.1 %
Crystal angle	0.1°	0.17%
Counter angle	0.1°	0.17%
Counter distance	0.1%	0.1 %
Position of peak	3 μ secs	(Phonon freq. 10^{13} c/sec) 0.4 %
(A11 errors are standard deviations)		

on the dispersion relation through the reduction of the wave vector to the first Brillouin zone.

A distinction should be made between resolutions and errors. The above errors were the errors in determining the mean incident wave vector, the mean counter angle, etc. These were considerably less than the spread in incident velocities or the angle subtended by the counter at the sample, that is the resolutions of the apparatus. The resolutions introduce an error through the second order effects discussed earlier. This error is not treated here.

Since the errors in wave vector and frequency were assumed to arise from one error, they were closely correlated and the correlation coefficients were calculated. For example we may write

$$\delta q_1 = \frac{\partial q_1}{\partial t}\,\delta t$$
$$\delta q_2 = \frac{\partial q_2}{\partial t}\,\delta t$$

45

where δq_1 and δq_2 are errors in the components of the wave vectors arising from a time of flight error δt.

$$\delta q_1 \, \delta q_2 = \frac{\partial q_1}{\partial t} \, \frac{\partial q_2}{\partial t} \, (\delta t)^2$$

The correlation coefficient c_{12} is given by

$$c_{12} = \frac{\partial q_1}{\partial t} \, \frac{\partial q_2}{\partial t} \, \sigma^2 \qquad\qquad (4.1)$$

where σ is the standard deviation error in the time of flight.

An error was given in each quantity, e.g., the error in q_1 was $\frac{\partial q_1}{\partial t} \sigma$ and the various correlation coefficients could be found by multiplying them as in 4.1. This, of course, was only possible because all errors were assumed to arise from the one error, σ, in the time of flight.

Chapter 5

Phonon Dispersion Relation in Lead

5.1 Introduction

A preliminary experiment was performed to check the time it would take to accumulate sufficient counts from the detectors to define the positions of the peaks in the time of flight spectra. A low resolution rotor was used, but it was hoped that the results of this experiment would justify the use of higher resolution in future experiments. A single crystal of lead was used as the scattering sample. Lead has a high coherent neutron cross section and low incoherent and absorption cross sections, which makes it suitable for this type of experiment. However, the highest phonon frequencies are about 2×10^{12} c/sec, which is low compared with most crystals. This results in a low fractional accuracy in determining these frequencies.

The phonon dispersion relation largely agreed with that determined by Brockhouse et al. (1960) using a triple axis spectrometer. An analysis of the results was made by Squires. He found the values of the short range forces which gave a best fit to the measured frequencies by a least squares method. The experimental results have several serious shortcomings, but did indicate that the resolution of the apparatus could be increased without leading to prohibitively long counting periods.

5.2 Theory

Phonon dispersion relations in metals are frequently calculated on the assumption that the interatomic forces have a fairly short range. If one atom is taken as origin, the remaining atoms may be divided into orders such that all atoms in one order are equivalent in terms of the point group symmetry of the crystal. If the force constants for one atom in the order are known, those for the other atoms in the order are determined by symmetry. Arbitrary parameters are introduced to describe the most general forces consistent with the symmetry of the crystal. The elements of the dynamical matrix are calculated by means of equations 2.1. The arbitrary parameters may be chosen to be consistent with the elastic.constants, which may be shown to be linear combinations of the parameters. Before the advent of direct experimental methods for determining the dispersion relation, the number of parameters had to be restricted to the number of elastic constants. Now, however, more parameters may be used, and their values determined by fitting the calculated dispersion curve to the experimental data. The number of parameters rises rapidly as the range of the forces increases. This is shown in the following table for a crystal with the face centred cubic structure. Clearly, few experiments will justify an analysis of this type with forces extending beyond 5 or 6 orders. The most general force constant

Table 5.1: Number of Parameters in Force Constant Models for F.C.C. Crystals

Order	Type	Distance	No. of parameters	Total no. of parameters
1	(0, 1, 1)	$0.707\,a_0$	3	3
2	(0, 0, 2)	$1.000\,a_0$	2	5
3	(1, 1, 2)	$1.225\,a_0$	4	9
4	(0, 2, 2)	$1.414\,a_0$	3	12
5	(0, 1, 3)	$1.581\,a_0$	4	16
6	(2, 2, 2)	$1.732\,a_0$	2	18
7	(1, 2, 3)	$1.871\,a_0$	6	24
8	(0, 0, 4)	$2.000\,a_0$	2	26

matrices for the first 3 orders are given below..

$$
\begin{array}{cccc}
\text{Order} & 1 & 2 & 3 \\
\text{Matrix} &
\begin{pmatrix} \alpha_1 & 0 & 0 \\ 0 & \beta_1 & \delta_1 \\ 0 & \delta_1 & \beta_1 \end{pmatrix} &
\begin{pmatrix} \alpha_2 & 0 & 0 \\ 0 & \alpha_2 & 0 \\ 0 & 0 & \gamma_2 \end{pmatrix} &
\begin{pmatrix} \alpha_3 & \rho_3 & \delta_3 \\ \rho_3 & \alpha_3 & \delta_3 \\ \delta_3 & \delta_3 & \gamma_3 \end{pmatrix}
\end{array}
$$

A severe disadvantage of this method of analysis is that the dispersion relation is expressed in terms of a set of functions of the wave vector which are not orthogonal. This means that a final set of values for say the first order force constants cannot be determined from the experimental measurements because the values will vary depending on whether we allow forces to extend to 1, 2, 3, ... orders. Squires (1962) has commented on this difficulty in his analysis of Larsson's experiment on aluminium.

Foreman and Lomer (1957) have pointed out that the dispersion relation in symmetry directions can be expressed as a Fourier series, the coefficients of which can be identified with forces between planes of atoms:

$$
m\omega^2 = \Phi_0 + \sum_{n=1}^{N} \Phi_n \left(1 - \cos\left(n\pi \frac{q}{q_m} \right) \right)
$$

q_m is half the shortest distance between equivalent points in reciprocal space in the symmetry direction. The coefficients Φ_n are linear combinations of the interatomic force constants. The relationships are given by Squires (1963), table 4. The table is repeated here, as the force constants are differently defined (Table 5.2). In this table, lines one and two for instance, mean that, for the symmetry direction where q takes the form $(\xi, 0, 0)$ the coefficients for the longitudinal mode are given by

$$\Phi_1 = 8\beta_1 + 16\alpha_3 + \text{ terms from } 4^{\text{th}} \text{and higher orders}$$
$$\Phi_2 == 2\gamma_2 + 8\gamma_3 + \text{ terms from } 4^{\text{th}} \text{and higher orders}$$

A final set of values for these coefficients may be determined because the dispersion relation is now expressed in terms of orthogonal functions. The Φ_n give

an estimate of the range of the forces since distant planes of atoms contain only distant orders.

No satisfactory alternative to the force constant method has emerged for the analysis of experimental results in non-symmetry directions. This method, therefore, has been used with the present results.

Table 5.2: Relations between the Interplanar Force Constants and the Interatomic Force Constant

Branch		n	α_1	β_1	δ_1	α_2	γ_2	α_3	γ_3	δ_3	ρ_3
$(\zeta,0,0)$	L	1	–	8	–	–	–	16	–	–	–
		2	–	–	–	–	2	–	8	–	–
	T	1	4	4	–	–	–	8	8	–	–
		2	–	–	–	2	–	8	–	–	–
$(\zeta,\zeta,0)$	L	1	4	4	–	–	–	4	4	$\bar{8}$	–
		2	–	2	2	2	2	4	–	–	4
		3	–	–	–	–	–	4	4	8	–
	T_1	1	–	8	–	–	–	8	–	–	–
		2	2	–	–	4	–	–	4	–	–
		3	–	–	–	–	–	8	–	–	–
	T_2	1	4	4	–	–	–	4	4	8	–
		2	–	2	$\bar{2}$	2	2	4	–	–	$\bar{4}$
		3	–	–	–	–	–	4	4	$\bar{8}$	–
(ζ,ζ,ζ)	L	1	2	4	4	4	2	8	4	–	$\bar{8}$
		2	–	–	–	–	–	4	2	8	4
	T	1	2	4	$\bar{2}$	4	2	8	4	–	4
		2	–	–	–	–	–	4	2	$\bar{4}$	$\bar{2}$

5.3 Experiment

The apparatus has been described in Chapter 3. Rotor 2 in Table 3.1 was used together with two detectors of the first type described in section 3.7. The lead single crystal was in the form of a cylinder 2.5 in long and 1.5 in in diameter. The mosaic spread, given by a neutron rocking curve, was about 0.4° standard deviation. The hydrogen liquefier was not very reliable at this time, and no liquid hydrogen moderator was available for this experiment.

The lead crystal was mounted with a (1,1,0) mirror plane parallel to the scattering plane. Neutron time-of-flight spectra were obtained with the crystal at various orientations about an axis perpendicular to the scattering plane. All phonons whose frequencies have been determined therefore have their wave vectors and polarisation vectors in the (1,1,0) mirror plane.

A typical time of flight spectrum is shown in fig.5.1. The time channel width is 40 μ sec. The positions of the peaks were estimated by eye as the computer programme *Fit and Search* had not been written at this time. The I.B.M. 7090
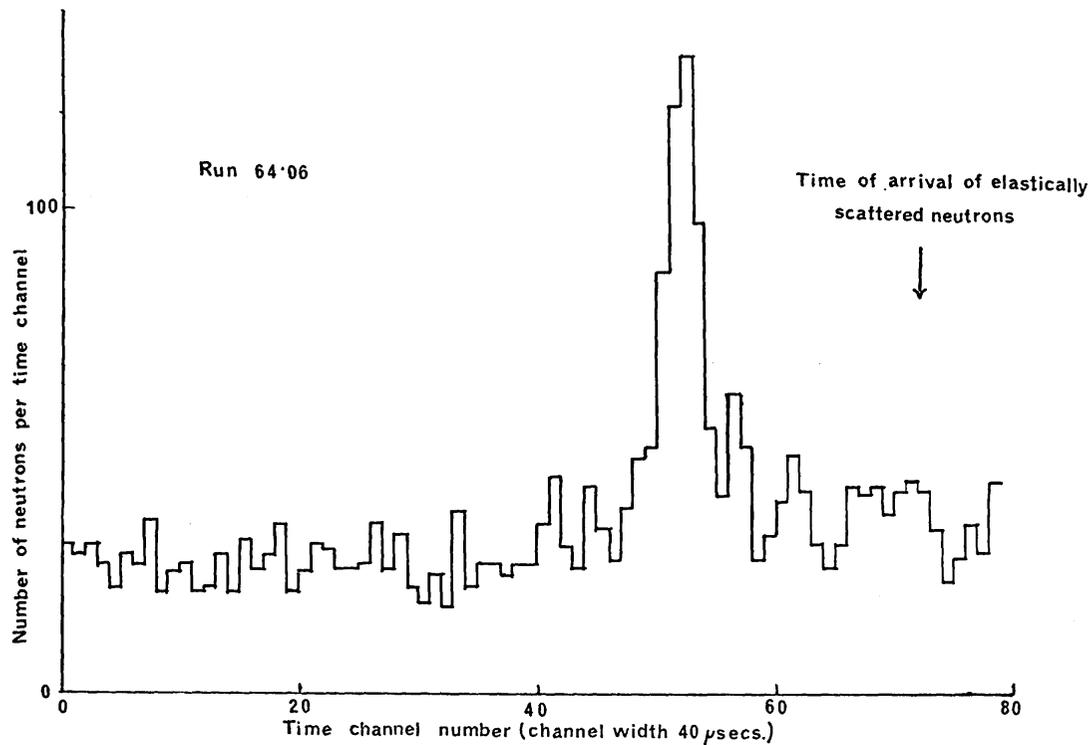
Figure 5.1: Typical time-of-flight spectrum from lead

computer was used to calculate the phonon frequencies and wave vectors from the positions of these peaks and the geometry of the apparatus.

Time of flight spectra were observed for 18 different orientations of the crystal spaced 10° apart. There was some difficulty at first in cooling the beryllium filter and it was necessary to accumulate the counts from the detectors for 12 hours to determine the time of flight spectra. Later, with the filter cooling system functioning, the counting period was reduced to 6 hours. A force constant model was fitted to the results by Squires, and the dispersion relation for the (110) plane according to this model is shown as a contour map in fig.5.3. Two branches of the dispersion relation have polarisation vectors parallel to the plane. The upper branch (1) is shown on the left-hand side of the diagram, and the lower branch (2) on the right. Degenerate points are indicated (see key in fig.5.2). The symmetry classification (longitudinal (L) or transverse (T)) of the branches in symmetry directions is also shown.

The triangles indicate the experimental points. Let the components of the wave vector of the phonon be q_1, q_2 and its frequency be ν_e. Estimates of the standard deviation errors in these quantities due to errors in determining the time of flight corresponding to the phonon peak are δq_1, δq_2, $\delta \nu_e$. As in Chapter 4, this is considered to be the main source of error. The effective error in the frequency $\delta \nu$ is given by

$$\delta \nu = \delta \nu_e + \frac{\partial \nu}{\partial q_1} \delta q_1 + \frac{\partial \nu}{\partial q_2} \delta q_2$$

where the errors are combined linearly as they are all derived from the one error in the time of flight. The gradients of the dispersion relation were approximated by assuming that they were given by the elastic constants out to a radius of half the Brillouin zone radius, and were zero beyond this. The theoretical frequency for wave vector (q_1, q_2) is ν_t. The branch to which the experimental point belonged was usually obvious because of the large difference in frequency between branches over most of the Brillouin zone. The mid point of the base of the triangle has coordinates (q_1, q_2), the height of the triangle is proportional to $(\nu_e - \nu_t)$ (1 cm $= 0.2 \times 10^{12}$ c/sec*), and the width of its base is proportional to $\delta \nu$ to the same scale. An inverted triangle indicates that ν_e is less than ν_t. It is seen that there are few significant deviations from the theory, as would be
represented by tall thin triangles, and in no region of the plane do the experimental frequencies lie systematically above or below the theoretical values. The theory is then a good fit to the experimental points. The experimental error is of order 5% standard deviation for points near the zone boundary.

## 5.4 The Force Constant Model

Squires used the I.B.M. 7090 computer to fit force constant models to the measured dispersion relation for forces extending to 1, 2, ..., 6 orders. The parameters of the theory were adjusted to minimise the sum of the quantities

$$\left(\frac{\nu_t^2 - \nu_e^2}{2 \nu_e \, \delta \nu} \right)^2$$

---

* The figures have been been scaled to fit an a4 page size. The original height (smaller side) of the figure was 12 cm, equivalent to 2.4×10^{12} c/sec
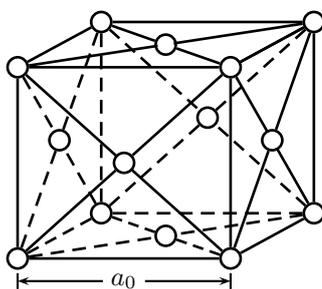
The structure of lead
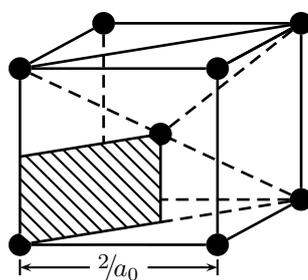
The reciprocal lattice of lead, showing the portion of the mirror plane covered
by the contour map

─────────	Symmetry direction
− − − −	Brillouin zone boundary
●	Reciprocal lattice point
○	Point of high symmetry ($(1,0,0)$ or $(1/2, 1/2, 1/2)$)
⊙	Degeneracy with branch above
⊕	Degeneracy with branch below
▲ ▼	Experimental point (see section 5.3)

The contour interval is 0.2×10^{12} c/sec

Spot frequencies are in units of 10^{12} c/sec

Figure 5.2: Key to contour map (fig. 5.3)
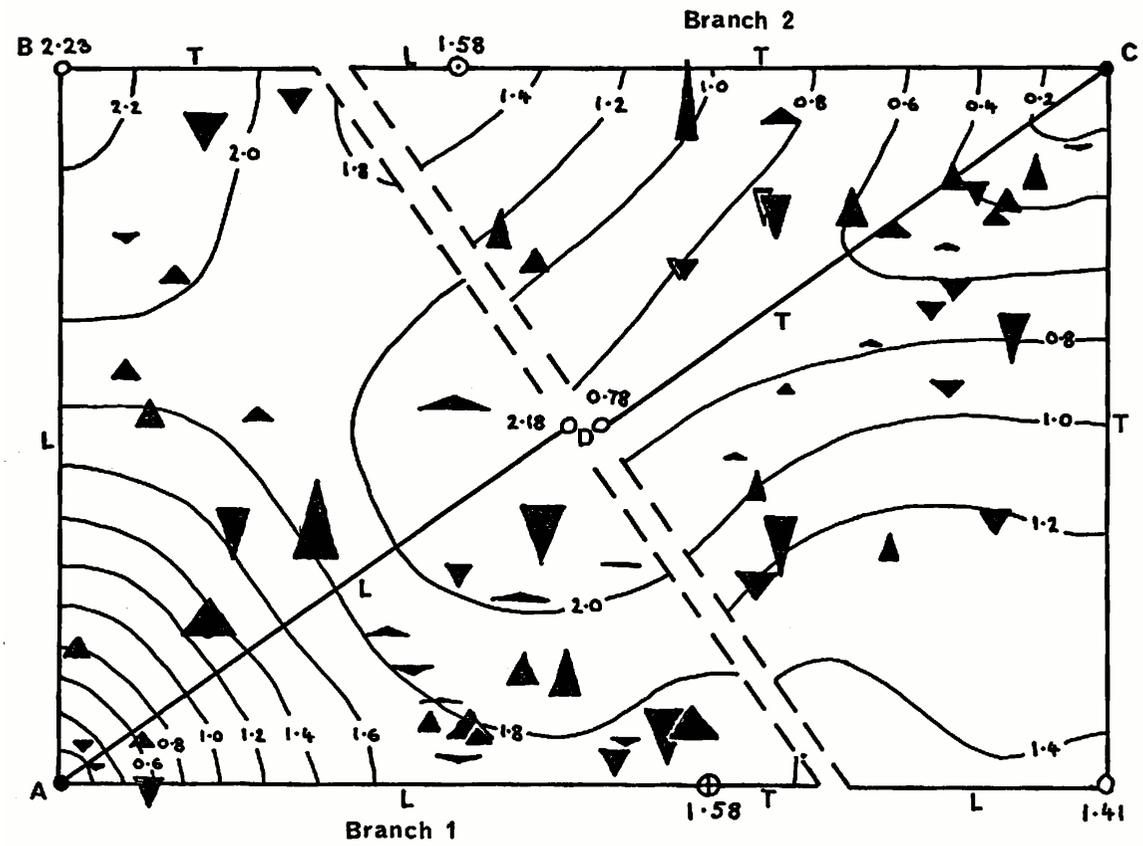
Figure 5.3: Phonon dispersion relation for lead

for all the experimental points. The force constants were constrained to fit the elastic constants given by Goens and Weerts(1936).

$$c_{11} = 4.83 \times 10^{11} \quad \text{dynes/cm}^2$$
$$c_{12} = 4.09 \times 10^{11} \qquad ''$$
$$c_{44} = 1.44 \times 10^{11} \qquad ''$$

Little further reduction in the sum of squares was obtained by allowing the force constants to extend beyond 5 orders. The force constants obtained for forces extending to 3 orders were

$$\alpha_1 = -0.928$$
$$\beta_1 = 3.544$$
$$\delta_1 = 3.539$$
$$\alpha_2 = -1.249$$
$$\gamma_2 = 1.641$$
$$\alpha_3 = 0.339$$
$$\gamma_3 = 0.035$$
$$\delta_3 = 0.559$$
$$\rho_3 = -0.570$$

The units are 10^3 dynes/cm. These force constants have been used to calculate the frequencies from which the contours in fig. 5.3 have been drawn.

Sections of the theoretical dispersion relation in the symmetry directions marked ABCD in fig. 5.3 are shown in fig.5.4 as full lines. The broken lines represent Brockhouse's experimental results. These have been calculated from his listed coefficients Φ_n for the dispersion relation in the $(\zeta, 0, 0)$ and (ζ, ζ, ζ) directions at room temperature. Brockhouse does not quote results at room temperature for the direction $(\zeta, \zeta, 0)$, so the dispersion relation in this direction has been scaled from his diagram for results taken at 100^0K.

The two sets of results give quite different frequencies in the neighbourhood of the point B (1,0,0), particularly for the lower branch. An examination of figure 5.3 shows that there are no experimental points in this region. This is a serious shortcoming of the present results.

The coefficients Φ_n have been calculated from the relations expressed in Table 5.2, and are plotted in fig. 5.5 (the points are joined by full lines). Brockhouse's coefficients are shown joined by broken lines. These are his room temperature results for the directions $(\zeta, 0, 0)$ and (ζ, ζ, ζ) and 100^0K results for the direction $(\zeta, \zeta, 0)$. The previously mentioned differences show up as an increase in even harmonics, and a decrease in odd harmonics in the present results as compared with those of Brockhouse.

5.5 Conclusions

The present results agree with those of Brockhouse as far as they go, but they are not very accurate. The importance of obtaining values of the frequency for wave vectors in all regions of the mirror plane has been emphasised by the effects of the lack of values in the neighbourhood of the point (1, 0, 0). Measurements
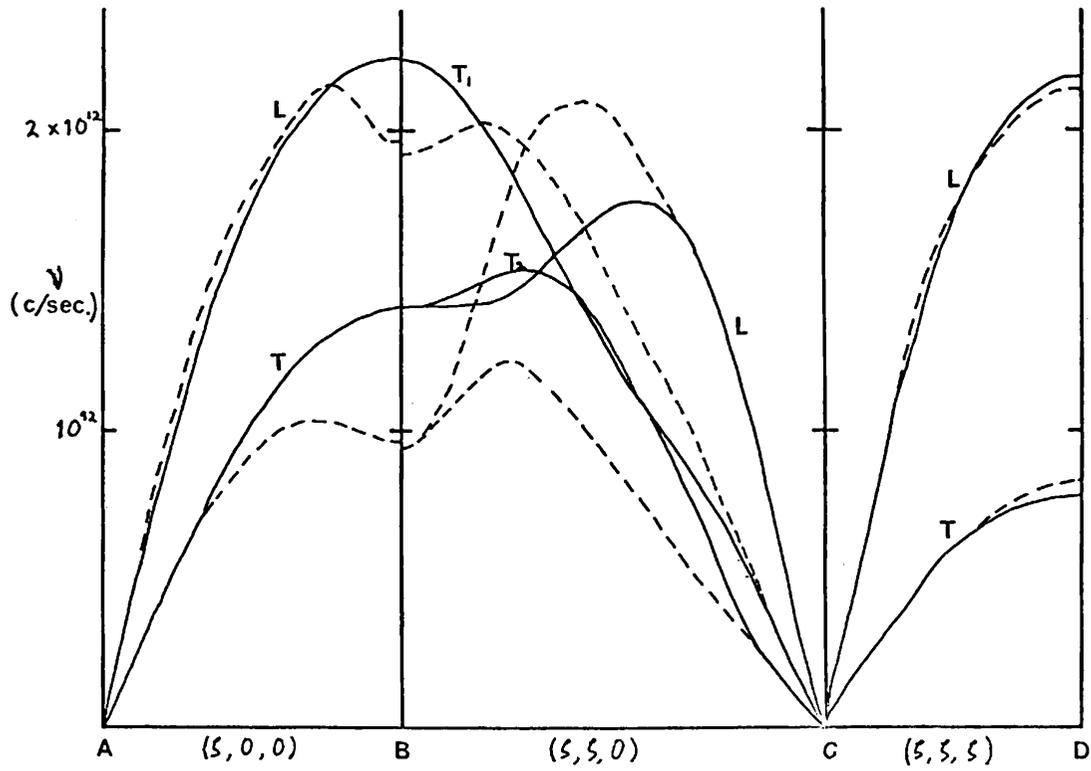
Figure 5.4: Phonon dispersion relation for lead
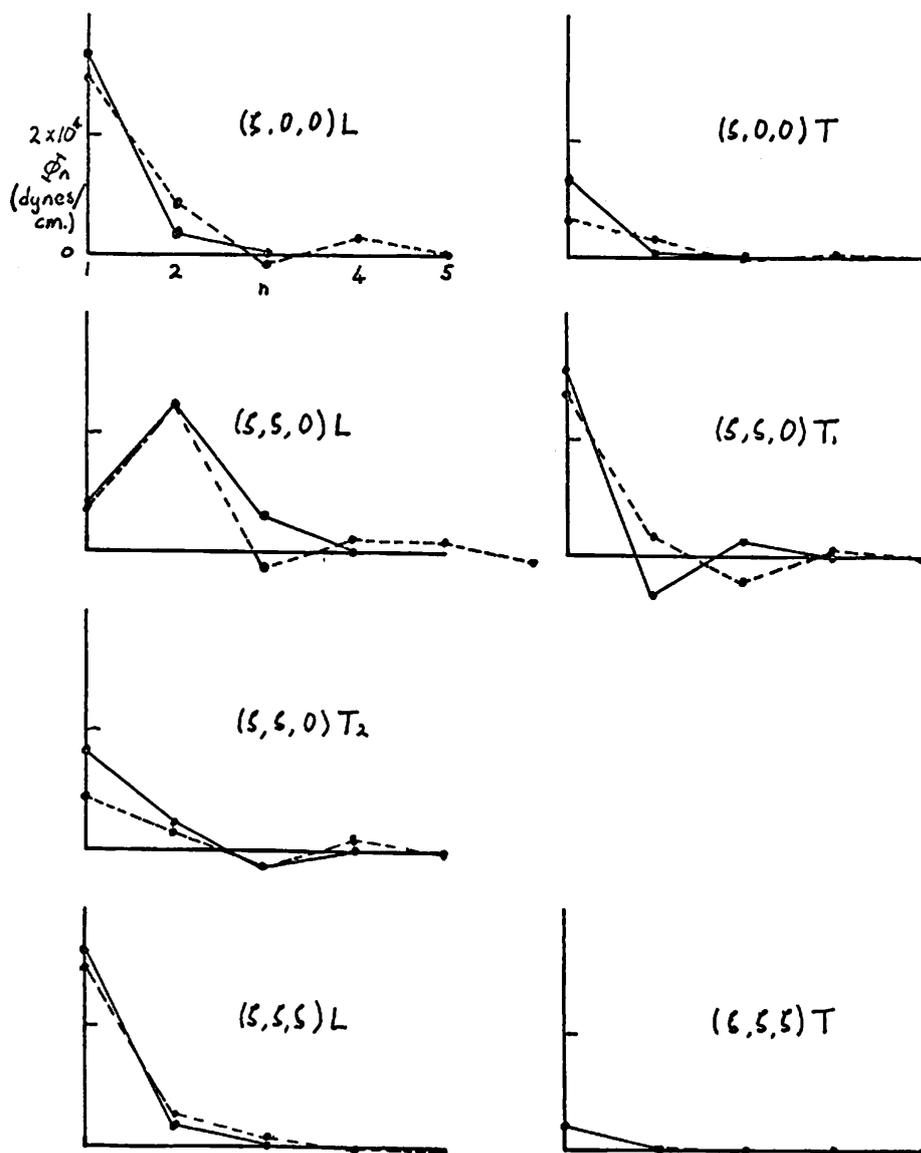
Figure 5.5: Inter-planar force constants (Φ_n) for lead

in the other mirror plane would have been necessary to determine a full set of interatomic force constants had the range of the forces been extended beyond the third order. However, forces extending to the third order gave a satisfactory fit to the experimental data.

The counting period necessary to obtain time of flight spectra in each crystal position was not unduly long (6 hours). The presence of a liquid hydrogen moderator increases the flux by a factor of about $3\,1/2$, so that with the moderator a rotor of significantly greater resolution could be used. It would then be necessary to decrease the detector thickness, or this would be the source of the dominant term in the time of flight resolution.

page 112   It was decided not to extend these measurements to meet the above criticisms as an extensive series of experiments on lead had been started by Brockhouse and it was thought that the time would be better spent studying the dispersion relation of another material.

Chapter 6

The Phonon Dispersion Relation for Magnesium Oxide – Theoretical

6.1 Introduction

The rigid ion and shell models for the lattice dynamics of ionic crystals are discussed. A technique for evaluating the lattice sums occurring in the expressions for the electrostatic coupling coefficients is given. Physical assumptions are made to reduce the number of arbitrary parameters in the theory to six and these parameters are chosen to fit the three elastic constants and the three constants describing the infra-red dispersion. Theoretical dispersion relations are calculated for phonons with wave vectors in the two mirror planes, and polarisation vectors parallel to these planes. The dispersion relations are presented as contour maps of the four branches in each plane. The nature of the degeneracies between these branches is discussed.

6.2 The Rigid Ion Model

The main contribution to the cohesive energy of an ionic crystal is the Madelung energy due to the electrostatic attraction of the ions. Other forces in the crystal are of short range and in sum are repulsive, exactly balancing the electrostatic forces when the ions occupy their equilibrium positions. The change in the electrostatic potential caused by moving an ion from its equilibrium position may be described by introducing dipole, quadripole, and higher moments centred on the equilibrium position of the ion. We shall use the dipole approximation and ignore the quadripole and higher moments. In the rigid ion model, the ion moves without distortion, and the dipole moment is the product of the ionic charge, Z_k, and the displacement, $u_{1,k}$. The elements of the dynamical matrix are the sum of two terms

$$M_{k,k'}^{\alpha,\beta} = \frac{1}{\sqrt{m_k m_{k'}}} \left\{ R_{k,k'}^{\alpha,\beta} + Z_k Z_{k'} \, C_{k,k'}^{\alpha,\beta} \right\}$$

the first due to the short range forces, and the second due to the long range dipole forces. Kellermann (1940) used the rigid ion model to calculate phonon dispersion relations for sodium chloride. Arbitrary parameters were introduced for the short range forces, their values being obtained from experimental measurements of the elastic constants, and rapidly convergent series were used to calculate the Coulomb coefficients $C_{k,k'}^{\alpha,\beta}$

6.3 The Short Range Forces

It has been found that a consistent set of ionic radii can be given to the ions so that in an ionic crystal, the nearest neighbour separation is given by

the sum of the ionic radii. Obviously a constant could be added to the radii of the positive ions and subtracted from the radii of the negative ions without upsetting the above additivity rule, so that additional information is required to fix the ionic radii. Wasastjerna (1923) determined ratios of the ionic radii indirectly from the molar refractions of the ions by assuming that the radii indicate the extensions of the electron orbits. Goldschmidt's (1926) radii have been chosen so that the values for O^{--} and F^- agree with those obtained by Wasastjerna. Pauling (1948) defines a set of univalent radii inversely proportional to $Z - S$, where Z is the ionic charge and S is a screening constant, for ions in the same iso-electronic series (i.e., ions with the same number of electrons). The constant of proportionality is chosen to reproduce correctly the empirical lattice constant for the alkali halide crystal formed from ions in the series. Crystal radii are obtained from the univalent radii by correcting for the increased electrostatic attraction with an inverse power form for the short range forces. Pau1ing's radii are in general agreement with those of Goldschmidt. The following ionic radii are given for magnesium and oxygen:

Table 6.1: Ionic Radii (Å)

	Mg^{++}	O^{--}
Goldschmidt	0.78	1.32
Pauling	0.65	1.40

The following table shows the separation between first and second neighbour pairs of ions compared with the sum of their radii.

Table 6.2: Separation of the ions in MgO compared with the sum of the ionic radii(Å)

Ions	Separation	Sum of ionic radii	
		Goldschmidt	Pauling
$Mg^{++} - O^{--}$	2.10	2.10	2.05
$Mg^{++} - Mg^{++}$	2.97	1.56	1.30
$O^{--} - O^{--}$	2.97	2.64	2.80

The short range forces arise from overlap of the electron wave functions. If the ionic radii indicate the extent of the wave functions, we can expect the largest contribution to these forces to come from the interaction between Mg^{++} and O^{--} ions, a significant contribution from the interaction between O^{--} and O^{--} ions and lesser contributions from other interactions.

Cowley (1962) gives expressions for the elastic constants in terms of snort range force constant parameters and the ionic charge (see section 6.6). The combination $c_{11} + c_{44}$ in the absence of second neighbour forces is determined by the ionic charge alone.

$$c_{11} + c_{44} = \left(\frac{e^2}{vr_0} \right) 1.39100 \, Z^2$$

59

v is the volume of the unit cell, r_o the separation between ions and Z the ionic charge in units of the electronic charge e. For MgO, with $Z = 2$, the right-hand side of this expression is equal to 32.57×10^{11} dynes/cms^2. The experimental values for the elastic constants (Dae-Hyun Chung, 1963; values quoted in section 6.8) give the left-hand side a value of 24.26×10^{11} dynes/cms^2. This discrepancy can be removed by the introduction of second neighbour forces as was suggested by by a consideration of the ionic diameters. The short range interaction between first neighbours ($Mg^{++} - O^{--}$) is described by two parameters. The force between the ion at $(1, 0, 0)$ and the ion at the origin is described by the 2×3 matrix $\Phi_{l,1,2}^{\alpha,\beta}$ where l depends on the choice of unit cell and $\alpha, \beta = 1, 2, 3$. In Cowley's (1962) notation this matrix may be written

$$\frac{e^2}{2v} \begin{pmatrix} A & 0 & 0 \\ 0 & B & 0 \\ 0 & 0 & B \end{pmatrix}$$

The matrices of force constants between other first neighbours are found from symmetry.

The short range interaction between second neighbours ($O^{--} - O^{--}$) is described by 3 parameters. The force between the ion at $(1, 1, 0)$ and the ion at the origin is described by the matrix $\Phi_{l,2,2}^{\alpha,\beta}$

$$\frac{e^2}{2v} \begin{pmatrix} \frac{1}{2}(A'' + B'') & \frac{1}{2}(A'' - B'') & 0 \\ \frac{1}{2}(A'' - B'') & \frac{1}{2}(A'' + B'') & 0 \\ 0 & 0 & D'' \end{pmatrix}$$

The force constants between other second nearest neighbours may be found by symmetry from this matrix.

These force constants describe the most general forces possible in a cubic crystal. The forces may be restricted in several ways:

(a) Axially symmetric forces

The force constant matrix is invariant under a rotation of the axes about the line joining the particles concerned. If axes are chosen so that the X axis is parallel to this line (these axes will be called axes A), the matrix must be of the form

$$\begin{pmatrix} A & 0 & 0 \\ 0 & B & 0 \\ 0 & 0 & B \end{pmatrix}$$

The first neighbour matrix is already in this form. The second neighbour matrix, when referred to axes A, becomes

$$\begin{pmatrix} A'' & 0 & 0 \\ 0 & B'' & 0 \\ 0 & 0 & D'' \end{pmatrix}$$

If the forces are to be axially symmetric, we must, then, impose the condition

$$D'' = B''$$

(b) Central forces

The potential energy associated with each force is assumed to be a function only of the distance between the particles. The derivatives of this potential are

$$\frac{\partial \phi}{\partial r^\alpha} = \frac{\partial |r|}{\partial r^\alpha} \frac{\partial \phi}{\partial |r|} = \frac{r^\alpha}{|r|} \frac{\partial \phi}{\partial |r|}$$

$$\frac{\partial^2 \phi}{\partial (r^\alpha)^2} = \left(\frac{r^\alpha}{|r|}\right)^2 \frac{\partial^2 \phi}{(\partial |r|)^2} + \left(\frac{1}{|r|} - \frac{(r^\alpha)^2}{|r|^3}\right) \frac{\partial \phi}{\partial |r|}$$

$$\frac{\partial^2 \phi}{\partial r^\alpha \, \partial r^\beta} = \frac{r^\alpha r^\beta}{|r|^2} \frac{\partial^2 \phi}{(\partial |r|)^2} - \frac{r^\alpha r^\beta}{|r|^3} \frac{\partial \phi}{\partial |r|} \qquad \text{for } \alpha \neq \beta$$

Referred to axes A, the force constant matrix $\frac{\partial^2 \phi}{\partial r^\alpha \, \partial r^\beta}$ becomes

$$\begin{pmatrix} \frac{\partial^2 \phi}{\partial (r^\alpha)^2} & 0 & 0 \\ 0 & \frac{1}{|r|} \frac{\partial \phi}{\partial |r|} & 0 \\ 0 & 0 & \frac{1}{|r|} \frac{\partial \phi}{\partial |r|} \end{pmatrix}$$

The forces are seen to be axially symmetric.

However, we now have a relation between some of the force constants and the first derivatives of the potential energy

$$\frac{e^2}{2v} B = \frac{1}{r_0} \frac{\partial \phi^{(1,0,0)}}{\partial r_0} \quad \text{and} \quad \frac{e^2}{2v} B'' = \frac{1}{r_1} \frac{\partial \phi^{(1,1,0)}}{\partial r_1}$$

where r_0 is the separation of nearest neighbour ions and $r_1 = \sqrt{2} r_0$. This leads to a stability condition. The potential energy per unit cell of the crystal, Φ, is given by

$$\Phi = -\alpha_M \frac{Z^2 e^2}{r_0} + 6\phi^{(1,0,0)} + 6\phi^{(1,1,0)}$$

where α_M is Madelung's constant. ($\alpha_M = 1.7476$ for a crystal with the sodium chloride structure). In the absence of external pressure, we must have

$$\frac{\partial \Phi}{\partial r_0} = 0$$

This gives the stability condition (Kellermann, 1940; Cowley, 1962)

$$B + 2B'' = -\frac{2}{3} \alpha_M Z^2$$

Use of the stability condition, together with the conditions for axially symmetric forces, gives the Cauchy relation between the elastic constants (see section 6.6)

$$c_{12} = c_{44}$$

The coupling coefficients of the short range interactions are given by Cowley

$$R_{1,2}^{\alpha,\alpha} = -\frac{e^2}{v}\left\{A\cos\pi q_\alpha + B(\cos\pi q_\beta + \cos\pi q_\gamma)\right\}$$

$$R_{1,1}^{\alpha,\alpha} = \frac{e^2}{v}\left\{A + 2B\right\}$$

$$R_{2,2}^{\alpha,\alpha} = \frac{e^2}{v}\left\{A + 2B + 2A'' + 2B'' + 2D'' - (A'' + B'')(\cos\pi q_\alpha)\right.$$
$$\left.(\cos\pi q_\beta + \cos\pi q_\gamma) - 2D''\cos\pi q_\beta\cos\pi q_\gamma\right\}$$

$$R_{1,2}^{\alpha,\beta} = 0$$

$$R_{1,1}^{\alpha,\beta} = 0$$

$$R_{2,2}^{\alpha,\beta} = \frac{e^2}{v}(A'' - B'')\sin\pi q_\alpha\sin\pi q_\beta$$

α, β and γ are all different in these formulae. The phonon wave vector $\boldsymbol{q}$ is in units of $1/2r_0$.

6.4 The Electrostatic Forces

The potential at the origin due to the dipole $\boldsymbol{p}$ at the point $\boldsymbol{r}$

$$-\boldsymbol{p}\cdot\boldsymbol{\nabla}\left(\frac{1}{|r|}\right)$$

The Coulomb coefficients are given by

$$C_{k,k'}^{\alpha,\beta} = -e^2\lim_{\boldsymbol{r}\to 0}\left\{\sum_l{}'\frac{\partial^2}{\partial r^\alpha\partial r^\beta}\frac{1}{|\boldsymbol{r}-\boldsymbol{r}_l|}e^{2\pi i\,\boldsymbol{q}\cdot\boldsymbol{r}_l}\right\}$$

$$C_{k,k'}^{\alpha,\beta} = -e^2 e^{-2\pi i\,\boldsymbol{q}\cdot(\boldsymbol{r}_k-\boldsymbol{r}_{k'})}\lim_{\boldsymbol{r}\to\boldsymbol{r}_k-\boldsymbol{r}_{k'}}\left\{\sum_l\frac{\partial^2}{\partial r^\alpha\partial r^\beta}\frac{1}{|\boldsymbol{r}-\boldsymbol{r}_l|}e^{2\pi i\,\boldsymbol{q}\cdot\boldsymbol{r}_l}\right\}$$

where k and k' are different, and $\sum_l{}'$ excludes the term with $l = 0$. These series as they stand converge very slowly. A rapidly convergent form can be found by making use of the Ewald transformation

$$\frac{2}{\sqrt{\pi}}\sum_l\exp\left(\epsilon^2|\boldsymbol{r}-\boldsymbol{r}_l|^2 + 2\pi i\,\boldsymbol{q}\cdot\boldsymbol{r}_l\right)$$

$$= \frac{2\pi}{v}\sum_h\frac{1}{\epsilon^3}\exp\left(\frac{\pi^2}{\epsilon^2}|\boldsymbol{q}+\boldsymbol{\tau}_h|^2 + 2\pi i\,\boldsymbol{r}\cdot(\boldsymbol{q}+\boldsymbol{\tau}_h)\right)$$

where $\boldsymbol{\tau}_h$ is a vector of the reciprocal lattice.

Kellermann (1940) gives the following formulae for the Coulomb coefficients (his coefficients differ in sign from those given here)

$$C_{1,1}^{\alpha,\beta} = \frac{e^2}{v}\left\{G_{1,1}^{\alpha,\beta} - HG_l^{\alpha,\beta} - \frac{8}{3\sqrt{\pi}}\epsilon^3\delta_{\alpha\beta}\right\}$$

$$C_{1,2}^{\alpha,\beta} = \frac{e^2}{v}\left\{G_{1,2}^{\alpha,\beta} - H_m^{\alpha,\beta}\right\}$$

$$C_{2,2}^{\alpha,\beta} = C_{1,1}^{\alpha,\beta}\qquad\text{and}\qquad C_{2,1}^{\alpha,\beta} = C_{1,2}^{\alpha,\beta}$$

$$\text{where} \quad G^{\alpha,\beta}_{k,k'} = 4\pi \sum_h p(h) \frac{(h_\alpha + q_\alpha)(h_\beta + q_\beta)}{|\boldsymbol{h} + \boldsymbol{q}|^2} e^{-\frac{\pi^2}{4\epsilon^2}|\boldsymbol{h}+\boldsymbol{q}|^2}$$

and for $(k, k') = (1, 1), \quad p(h) = +1$
for $(k, k') = (1, 2), \quad p(h) = +1 \quad$ for h_α even
$= -1 \quad$ for h_α odd

$$H^{\alpha,\beta}_l = 2 \sum_l \left\{ -f(l)\delta_{\alpha,\beta} + g(l)\frac{l_\alpha l_\beta}{l^2} \right\} \cos \pi \boldsymbol{q} \cdot \boldsymbol{l}$$

$$f(l) = \frac{2}{\sqrt{\pi}} \epsilon \frac{e^{-\epsilon^2 l^2}}{l^2} + \frac{\psi(\epsilon l)}{l^3}$$

$$g(l) = \frac{4}{\sqrt{\pi}} \epsilon^3 e^{-\epsilon^2 l^2} + \frac{6}{\sqrt{\pi}} \epsilon \frac{e^{-\epsilon^2 l^2}}{l^2} + 3\frac{\psi(\epsilon l)}{l^3}$$

$$\psi(\epsilon l) = 1 - \frac{2}{\sqrt{\pi}} \int_0^{\epsilon l} e^{-\zeta^2} \, d\zeta$$

$$l = |\boldsymbol{l}|$$

The phonon wave vector $\boldsymbol{q}$ is expressed in units of $1/2r_0$.

q_α are the components of $\boldsymbol{q}$ in the directions of the crystal cube edges.

$\sum_l$ indicates a sum over the sites of ions of the same type as that at the origin. l_α take all integral values for which $\sum_\alpha l_\alpha$ is even. The origin is excluded.

$\sum_m$ indicates a sum over the remaining ion sites. m_α take all integral values for which $\sum_\alpha m_\alpha$ is odd.

$\sum_h$ indicates a sum over the reciprocal lattice points. h_α are integers and either all even or all odd.

$\boldsymbol{l}$ is a vector with components l_α. $\boldsymbol{h}$ is similarly defined.

ϵ is an arbitrary parameter controlling the convergence of G and H. G is more rapidly convergent for small ϵ, and H is more rapidly convergent for large ϵ.

A routine was written for the Stretch computer to evaluate the Coulomb coefficients and their derivatives with respect to the components of $\boldsymbol{q}$ for any phonon wave vector $\boldsymbol{q}$. The lattice points may conveniently be divided into orders, each order consisting of all those points which can be generated from a single point by the operations of cubic symmetry. $f(l)$ and $g(l)$ are the same for all points in an order. The summation is done order by order in increasing distance from the origin. Simple algebraic expressions can be found for the sum H over a given order. However, this is not possible for the sum G and explicit summation over the points in an order was necessary. In fact it proved convenient to sum explicitly over the points in an order for H as well as for G. If we impose the following restriction on $\boldsymbol{l}$, only one point in each order is given.

$$0 \underset{1}{\leq} l_1 \underset{2}{\leq} l_2 \underset{3}{\leq} l_3 \tag{6.1}$$

The other points in each order may be generated using the cubic symmetry. In general there are 48 points in an order, but if any of the equality signs apply in the restriction (6.1), there are less than this. If an order contains n points, a sum over the order may be evaluated by summing over 48 points, ignoring the fact that points may be duplicated, and then multiplying by $n/48$. This method leads to unnecessary computation and it was decided to use a technique which would ensure that none of the points in an order would be duplicated. All the points in an order may be generated by repeated application of the following four operators:

Table 6.3: The Cubic Symmetry Operators

Operator	Effect on $\boldsymbol{l} = (l_1,\, l_2,\, l_3)$
C_3 (triad axis)	$C_3\,\boldsymbol{l} = (l_2,\, l_3,\, l_1)$
C_4 (tetrad axis)	$C_4\,\boldsymbol{l} = (\bar{l}_2,\, l_1,\, l_3)$
σ (mirror plane)	$\sigma\,\boldsymbol{l} = (l_2,\, l_1,\, l_3)$
I (centre of inversion)	$\mathrm{I}\,\boldsymbol{l} = (\bar{l}_1,\, \bar{l}_2,\, \bar{l}_3)$

They are applied as indicated in the following diagram. The first term in the sum is calculated for the point $\boldsymbol{l} = (l_1,\, l_2,\, l_3)$ and the operator C_3 is applied to $\boldsymbol{l}$. The next term is added and C_3 applied again, and so on until $n(C_3$ terms have been calculated and C_3 applied $n(C_3$ times. The operator C_4 is now applied and the whole repeated until C_4 has been applied $n(C_4$ times when σ is applied and so on. All operations enclosed by a return path in the diagram are to be performed the number of times shown on the return path each time they are entered afresh. (The return path is used this number minus one times.) If

Figure 6.1: Application of the operators to generate the points of one order

$n(C_3)$, $n(C_4)$, $n(\sigma)$, and $n(\mathrm{I})$ are set to the values shown in table 6.4, a term

64

will be added for each point in the order and no points will be duplicated. In

Table 6.4: Numbers of operations

Equalities satisfied in 6.1	Form of $\boldsymbol{l}$	n	$n(C_3)$	$n(C_4)$	$n(\sigma)$	$n(I)$
None	(l_1, l_2, l_3)	48	3	4	2	2
1	$(0, l_1, l_2)$	24	3	4	1	2
2	(l_1, l_1, l_2)	24	3	4	1	2
3	(l_1, l_2, l_2)	24	3	4	1	2
1, 2	$(0, 0, l_1)$	6	3	1	1	2
2, 3	(l_1, l_1, l_1)	8	1	4	1	2
3, 1	$(0, l_1, l_1)$	12	3	1	2	2
1, 2, 3	$(0, 0, 0)$	1	1	1	1	1

this table $0 < l_1 < l_2 < l_3$ for the components of a given $\boldsymbol{l}$.

Values of $\boldsymbol{l}$, $\boldsymbol{m}$ and $\boldsymbol{h}$ and of $g(l)$ and $f(l)$ for the first 20 orders are prepared by a separate routine which is called once only each time the programme is loaded. Summation over orders is continued until three adjacent groups of orders are found such that the largest contribution to the sum from the first group has magnitude less than 10^{-6}, that from the second group less than 10^{-7}, and that from the third group less than 10^{-8}. (The sums are of order unity). This method will not terminate the sum prematurely if the contribution from an order is negligible, but that from the next order is important, as might happen with a simpler criterion. The sums for all the Coulomb coefficients and their derivatives are calculated at once, so that the largest contribution from an order is taken as the largest contribution to any of the Coulomb coefficients or their derivatives. After a few trials, ϵ was set to 1.3. About 9 orders were then included in each sum.

6.5 The Shell Model

Kellermann, using the rigid ion model, was able to account quite well for the measured elastic constants and infra-red absorption frequency of sodium
chloride. However, it is easily seen that this theory is inconsistent with the known dielectric constants. In the presence of a high frequency electric field, the ions do not move and the polarisation of the crystal arises entirely from distortion of the ions. If, as in the rigid ion model, we ignore this distortion, we shall obtain a value of 1 for the high frequency dielectric constant. In practice the high frequency dielectric constants of ionic crystals range from about 1.7 to 5.1 (Born and Huang, 1954, table 17).

The *Shell Model* allows the effects of the distortion of the ions to be taken into account, whilst the theory remains within the framework of the Born–von Karman theory of lattice dynamics. This theory was introduced by Dick and Overhauser (1958) and by Hanlon and Lawson (1959) in studies of the dielectric properties of alkali halides. The theory has been used to calculate phonon dispersion relations in the alkali halides by Woods, Cochran and Brockhouse

(1960). This account of the theory follows the last reference and subsequent papers by Cochran (1961), Cowley (1962) and Cowley, Cochran, Brockhouse and Woods (1963).

The outer electrons of an ion are considered to form a shell which can move without distortion about its equilibrium position centred on the core of the ion. Relative displacement of the shell and core produces a dipole moment on the ion, representing the effect of distorting the ion. We use the Coulomb coefficients introduced for the point ion model to calculate the long range effects of this dipole moment, and the short range effects are allowed for by introducing arbitrary short range forces linking the shells and cores. Each shell is linked to its own core by an isotropic force constant, k_1 for the positive ion and k_2 for the negative ion. The shell charges are $Y_1 e$ and $Y_2 e$ respectively, so that the free ion polarisability of the positive ion is $\frac{Y_1^2 e^2}{k_1}$ and of the negative ion $\frac{Y_2^2 e^2}{k_2}$

The potential energy Φ is a function of the core displacements $\boldsymbol{u}_{l,k}$, and the shell displacements $\boldsymbol{v}_{l,k}$. The force constants are defined by

$$\Phi^{(E)\,\alpha,\beta}_{l-l',k,k'} = \frac{\partial^2 \Phi}{\partial u^\alpha_{l,k} \partial u^\beta_{l',k'}}$$

$$\Phi^{(S)\,\alpha,\beta}_{l-l',k,k'} = \frac{\partial^2 \Phi}{\partial v^\alpha_{l,k} \partial v^\beta_{l',k'}}$$

$$\Phi^{(F)\,\alpha,\beta}_{l-l',k,k'} = \frac{\partial^2 \Phi}{\partial u^\alpha_{l,k} \partial v^\beta_{l',k'}} \left(1 - \delta_{ll'}\delta_{kk'}\right)$$

We assume

$$\frac{\partial^2 \Phi}{\partial u^\alpha_{l,k} \partial v^\beta_{l,k'}} = k_k \delta_{\alpha,\beta}$$

The notation is similar to that of Chapter 2. we define coupling coefficients E, S, and F by

$$E^{\alpha,\beta}_{k,k'} = \exp\left\{-2\pi i\,\boldsymbol{q}\cdot(\boldsymbol{r}_k - \boldsymbol{r}_{k'})\right\} \sum_l \Phi^{(E)\,\alpha,\beta}_{l,k,k'} e^{-2\pi i\,\boldsymbol{q}\cdot\boldsymbol{r}_l}$$

etc. From their definitions, E and S are Hermitian, but not F. We define F' as the Hermitian conjugate of F, i.e.,

$$F'^{\,\alpha,\beta}_{k,k'} = \left(F^{\beta,\alpha}_{k',k}\right)^*$$

The forces contributing to the various coupling coefficients are shown schematically in figure 6.2. for a crystal with two ions per unit cell.

The equations of motion are most easily written in terms of the core displacements and the relative displacements of the shells and cores, $\boldsymbol{w}_{l,k} = \boldsymbol{v}_{l,k} - \boldsymbol{u}_{l,k}$. We introduce an ion-ion coupling coefficient, R, and a shell-ion coefficient, T, where

$$R = E + S + F + F'$$
$$\text{and} \quad T = S + F$$

66

All other type 1 ions

All type 1 ions

S_{11}

F_{11}

F'_{11}

E_{11}

k_1

Type 1 ion

E_{12}

F'_{12}

F_{12}

S_{12}

All type 2 ions

S_{21}

F_{21}

F'_{21}

E_{21}

Type 2 ion

k_2

E_{22}

F'_{22}

F_{22}

S_{22}

All other type 2 ions
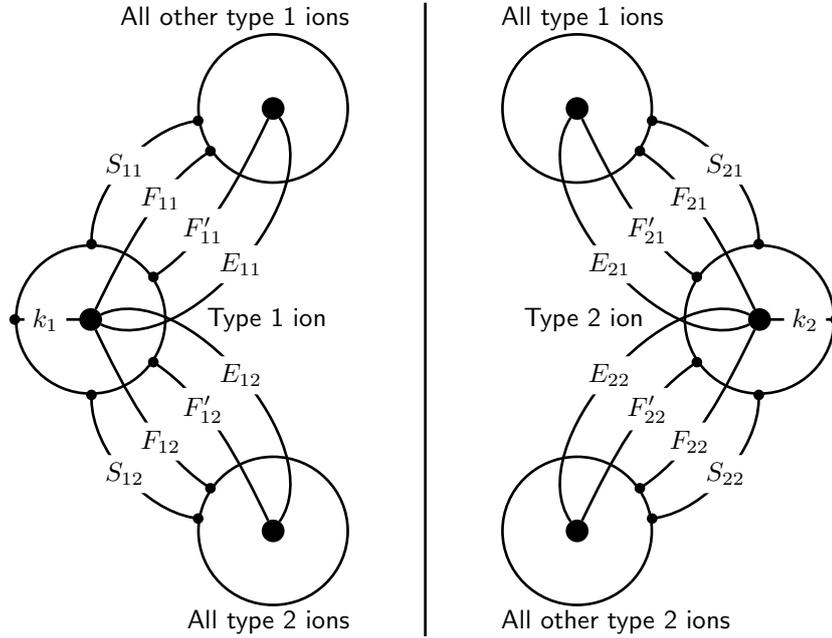
Figure 6.2: Forces between ions

R is Hermitian, but T need not be. In accordance with the adiabatic approximation, the masses of the shells are assumed to be zero.

The equations of motion in matrix notation are

$$m\omega^2 \boldsymbol{u} = A\boldsymbol{u} + B\boldsymbol{w}$$
$$0 = B'\boldsymbol{u} + D\boldsymbol{w}$$

where m is a diagonal matrix

$$m_{ij} = m_k \delta_{ij}$$

$\boldsymbol{u}$ and $\boldsymbol{w}$ are column matrices

$$u_i = u_k^\alpha \qquad w_i = w_k^\alpha$$
and $$A_{ij} = R_{k,k'}^{\alpha,\beta} + Z_k Z_{k'} C_{k,k'}^{\alpha,\beta}$$
$$B_{ij} = T_{k,k'}^{\alpha,\beta} + Z_k Y_{k'} C_{k,k'}^{\alpha,\beta}$$
$$B'_{ij} = (B_{ji})^*$$
$$D_{ij} = S_{k,k'}^{\alpha,\beta} + k_k \delta_{\alpha.\beta} \delta_{k,k'} + Y_k Y_{k'} C_{k,k'}^{\alpha,\beta}$$

In these equations $i = n\alpha + k - n$ and $j = n\beta + k' - n$. Since $\alpha = 1, 2, 3$ and $k = 1, 2, \ldots, n$, $i = 1, 2, \ldots, 3n$ and similarly for j.

We now restrict ourselves to crystals with the sodium chloride structure.
A, B and D are real 6×6 matrices, and A and D are symmetrical. For $\boldsymbol{q} = 0$,

67

choosing axes parallel to the crystal cube edges,

$$
\left.
\begin{array}{l}
R^{\alpha,\beta}_{k,k'}(0) = \delta_{\alpha\beta} R_{kk'}(0) \\
S^{\alpha,\beta}_{k,k'}(0) = \delta_{\alpha\beta} S_{kk'}(0) \\
T^{\alpha,\beta}_{k,k'}(0) = \delta_{\alpha\beta} T_{kk'}(0)
\end{array}
\right\} \text{independent of } \alpha
$$

The invariance of the crystal under translation and the symmetry of R require

$$
\begin{aligned}
R_{11}(0) &= R_{22}(0) = -R_{12}(0) = -R_{21}(0) \\
T_{11}(0) &= -T_{21}(0) \\
T_{22}(0) &= -T_{12}(0)
\end{aligned}
$$

We have introduced four parameters, the shell charges and the shell displacements, to describe two physically meaningful quantities, the electronic dipole moments of the ions. We can, therefore, impose two arbitrary conditions on the equations.

$$
R_{11}(0) = T_{11}(0) = T_{22}(0) = \frac{e^2}{v} R_0
$$

This makes the R and T matrices identical at $\boldsymbol{q} = 0$..

These equations may be derived by postulating that the energy perturbation in the crystal, when the ions are given small displacements, is a quadratic function of the nuclear displacements and the electronic dipole moments. The shell model takes account of the dipole terms in a multipole expansion of the charge distribution about the ion sites. Cowley (1962) has given a quantum mechanical justification for the shell model, and indicated its extension to include quadripole terms. Other theories based on dipole expansions give similar equations to the shell model, the differences being largely in the physical assumptions used to reduce the number of arbitrary parameters (Cowley et al., 1963). It would, of course, be possible to base a theory on a dipole expansion about points in the unit cell other than the ion sites.

6.6 The Macroscopic Constants

An ionic crystal with the sodium chloride structure requires three constants to describe its elastic properties, and three more constants to describe the behaviour of the dielectric constant as a function of frequency for frequencies near the infra-red dispersion frequency.

The elastic constants are given in terms of the short range ion-ion force constants by Cowley (1962). The elastic constants do not depend on the polarisabilities of the ions and are the same as those given by the rigid ion model. In terms of the first and second neighbour force constants defined in the section on the rigid ion model, the elastic constants are

$$
\begin{aligned}
c_{11} &= \frac{e^2}{vr_0} \left\{ \frac{1}{2}(A + A'' + B'') - 2.55604 Z^2 \right\} \\
c_{12} &= \frac{e^2}{vr_0} \left\{ \frac{1}{4}(A'' - 2D'' - 2B - 3B'') + 0.11298 Z^2 \right\} \\
c_{44} &= \frac{e^2}{vr_0} \left\{ \frac{1}{4}(2B + 2D'' + A'' + B'') + 1.27802 Z^2 \right\}
\end{aligned}
$$

68

If the forces are central, use of the stability criterion,

$$B + 2B'' = -\frac{2}{3}\alpha_M Z^2$$

and the condition $D'' = B''$ gives

$$c_{12} = c_{44} = \frac{e^2}{vr_0}\left\{\frac{1}{4}(A'' - B'') - 0.69550Z^2\right\}$$

The equations of motion at $\boldsymbol{q} = 0$ may be written in terms of the effective field $\mathcal{E}$ at an ion site. Due to the symmetry of the crystal this effective field is the same at all ion sites.

$$m_1\omega^2 u_1 = \frac{e^2}{v}\left\{R_0 u_1 - R_0 u_2 + R_0 w_1 - R_0 w_2\right\} - Ze\mathcal{E}$$

$$m_2\omega^2 u_2 = \frac{e^2}{v}\left\{-R_0 u_1 + R_0 u_2 - R_0 w_1 + R_0 w_2\right\} + Ze\mathcal{E}$$

$$0 = \frac{e^2}{v}\left\{R_0 u_1 - R_0 u_2 + (k_1 + S_{11})w_1 + S_{12}w_2\right\} - Y_1 e\mathcal{E}$$

$$0 = \frac{e^2}{v}\left\{-R_0 u_1 + R_0 u_2 + S_{12}w_1 + (k_2 + S_{22})w_2\right\} - Y_2 e\mathcal{E}$$

As before, we have dropped the cartesian superscripts and have used the two arbitrary parameters of the shell model to make the R and T matrices identical at $\boldsymbol{q} = 0$. We have put

$$S_{k,k'}^{\alpha,\beta}(0) = \delta_{\alpha\beta}\frac{e^2}{v}S_{k,k'}$$
$$\text{and}\quad S_{21} = S_{12}$$

From the first two equations,

$$m_1 u_1 + m_2 u_2 = 0$$

and the equations may be rewritten in terms of the relative ion displacements $u = u_1 - u_2$ and the reduced mass $m = \frac{m_1 m_2}{M_1 + M_2}$

$$m\omega^2 u = \frac{e^2}{v}\left\{R_0 u + R_0 w_1 - R_0 w_2\right\} - Ze\mathcal{E}$$

$$0 = \frac{e^2}{v}\left\{R_0 u + (k_1 + S_{11})w_1 + S_{12}w_2\right\} - Y_1 e\mathcal{E}$$

$$0 = \frac{e^2}{v}\left\{-R_0 u + S_{12}w_1 + (k_2 + S_{22})w_2\right\} - Y_2 e\mathcal{E}$$

The polarisation, P, is given by

$$P = \frac{e}{v}(Zu + Y_1 w_1 + Y_2 w_2)$$

The effective field is the sum of the macroscopic field, E, and the Lorentz field $\frac{4\pi}{3}P$.

$$\mathcal{E} = E + \frac{4\pi}{3}P$$

69

The displacement, D, is given by

$$D = \epsilon E = E + 4\pi P$$

where ϵ is the dielectric constant.

Hence $\quad E = \dfrac{4\pi}{\epsilon - 1} P$

and $\quad \mathcal{E} = \dfrac{1}{b} P \qquad$ where $\qquad b = \dfrac{3}{4\pi}\left(\dfrac{\epsilon - 1}{\epsilon + 2}\right)$

This is the Clausius-Mossotti relation.

We now have a fourth equation to add to the other three:

$$\frac{e}{v}(Zu + Y_1 w_1 + Y_2 w_2) - b\mathcal{E} = 0$$

A solution for u, w_1, w_2 and $\mathcal{E}$ is possible if

$$\begin{vmatrix} b & Y_1 & Y_2 & Z \\ Y_1 & k_1 + S_{11} & S_{12} & R_0 \\ Y_2 & S_{12} & k_2 + S_{22} & -R_0 \\ Z & R_0 & -R_0 & R_0 - \frac{vm}{e^2}\omega^2 \end{vmatrix} = 0$$

This equation determines b as a function of ω. The function is completely determined by three constants defined in terms of the shell model parameters. In terms of the dielectric constant, this dispersion formula may be written as

$$\epsilon = \epsilon_\infty + \frac{\epsilon_0 - \epsilon_\infty}{1 - (\frac{\omega}{\omega_0})^2} \tag{6.2}$$

ϵ_0 is the value of ϵ for $\omega = 0$, ϵ_∞ the value of ϵ as ω tends to infinity, and when $\omega = \omega_0$, ϵ is infinite. These three constants are given in terms of the shell model parameters by the following equations:

$$\begin{vmatrix} b_0 & Y_1 & Y_2 & Z \\ Y_1 & k_1 + S_{11} & S_{12} & R_0 \\ Y_2 & S_{12} & k_2 + S_{22} & -R_0 \\ Z & R_0 & -R_0 & R_0 \end{vmatrix} = 0$$

$$b_0 = \frac{3}{4\pi}\left(\frac{\epsilon_0 - 1}{\epsilon_0 + 2}\right)$$

$$\begin{vmatrix} b_\infty & Y_1 & Y_2 \\ Y_1 & k_1 + S_{11} & S_{12} \\ Y_2 & S_{12} & k_2 + S_{22} \end{vmatrix} = 0$$

$$b_\infty = \frac{3}{4\pi}\left(\frac{\epsilon_\infty - 1}{\epsilon_\infty + 2}\right)$$

$$\begin{vmatrix} \frac{3}{4\pi} & Y_1 & Y_2 & Z \\ Y_1 & k_1 + S_{11} & S_{12} & R_0 \\ Y_2 & S_{12} & k_2 + S_{22} & -R_0 \\ Z & R_0 & -R_0 & R_0 - \frac{vm}{e^2}\omega_0^2 \end{vmatrix} = 0$$

70

6.7 Reduction of the Number of Arbitrary Parameters

The equations of the shell model contain a large number of arbitrary parameters, and some simplification is necessary when applying the theory in practice. The polarisability of the positive ion is frequently so small compared with that of the negative ion that it may be ignored. In the case of MgO, the polarisabilities given by Kittel (1956, table 7.1) are 3.88×10^{-24} cms^3 for O^{--}, and 0.094×10^{-24} cms^3 for Mg^{++}. We shall, then, ignore the polarisability of the magnesium ion and set $k_1 = \infty$. Y_1 then disappears from the equations.

The polarisation of the ion arises from the relative motion of the outer electrons and the core. The short range forces are expected to act mainly through these same electrons, which, in the shell model, form the shell of the ion. We assume that all short range forces act through the shell, i.e., $F = E = O$, giving $R = T = S$. Cowley et al (1963) present a rough justification for this procedure. We need now only consider one set of short range coupling coefficients.

6.8 Evaluation of the Parameters of the Theory in Terms of the Macroscopic Constants

The assumption that all short range forces act through the shell and that only forces between first and second nearest neighbours are important, reduces the number of parameters needed to describe these forces to five. If the polarisability of the positive ion is ignored, the theory contains the following 8 parameters.

$$
\left\{
\begin{array}{lll}
\text{Nearest neighbours} & A \\
\qquad\qquad '' & B \\
\text{2nd Nearest neighbours} & A'' \\
\qquad\qquad '' & B'' \\
\qquad\qquad '' & D'' \\
\end{array}
\right.
$$

Short range forces	
Ionic charge	Z
Shell charge	Y
Shell isotropic force constant	k

We make the following assumptions to reduce the number of parameters to six which may then be determined from the macroscopic constants. The ionic charge is assumed to be twice the electronic charge ($Z = 2$), and the forces between second nearest neighbours are assumed to be axially symmetric ($D'' = B''$). There is no justification for this second assumption in the case of ionic crystals, but the exact form assumed for the weaker second neighbour forces is unlikely to affect the results very much.

Smart's (1961) infra-red measurements give the following values for the infra-red dispersion frequency and the dielectric constants:

$$^*\nu_0 = 11.52 \times 10^{12} \text{ c/sec}$$
$$\epsilon_0 = 9.77$$
$$\epsilon_\infty = 2.94$$

These values give

$$R_0 = 23.56 \qquad (R_0 = S_{11} = -S_{12} = A + 2B)$$
$$Y = -2.64$$
$$k = 50.84$$

One other set of values is possible, but gives an imaginary frequency for the L.A. mode at (1, 0, 0).

Dae-Hyun Chung (1963) gives the following values for the elastic constants of magnesium oxide:

$$c_{11} = 28.917 \times 10^{11} \text{ dynes/cms}^2$$
$$c_{12} = 8.796 \qquad\qquad ''$$
$$c_{44} = 15.461 \qquad\quad ''$$

These values, together with the value already obtained for R_0, give

$$A = 32.31$$
$$B = -4.38$$
$$A'' = -2.50$$
$$B'' = 0.42 \quad (D'' = B'')$$

These values of the parameters have been used to draw contours of constant frequency for phonons with wave vectors in the (1, 0, 0) and (1, 1, 0) mirror planes and with polarisation vectors lying in the plane, and also to draw sections of the dispersion relation for various directions in these planes for comparison with the results of the neutron scattering experiments.

6.9 Degeneracy

Before the contour maps are introduced, it is of some interest to determine the types of degeneracy that can occur between the various branches of the dispersion relation. Landau and Lifshitz (1958) give an account of the degeneracies which occur between electron terms in a molecule which is readily applied to the present case.

Assume that two branches are near degenerate at wave vector q

$$M\boldsymbol{\xi}_1 = \omega_1^2 \boldsymbol{\xi}_1 \qquad \text{and} \qquad M\boldsymbol{\xi}_2 = \omega_2^2 \boldsymbol{\xi}_2$$

where $\omega_1 \approx \omega_2$

An eigenvector of the dynamical matrix for a point near q with frequency near ω_1 and ω_2 will be a linear combination of $\boldsymbol{\xi}_1$ and $\boldsymbol{\xi}_2$ to a first order of approximation:

$$\boldsymbol{\xi}(q + \delta q) = c_1 \boldsymbol{\xi}_1(q) + c_2 \boldsymbol{\xi}_2(q)$$
$$\text{write} \qquad M(q + \delta q) = M(q) + M'$$
$$\text{then} \qquad (M + M')\boldsymbol{\xi} = \omega^2 \boldsymbol{\xi}$$

---

*See, however, section 6.11

or $c_1(\omega_1^2 + M' - \omega^2)\boldsymbol{\xi}_1 + c_2(\omega_2^2 + M' - \omega^2)\boldsymbol{\xi}_2 = 0$

Form the scalar products of this expression with $\boldsymbol{\xi}_1$ and $\boldsymbol{\xi}_2$

$$c_1(\omega_1^2 + M'_{11} - \omega^2) + c_2 M'_{12} = 0$$
$$c_1 M'_{21} + c_2(\omega_2^2 + M'_{22} - \omega^2) = 0$$

where $M'_{ij} = \sum_{\substack{\alpha,\beta \\ k,k'}} \xi_{k,i}^\alpha M'^{\alpha,\beta}_{k,k'} \xi_{k',j}^\beta$

The solubility condition for these equations gives two possible values of ω

$$\begin{vmatrix} \omega_1^2 + M'_{11} - \omega^2 & M'_{12} \\ M'_{21} & \omega_2^2 + M'_{22} - \omega^2 \end{vmatrix} = 0$$

or

$$\omega_1^2 = \frac{1}{2}\left(\omega_1^2 + \omega_2^2 + M'_{11} + M'_{22}\right) \pm \left\{\frac{1}{4}\left(\omega_1^2 - \omega_2^2 + M'_{11} - M'_{22}\right)^2 + (M'_{12})^2\right\}^{\frac{1}{2}}$$

where we have used the fact that $M'_{21} = M'_{12}$. For a degenerate solution, two conditions must be fulfilled:

$$\omega_1^2 - \omega_2^2 + M'_{11} - M'_{22} = O$$
and $$M'_{12} = 0$$

If we allow $\boldsymbol{q}$ to have s dimensions, the dispersion relation is a surface in $(s+1)$ dimensional space, and degeneracies occur in general in a manifold of $(s-2)$ dimensions. However, it can happen that, from symmetry considerations, M'_{12} is always zero. This is the case when we can divide the branches into symmetry types, and branches 1 and 2 belong to different types. In this case only one condition remains, and degeneracy occurs in a manifold of $(s-1)$ dimensions. We shall distinguish three different cases.

(1) $\boldsymbol{q}$ general $(s = 3)$ The dispersion relation is a surface in 4 dimensional space. No division into symmetry types is possible. Degeneracies between branches occur along lines in reciprocal space.

(2) $\boldsymbol{q}$ in a mirror plane $(s = 2)$
The dispersion relation is a surface (in 3 dimensional space). The branches may be divided into two symmetry types; those with polarisation vectors perpendicular to the plane, and those with polarisation vectors in the plane. Degeneracy between perpendicular and parallel types occurs along lines in the plane, but degeneracy between like types occurs only at isolated points.

(3) $\boldsymbol{q}$ in a symmetry direction $(s = 1)$
The dispersion relation is a line. The branches may be divided into 3 symmetry types, L, T_1 and T_2 where the polarisation vectors of the L type are parallel to the symmetry direction, and those of the T_1 and T_2 types are perpendicular to the symmetry direction. Degeneracy is

73

possible only between unlike types, when it will in general occur at points. Since degeneracy between, say, the two L branches is impossible, they may be labelled LO and LA, depending on their behaviour at the origin, without risk of confusion at points away from the origin. In the case of the T_1 and T_2 branches in the (1,0,0) direction in a cubic crystal, the first condition is also satisfied from symmetry considerations, and the branches are degenerate for all $\boldsymbol{q}$ in this direction.

It can be shown that the gradient of the dispersion relation and the polarisation vectors change continuously along a line in the dispersion relation which passes through a degeneracy. Let us move a distance $\alpha\boldsymbol{\delta q}$ from our original point towards the degeneracy

$$M(\boldsymbol{q} + \alpha\boldsymbol{\delta q}) = M(\boldsymbol{q}) + \alpha M'$$

With $\alpha = 1$ we reach the degeneracy, so M' satisfies the two conditions already found. The equations for c_1 and c_2 become

$$c_1(\omega_1^2 + \alpha M'_{11} - \omega^2) = 0$$
$$c_2(\omega_2^2 + \alpha M'_{22} - \omega^2) = 0$$

where we have used the fact that $M'_{12} = 0$. If $c_1 \neq 0$ and $c_2 \neq 0$, we must have $\alpha = 1$ for the above equations to be true. If $c_1 \neq 0$ and $c_2 = 0$

$$\omega^2 = \omega_1^2 + \alpha M'_{11}$$
$$\text{or} \qquad \omega = \omega_1 + \frac{\alpha}{2}\frac{M'_{11}}{\omega_1}$$

If $c_2 \neq 0$ and $c_1 = 0$

$$\omega^2 = \omega_2^2 + \alpha M'_{22}$$
$$\text{or} \qquad \omega = \omega_2 + \frac{\alpha}{2}\frac{M'_{22}}{\omega_2}$$

c_1 and c_2 cannot both be zero if we are to have $\boldsymbol{\xi} = c_1\boldsymbol{\xi}_1 + c_2\boldsymbol{\xi}_2$. The frequencies are seen to be linearly dependent on α, and the polarisation vector does not change along the line through the degeneracy.

In the case of point degeneracies between branches of like symmetry types in a mirror plane, the M'_{ij} are linear functions of the two components of the wave vector. The equation for the frequencies then gives a dispersion relation in the form of an elliptic cone. The following diagram shows the form of the dispersion relation near the degeneracy, and the changes in polarisation vector that would occur in say the upper surface in the region of the degeneracy. If the polarisation vectors at the point P are $\boldsymbol{\xi}_1$ and $\boldsymbol{\xi}_2$ for the upper and lower surfaces respectively, the polarisation vectors for the upper surface at other points are of the form $\boldsymbol{\xi} = c_1\boldsymbol{\xi}_1 + c_2\boldsymbol{\xi}_2$, and these are drawn as lines at an angle ϕ to the q_1 axis where $\tan\phi = \frac{c_1}{c_2}$. The lines represent the polarisation vectors in a conventional way for the two component vectors obtained in the case of a Bravais lattice. The polarisation vectors of say the upper surface on opposite sides of the degenerate point are orthogonal.
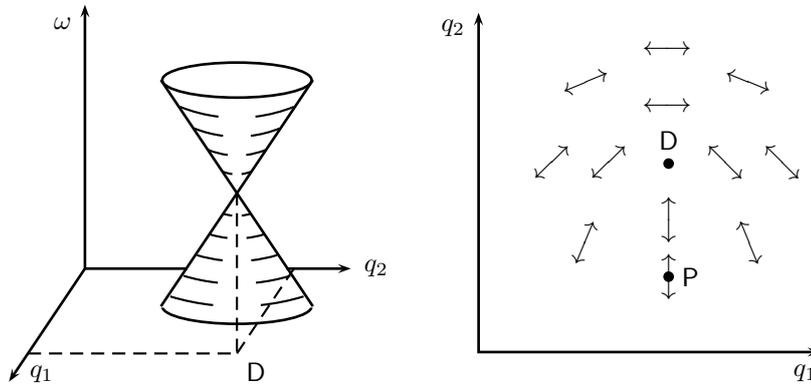
Figure 6.3: The dispersion relation in the neighbourhood of a degeneracy

6.10 Preparation of the Contour Maps

The experimental measurements enable the phonon dispersion relation to be determined for phonons with wave vectors in a mirror plane, and with polarisation vectors parallel to the plane. Contour maps of the theoretical dispersion relation have been prepared for the four branches of the dispersion relation in the (1,0,0) and (1,1,0) mirror planes which have polarisation vectors parallel to the planes. It has been shown that these branches are degenerate only at isolated points, and so may be separated readily and displayed as four separate surfaces each represented by its own contour map. If, for any wave vector, the four solutions of the secular equation are arranged in order of descending frequency, branch 1 describes the behaviour of the first solution as a function of
wave vector, branch 2 that of the second solution, etc. To draw each contour of constant frequency, the secular determinant

$$\Delta = \det\left(M_{k,k'}^{\alpha,\beta} - \omega^2 \delta_{\alpha\beta}\delta_{kk'}\right)$$

was evaluated for the particular frequency for values of the wave vector forming a grid of points in reciprocal space, so spaced that there were 40 points between the origin and the point (1,0,0), and between the origin and the point (1,1,0). The Stretch computer was used to make these calculations, and a library routine used to interpolate the contour $\Delta = 0$ between the grid points and to prepare the output for the automatic graph plotter. The interpolation formula is quadratic and uses six values of Δ on the sides of a triangle to determine
the contour within the triangle. Each contour was initially drawn on a separate sheet, and the various disconnected parts of the contour were allocated to one of the four branches with the aid of some additional frequency calculations where necessary. The contours were then traced to form four contour maps. Symmetry directions are shown by full lines, and the symmetry classification of the branch is written beside the line. This classification changes at degenerate points. The optic branches are normally identified by their behaviour at a lattice point. However, it has been shown that in a symmetry direction, two branches of the same symmetry type (i.e., LO and LA or TO and TA) cannot be
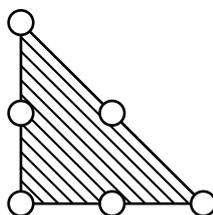
Figure 6.4: The six points used by the interpolation formula to determine the contour within the shaded area

degenerate. Consequently, the optic branch may also be defined as the branch of a given symmetry type of higher frequency. This second definition is used in the symmetry direction where q takes the form $(0, \zeta, 1)$, as this direction does not pass through a lattice point.

Degenerate points have been marked and their frequencies given. An iterative method based on the equations of section 6.8 was used to locate these points in regions where the shape of the contours suggested a possible degener- acy. It is possible that there are other degenerate points that are not marked. Symmetry arguments show that some degeneracies must occur. For instance, the degeneracies at the point $(0,1,1)$ in the $(1,0,0)$ plane must occur there from symmetry. In the $(1,1,0)$ plane we can show that there must be degeneracies between the L0 and T0 and between the LA and TA branches somewhere along the path joining the three points $(0,0,0)$, $(0,0,1)$ and $(1, \bar{1}, 1)$. If we assume that the degeneracy does not occur between the first two points, since L is above T at the origin, L must still be above T at $(0,0,1)$. In the new symmetry direction towards $(1, \bar{1}, 1)$, the classification of the branches changes, and L and T are interchanged. Hence T is above L. However, at $(1, \bar{1}, 1)$, a lattice point, L is above T and, therefore, there must be a degeneracy between the last two points. This argument applies to both optic and acoustic modes.
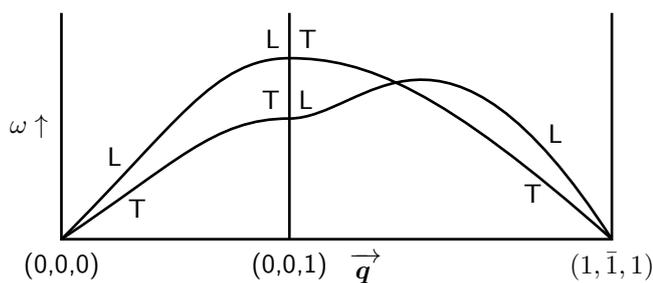
Figure 6.5: Degeneracies in the (1,1,0) plane
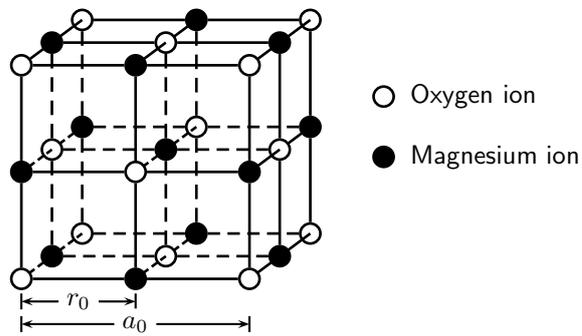
The structure of magnesium oxide

O Oxygen ion

● Magnesium ion

$\boxed{\diagdown}$ (1, 0, 0) plane

$\boxed{\diagdown}$ (1, 1, 0) plane
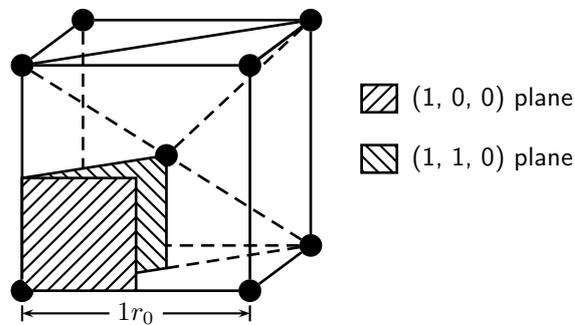
The reciprocal lattice of magnesium oxide, showing the portions of the mirror planes covered by the contour maps

———	Symmetry direction
– – – –	Brillouin zone boundary
●	Reciprocal lattice point
○	Point of high symmetry $((1, 0, 0)$ or $(1/2, 1/2, 1/2))$
⊙	Degeneracy with branch above
⊕	Degeneracy with branch below

The contour interval is 10^{12} c/sec

Spot frequencies are in units of 10^{12} c/sec

Figure 6.6: Key to contour map (figs. 6.7 to 6.14)
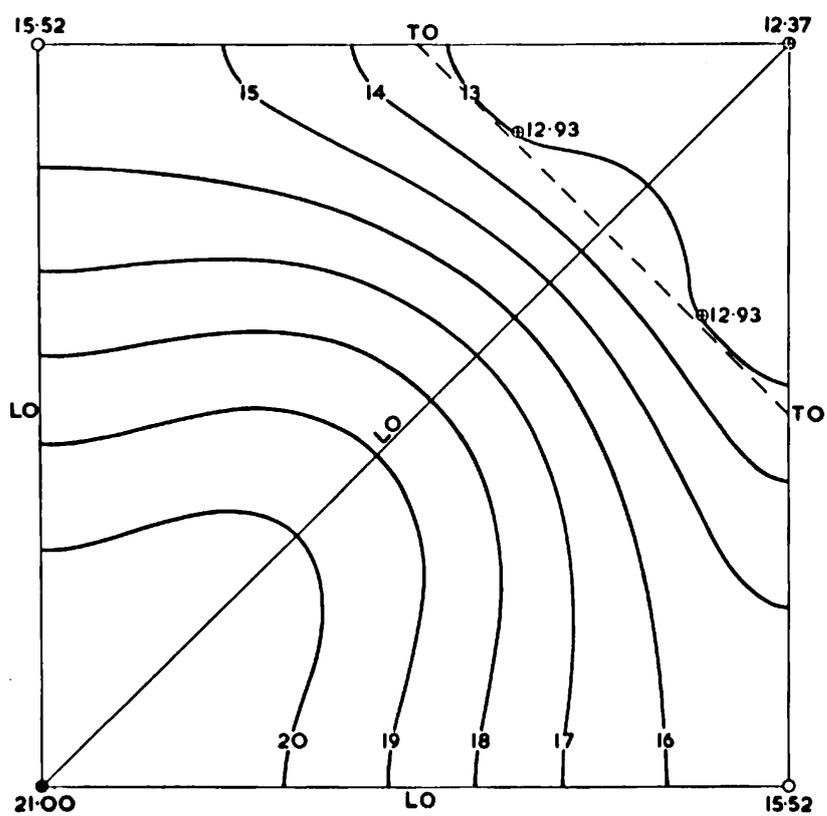
Figure 6.7: (1 0 0) plane branch 1

78
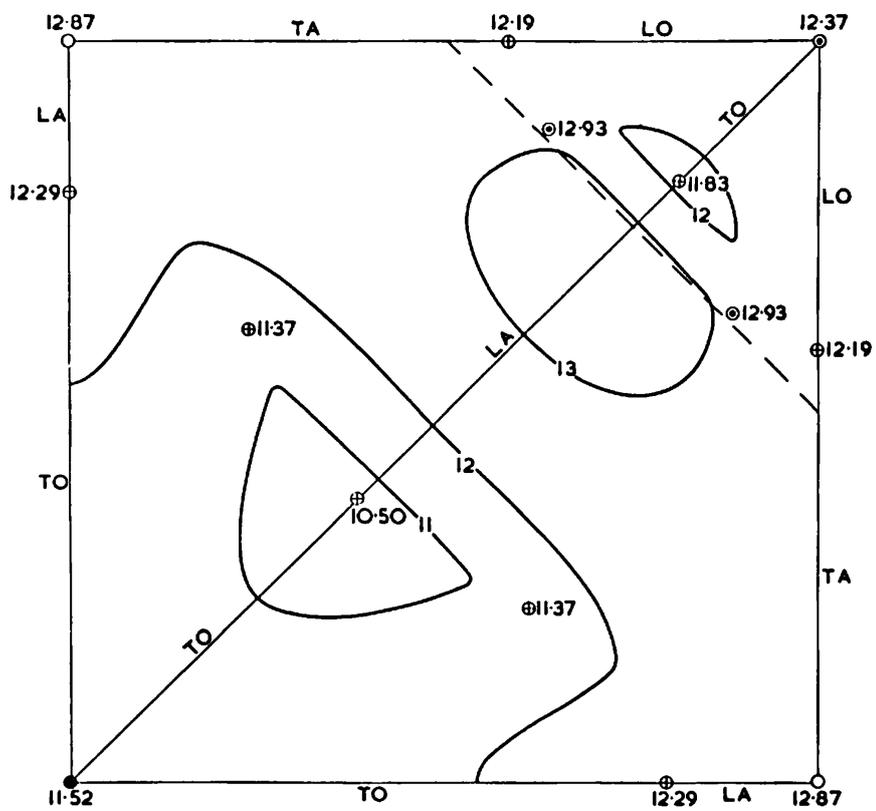
Figure 6.8: (1 0 0) plane branch 2
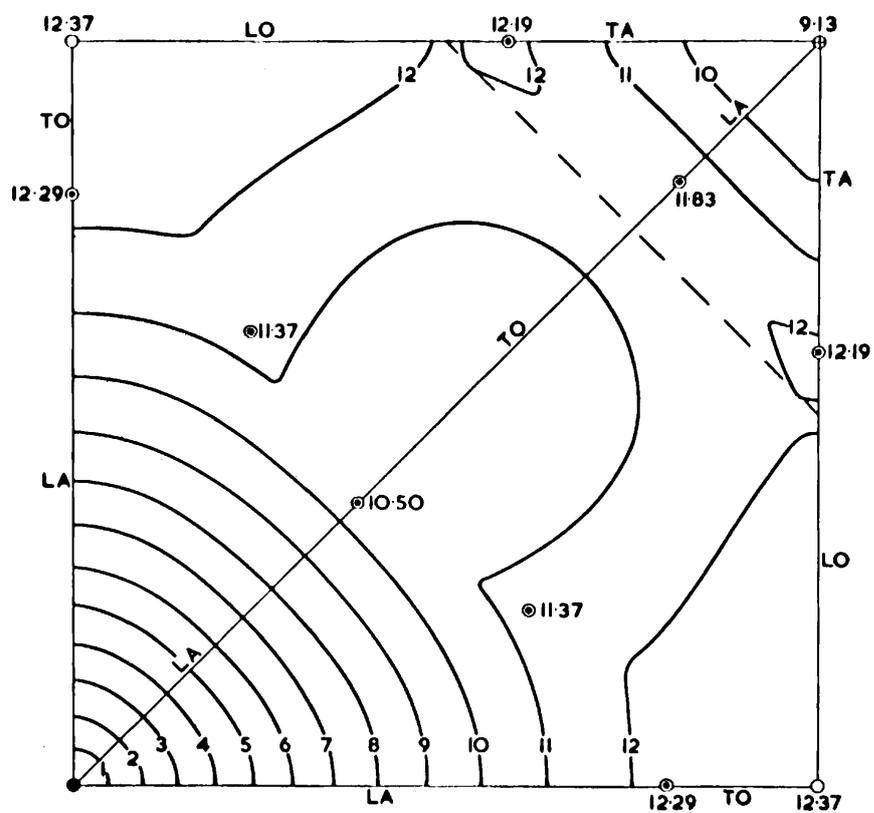
Figure 6.9: (1 0 0) plane branch 3
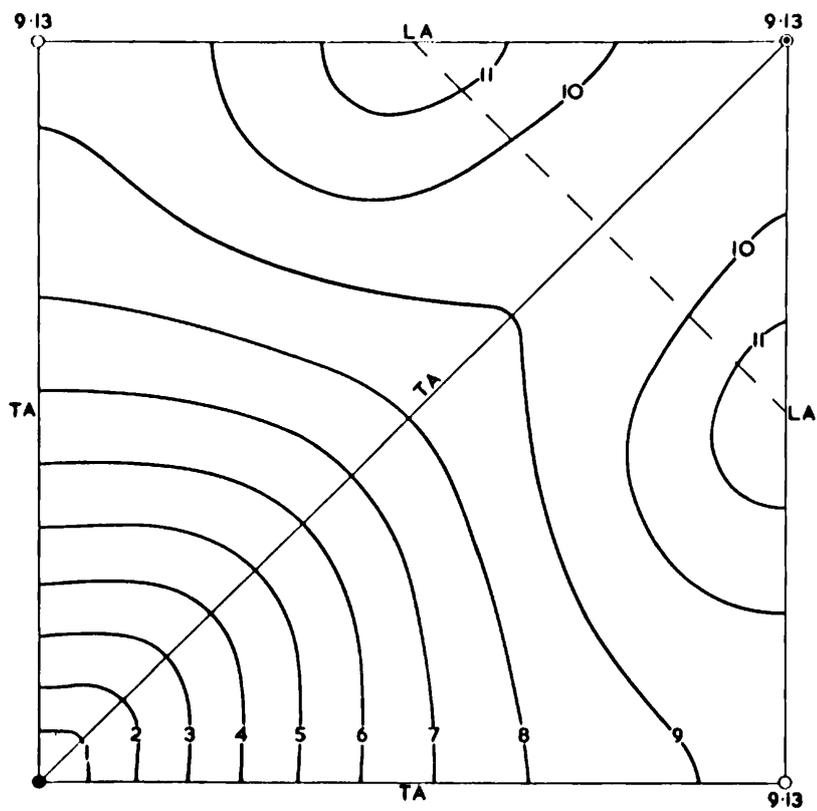
Figure 6.10: (1 0 0) plane branch 4
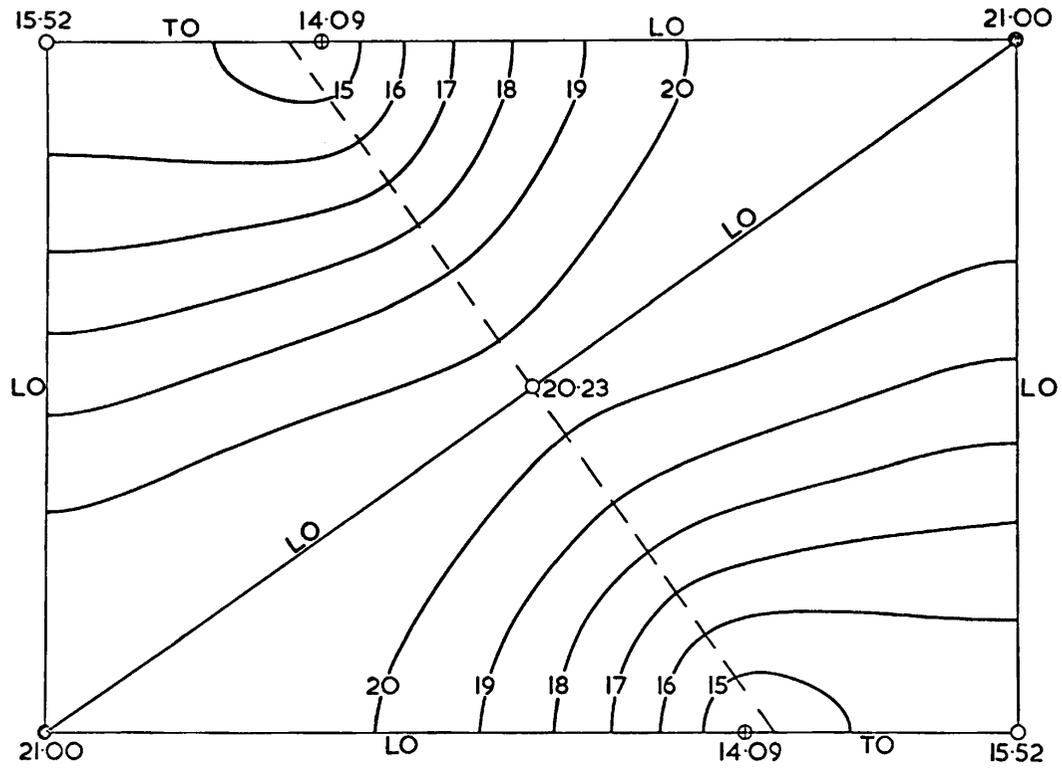
Figure 6.11: (1 1 0) plane branch 1
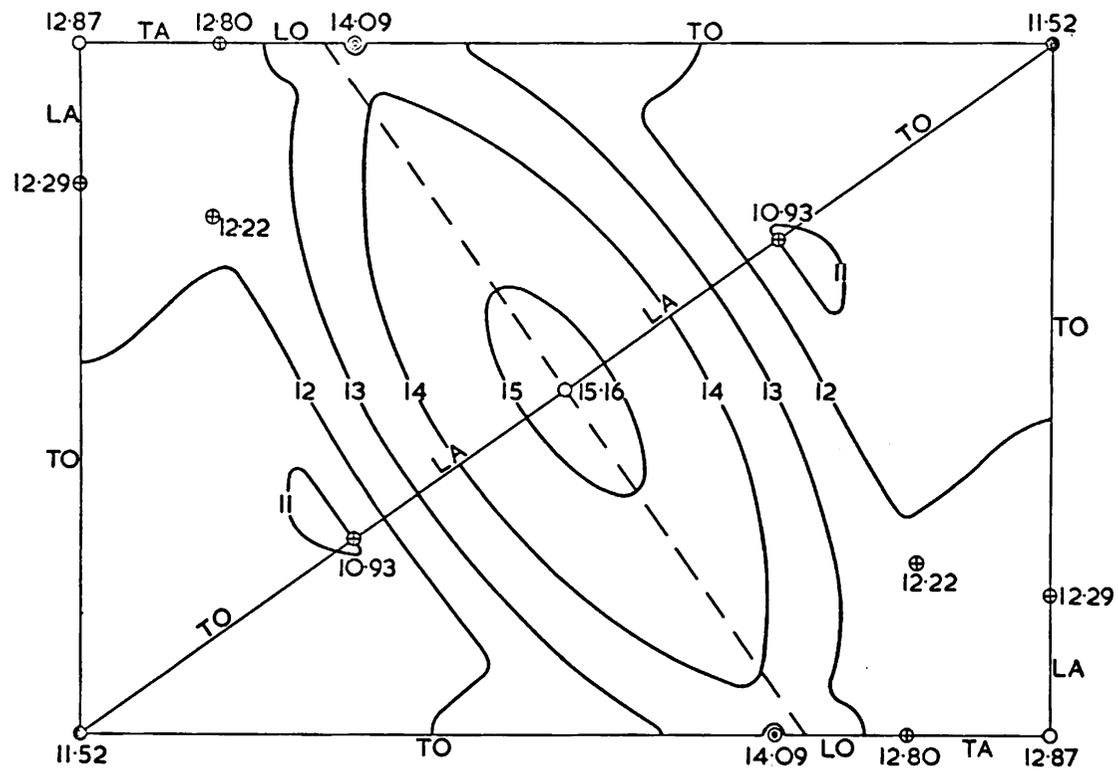
Figure 6.12: (1 1 0) plane branch 2
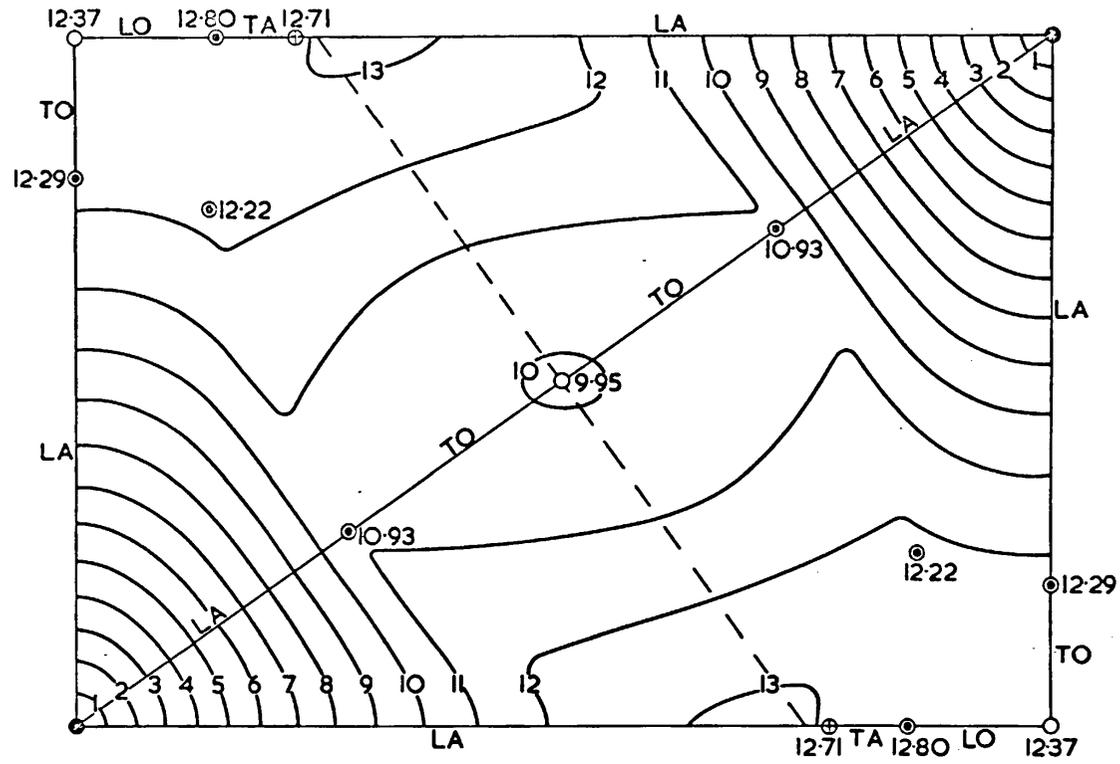
Figure 6.13: (1 1 0) plane branch 3
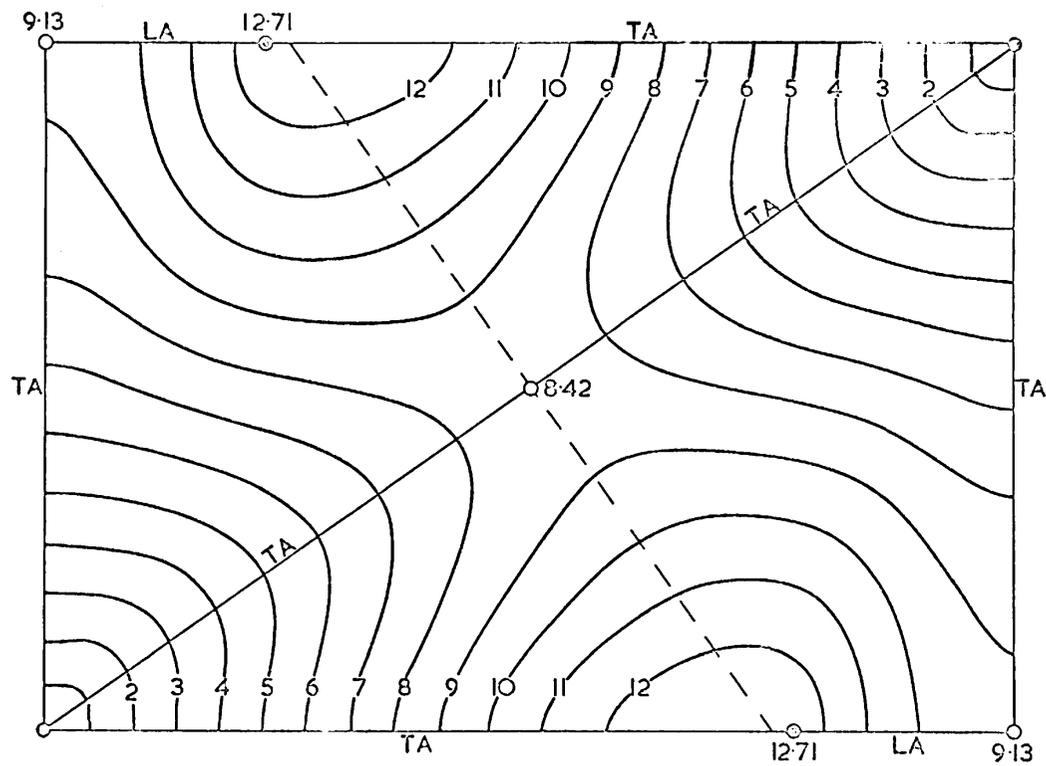
Figure 6.14: (1 1 0) plane branch 4

6.11 The Infra-Red Dispersion Frequency for Magnesium Oxide

The infra-red dispersion frequency is the frequency occurring in the denominator of equation 6.2. It may be found from infra-red measurements. Field, Smart and Wilkinson (l964) give two values for the dispersion frequency:-

(a) 394 cms^{-1} This value is based on a measurement of the infra-red absorption of a thin film of magnesium oxide

(b) 403 cms^{-1} This value is based on a Kramers-Krönig analysis of the reflection spectrum. This is a revised value. Smart gives the value 384 cms^{-1} in his thesis,and,this vaLue was used in the previous calculations, but apparently there were errors in his analysis (Field, private communication).

Von Häfele (1963) has measured the infra-red reflectivity of magnesium oxide, and obtained the following value for the dispersion frequency:

(c) 394 cms^{-1} Reflection measurements were made at two different angles of incidence, and the Kramers-Krönig analysis avoided.

Kramers-Krönig analysis depends on a general property of complex functions which involves integrals over an infinite range. To perform these integrals, the reflectivity must be known over an infinite range of frequencies. This type of analysis requiring an infinite range of experimental data is not usually very satisfactory. The value of 394 cms^{-1} (= 11.81×10^{12} c/sec) based on a direct absorption measurement has therefore been chosen. This value agrees with that obtained by von Häfele. The values of the dielectric constants have also been taken from Born and Huang (1954), Table 17, rather than from the infra-red measurements. The agreement, however, is very good and this involves little change. Revised parameters have been calculated, and the frequencies at points of high symmetry are compared with the original values.

Table 6.5: Data on which Model is Based

	c_{11}	c_{12}	c_{13}	ϵ_0	ν_0	ϵ_∞
	(10^{11} dynes/cms^2)				(10^{12} c/sec)	
Original data	28.917	8.796	15.461	9.77	11.52	2.94
Revised data	″	″	″	9.8	11.81	2.95

Table 6.6: Shell Model Parameters

	A	B	A''	B''	Z	Y	k
Original	32.31	-4.38	-2.50	0.422	2	-2.641	50.84
Revised	32.43	-4.26	-2.57	0.365	″	-2.782	58.36

Table 6.7: Calculated Frequencies (10^{12} c/sec)

$(0,0,0)$	L.O.	21.00	21.53
	T.O.	11.52	11.81
$(1,0,0)$	L.O.	15.52	15.42
	L.A.	12.87	12.83
	T.O.	12.37	12.50
	T.A.	9.13	9.05
$(\frac{1}{2}, \frac{1}{2}, \frac{1}{2})$	L.O.	20.22	20.29
	L.A.	15.16	15.44
	T.O.	9.95	10.05
	T.A.	8.42	8.58

The revised frequencies differ little from those originally calculated.

Chapter 7

The Phonon Dispersion Relation of Magnesium Oxide – Experimental

7.1 Introduction

The shell model has been used with considerable success to describe the crystal dynamics of the alkali halides. It is of some interest to see if the same theory (as discussed in Chapter 6) can describe as successfully the dynamics of a crystal such as magnesium oxide which is considered to be not as purely ionic in character as the alkali halides. Both magnesium and oxygen have high coherent cross sections and low incoherent and absorption cross sections, which makes magnesium oxide suitable for the type of experiment described in this thesis. However, the calculations of Chapter 6 show that phonons with frequencies up to 21×10^{12} c/sec are present. The population factor, P_j, in the cross section formula 2.3 becomes very small for experiments in which neutrons gain energy from phonons of such high frequency. In fact very few phonons from the branch with the highest frequency were observed. Apparatus was constructed to overcome this restriction by the use of a neutron energy loss technique, and is described in Chapter 8. Unfortunately, no results have yet been obtained with this apparatus.

page 167

page 168

The frequencies of 656 phonons were determined. 388 of these had wave vectors parallel to the (1,0,0) mirror plane, and 268 wave vectors parallel to the (1,1,0) mirror plane. Each plane has been divided into a series of sectors 5° wide, and for each sector graphs of frequency against wave vector amplitude have been plotted for all phonons with wave vectors lying in the sector. Sections of the theoretical dispersion relation along the centre line of the sectors are shown on the same graphs. An attempt has been made to identify the branch to which a phonon belongs by comparing the theoretical and observed intensities of the peaks in the time of flight spectrum. This has not been altogether successful.

The theory is found to agree quite closely with the experimental points. The portions of the branches which become T0 in symmetry directions have slightly lower frequencies than the experimental results indicate, and the branch with the highest frequency lies above the experimental points in the neighbourhood of the point (1,0,0). Very few points have been obtained on this latter branch except near the zone boundary where its frequency is comparatively low.

page 169

7.2 Apparatus

This experiment made use of the cold neutron apparatus described in Chapter 3. Rotor 5 in Table 3.1 was used. At first three LiF-ZnS scintillator detectors were mounted above the sample in the shielding shown in fig. 3.2. These detectors are described in section 3.7. Most of the results for phonons with wave vectors parallel to the (1,1,0) mirror plane were obtained with the apparatus in this form. The detector shielding was later extended (figs. 3.1 and 3.3) to

house 12 detectors, and the results for the (1,0,0) plane were obtained with the 12 detectors.

Two different magnesium oxide crystals were used. One had a (1,1,0) mirror plane perpendicular to its longest axis, and so was conveniently shaped for measurements in this plane. The other had a (1,0,0) mirror plane perpendicular to its longest axis and was used for measurements in this plane. The *mosaic spread* of both crystals, given by neutron rocking curves, was about 0.3° standard deviation. It is probable that this is not a true mosaic spread, but that the crystals consisted of several parts which had slightly different orientations.

The crystals were oriented with their mirror planes parallel to the scattering plane by means of the techniques described in Appendix III. Full use was made of the automatic features of the goniometer (Peckham, 1964c). Several crystal angles were set in advance, and the crystal was automatically turned to the next angle when a preset number of beam monitor counts had been accumulated. Counting periods of about 18 hours were necessary to obtain time of flight spectra for each crystal orientation. Two typical spectra are shown in fig. 7.1. The liquid hydrogen moderator was available for the whole of this experiment.

The various stages in the reduction of the data are described in Chapter 4. Initially, the time of arrival of each neutron was recorded on magnetic tape. Time of flight spectra were obtained from the magnetic tape by the analyser. The I.B.M. computer was used to find peaks in the time of flight spectra and to determine their positions. Phonon frequencies and wave vectors were calculated from the peak positions by the Ferranti *Mercury* computer.

7.3 Results

Sections of the reciprocal lattice in the (1,0,0) and (1,1,0) mirror planes are shown in fig.7.2. The Brillouin zone boundaries are shown as broken lines. The symmetry of the lattice is such that the dispersion relation is completely determined if the frequencies corresponding to wave vectors-lying in one half of the areas shown are given. These regions have been divided into 5° wide sectors as shown in the diagram. The sectors are labelled A1, A2, . . . , A9 in the (1,0,0) plane, and B1, B2, . . . , B18 in the (1,1,0) plane. A reduced wave vector lying in one of these sectors has been calculated for each observed phonon. A section of the dispersion relation is obtained by plotting the frequencies against the reduced wave vector amplitudes of all phonons with reduced wave vectors lying in a given sector. These sections, labelled with the sector number, are shown in figs. 7.5 to 7.18. Sections of the theoretical dispersion relation, in directions along the centre line of each sector, have been taken from the contour maps given in Chapter 6.

A standard deviation error in the frequency of each phonon was calculated in the way described in Chapter 4. The errors were found to depend strongly on the frequency, as the neutron groups corresponding to the higher frequency phonons were very much weaker (see the behaviour of the population factor in fig. 3.14). Average errors have been calculated for phonons with frequencies between 0 and 2, 2 and 4, 4 and 6, etc. $\times 10^{12}$ c/sec. The curve in fig.7.3 is a smooth curve which gives approximately these errors.

89
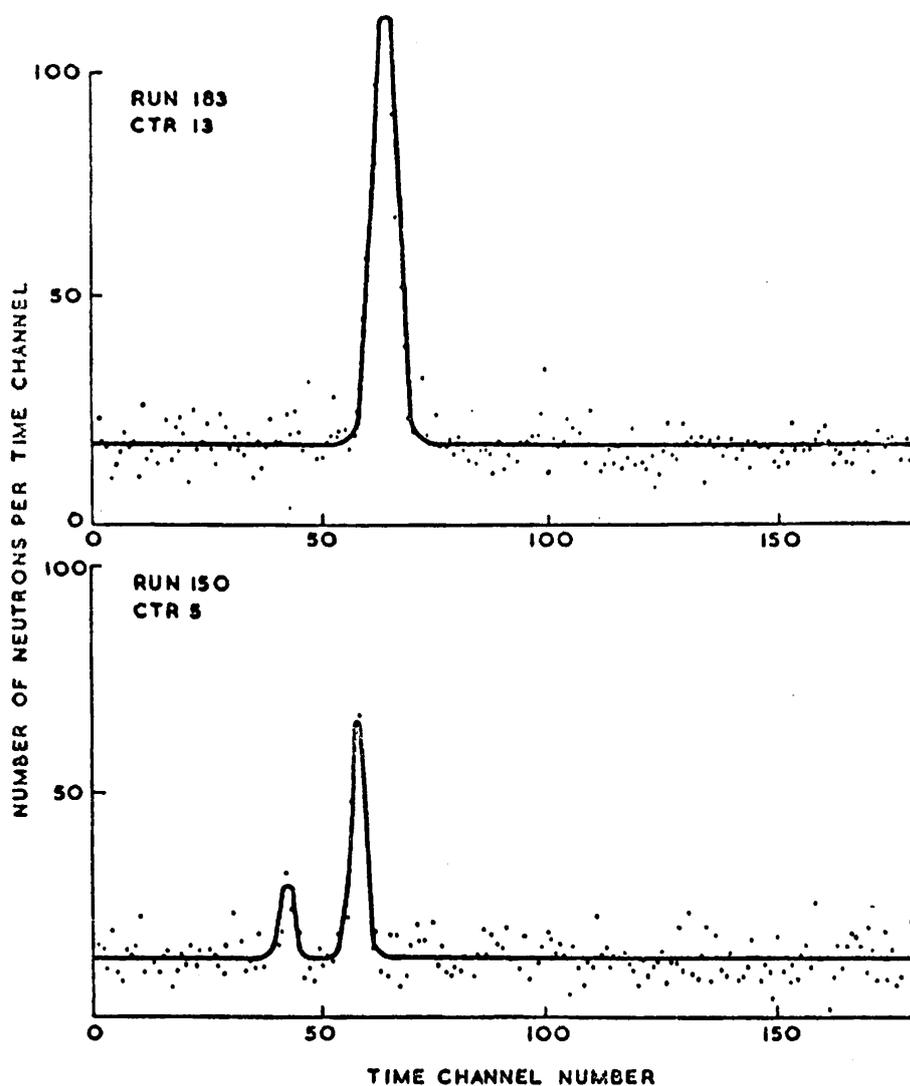
Figure 7.1: Neutron time of flight spectra from MgO

7.4 Resolution

A function, which is the sum of two similar Gaussian peaks, shows a central dip only if the separation of the peaks is greater than the sum of their standard deviations. It would be unlikely that two peaks in a time of flight spectrum would be resolved if they were so close together that they did not show a central dip. This resolution criterion is to some extent arbitrary, but must be of the right order of magnitude. Fig. 3.14 shows that the resolution of the apparatus at a phonon frequency of 12×10^{12} c/sec is about 3%, or 0.36×10^{12} c/sec. Two branches of the dispersion relation will be unresolved if they are separated by less than about 0.7×10^{12} c/sec. The position assumed for the combined peak will lie somewhere between the two branches and depends on the intensities of
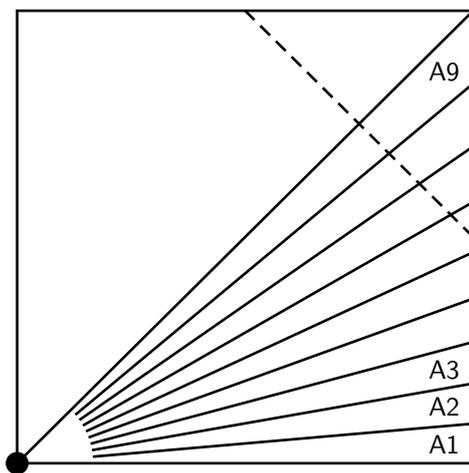
(1, 0, 0) Plane
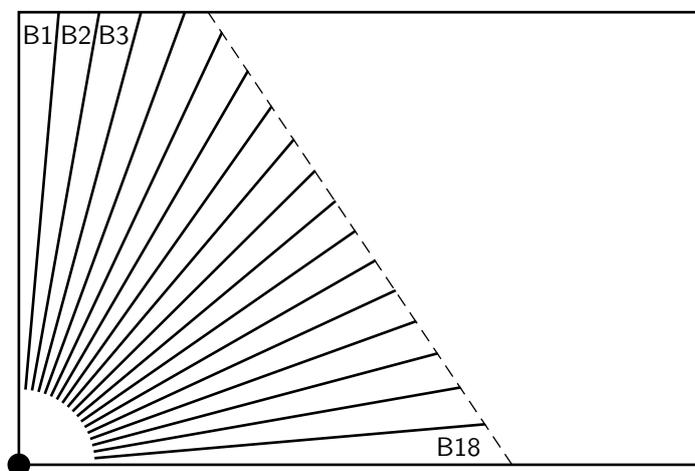
(1, 1, 0) Plane

Figure 7.2: Sections of the reciprocal lattice of magnesium oxide showing the positions of the sectors. The areas shown are shaded in Fig. 6.6
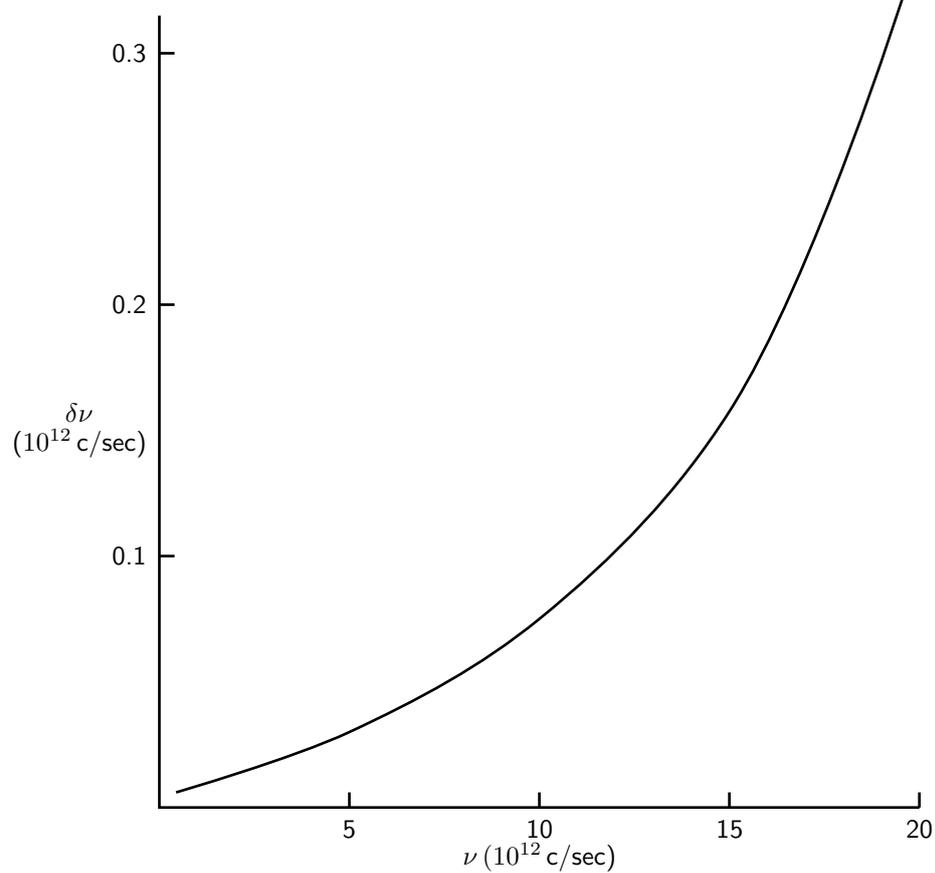
Figure 7.3: Experimental error $(\delta\nu)$ (standard deviation) as a function of phonon frequency (ν)

Figure 7.4: Key to figs. 7.5 to 7.18

Experimental points have been allocated to one of the four branches of the dispersion relation on the basis of observed intensity.

Symbol	Branch
△	1
▽	2
▲	3
▼	4
◯	Unknown
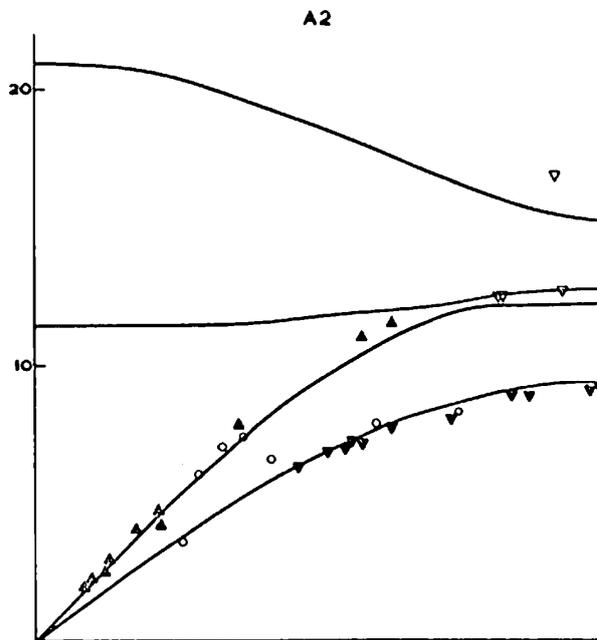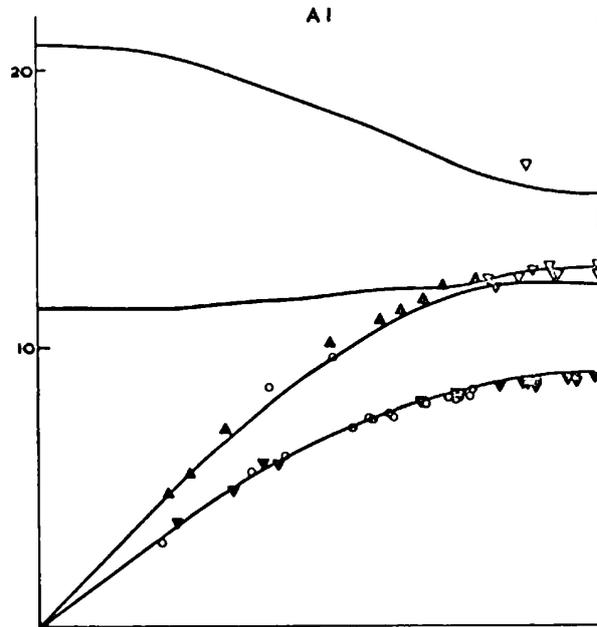
Figure 7.5
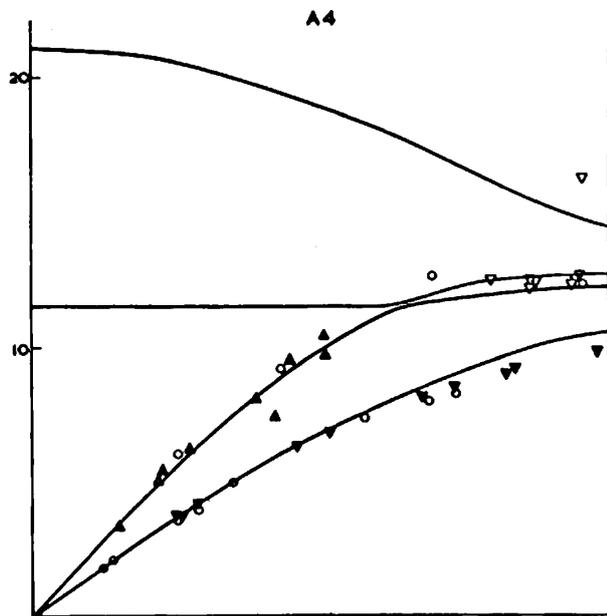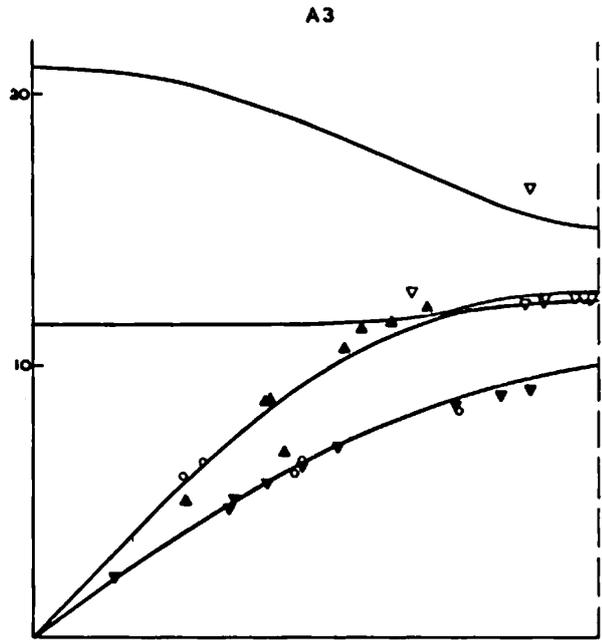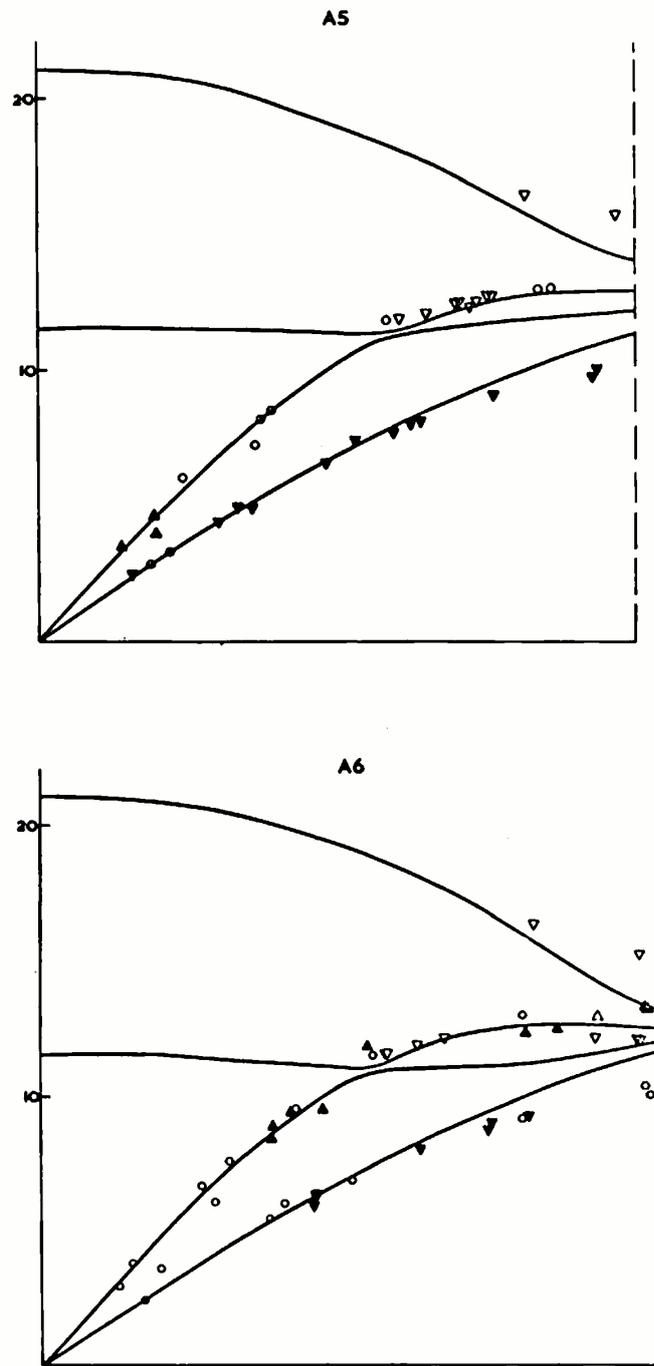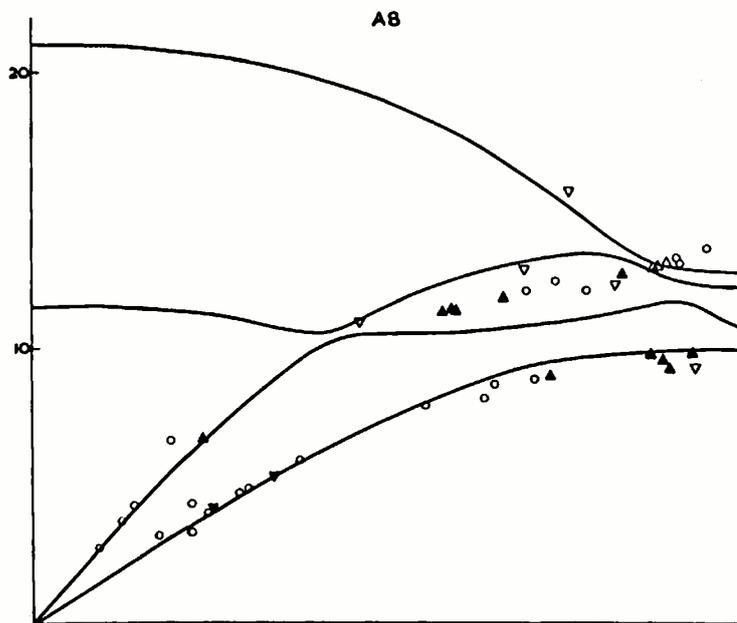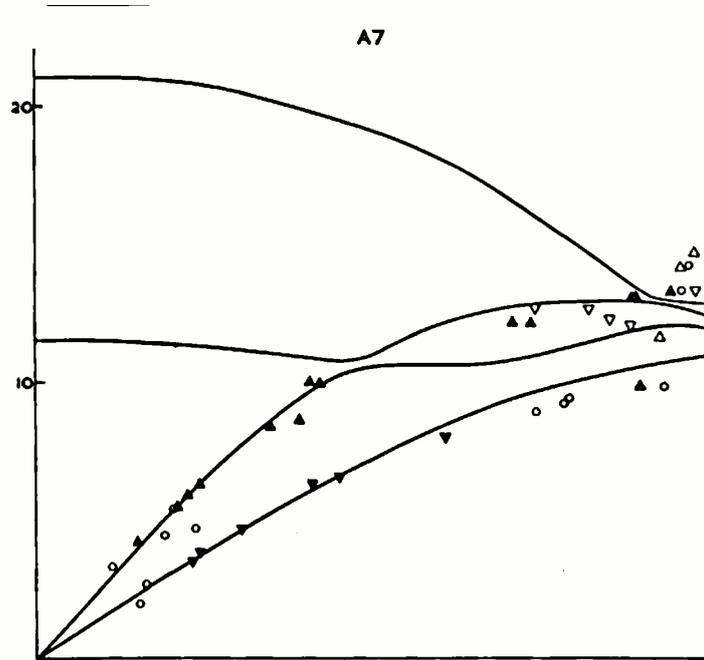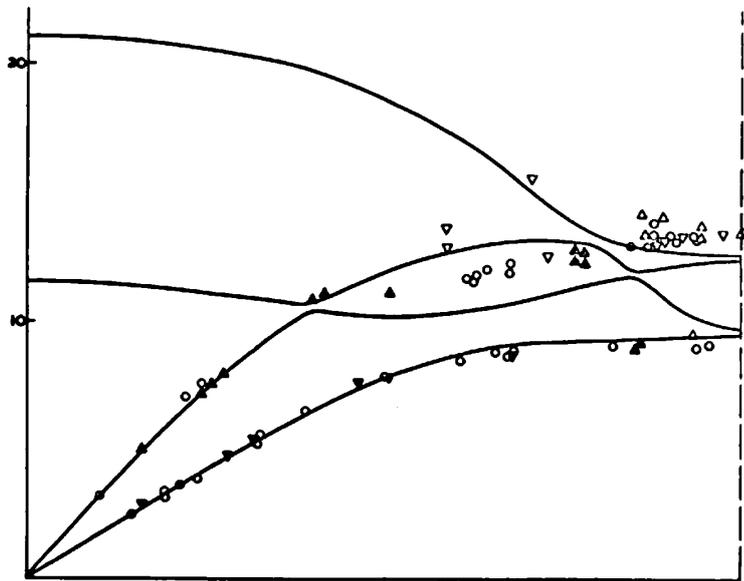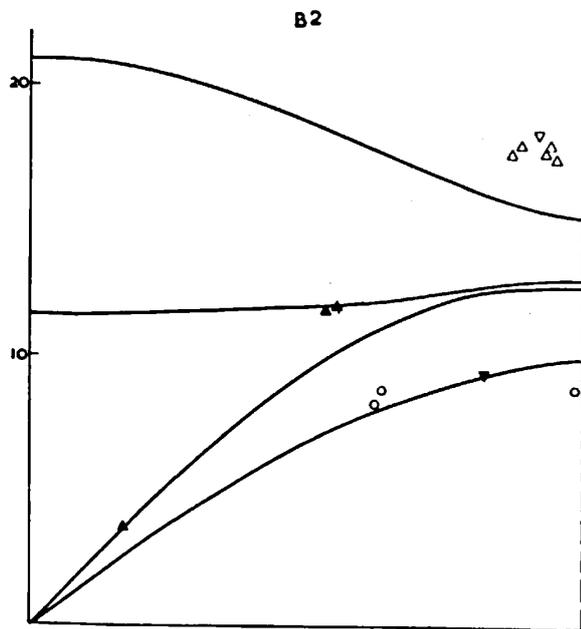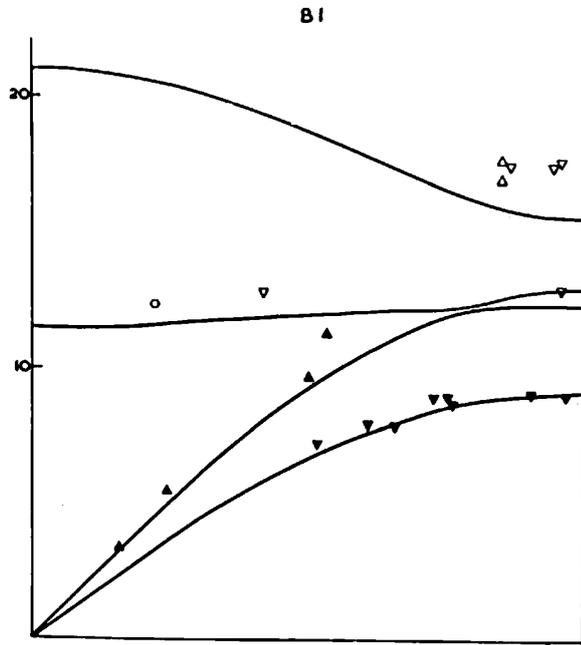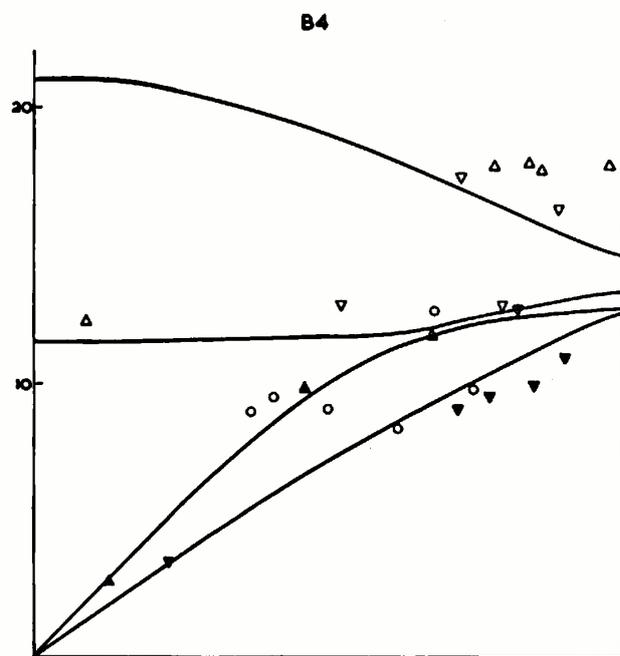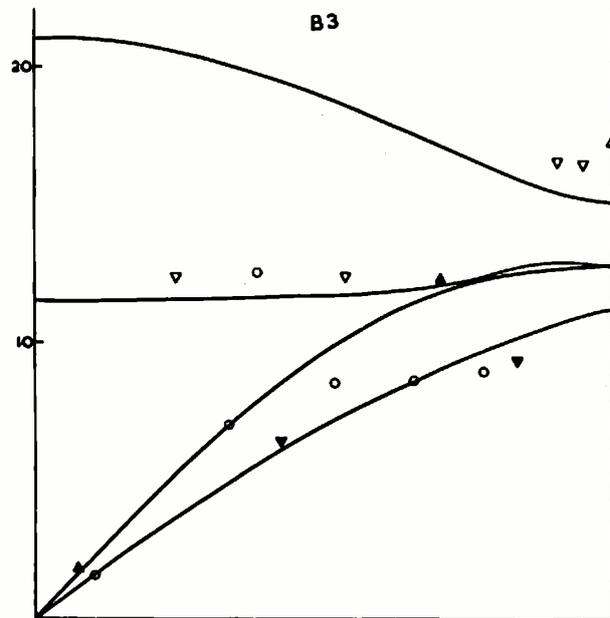
A3

A4

Figure 7.6

A5

A6

Figure 7.7

95

Figure 7.8

96

A9

Figure 7.9

B 1

B 2

Figure 7.10

98

Figure 7.11

B5

B6

Figure 7.12

100

Figure 7.13

B9

BIO

Figure 7.14

B II

B I2

Figure 7.15

103

Figure 7.16

104

BI5

BI6

Figure 7.17

B17

B18
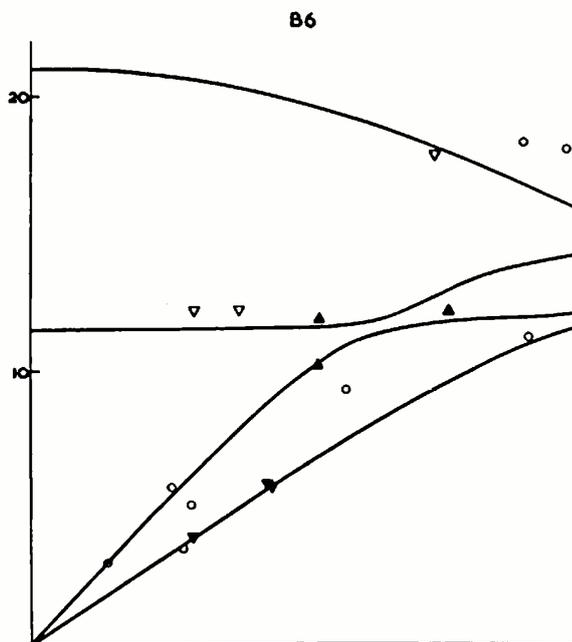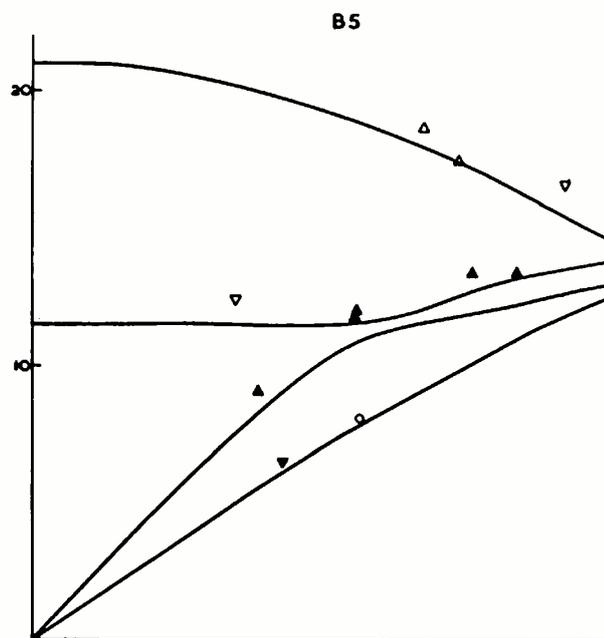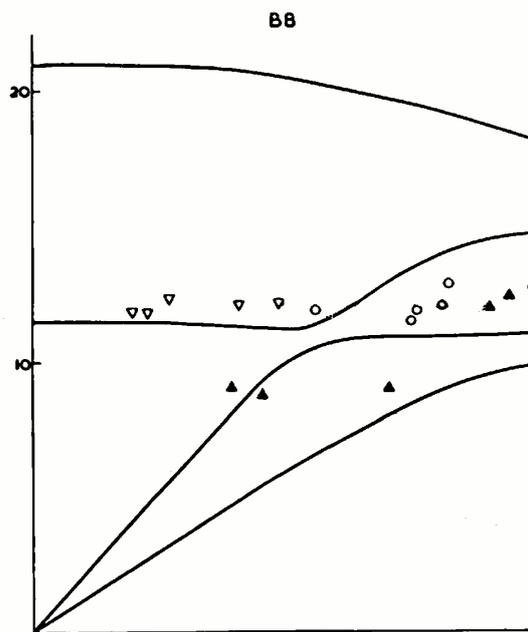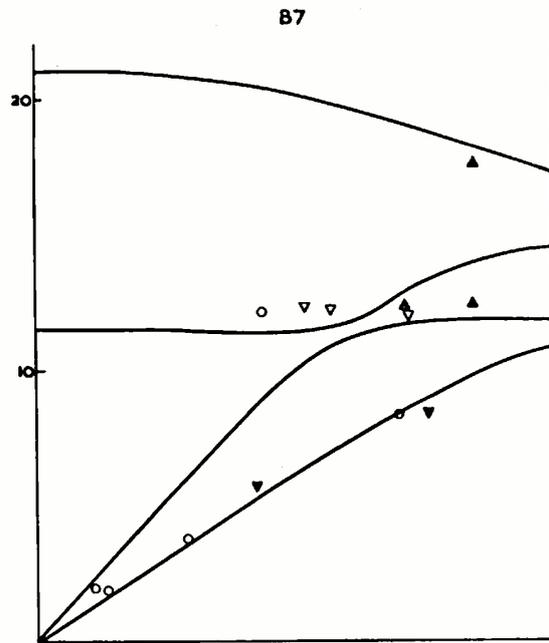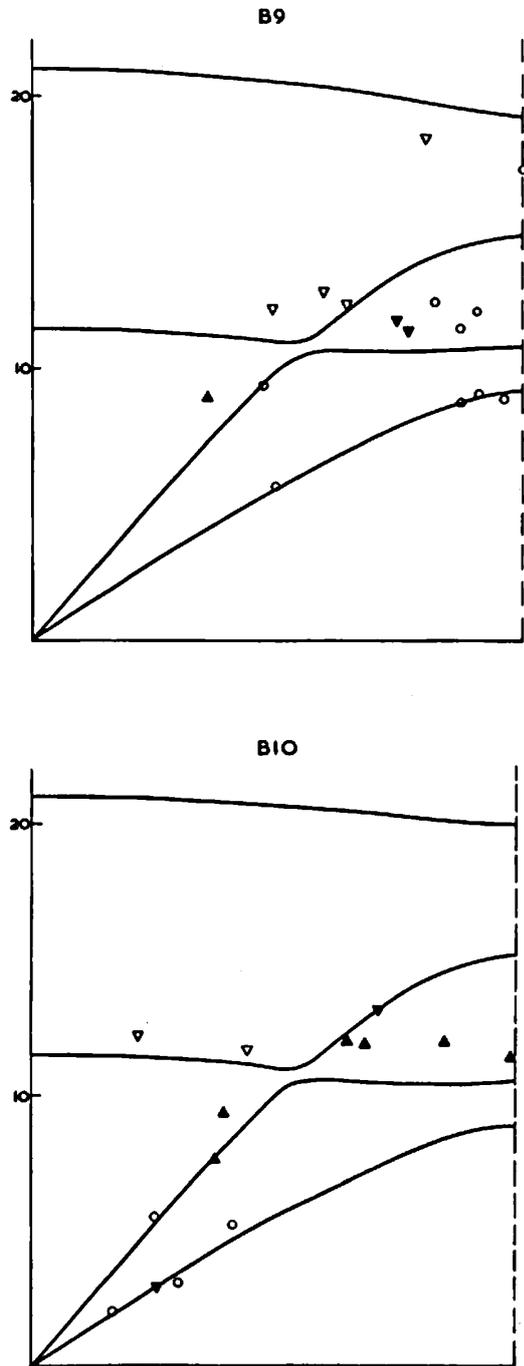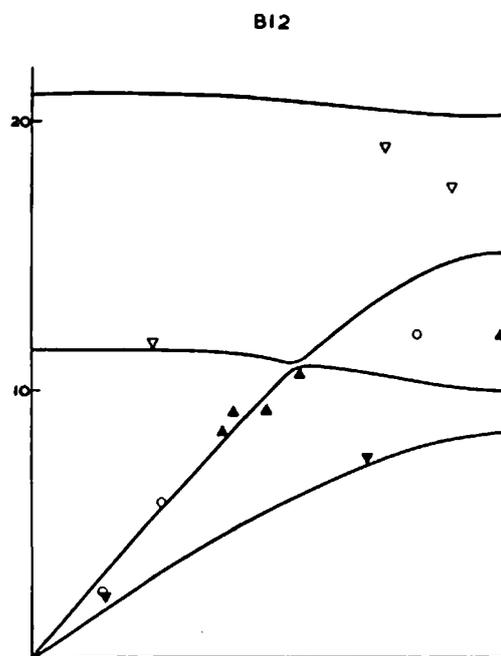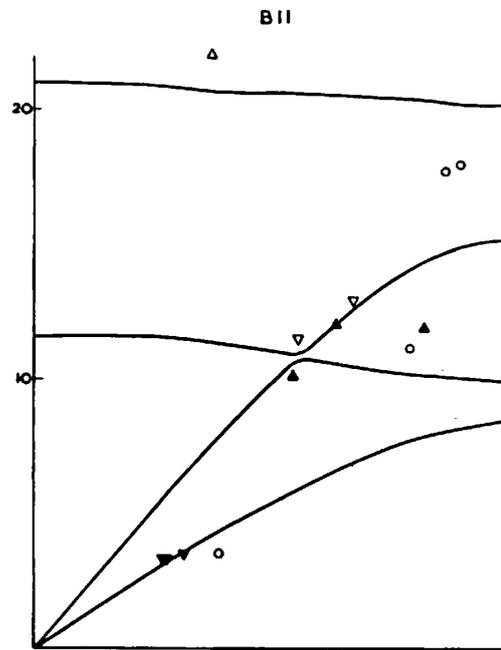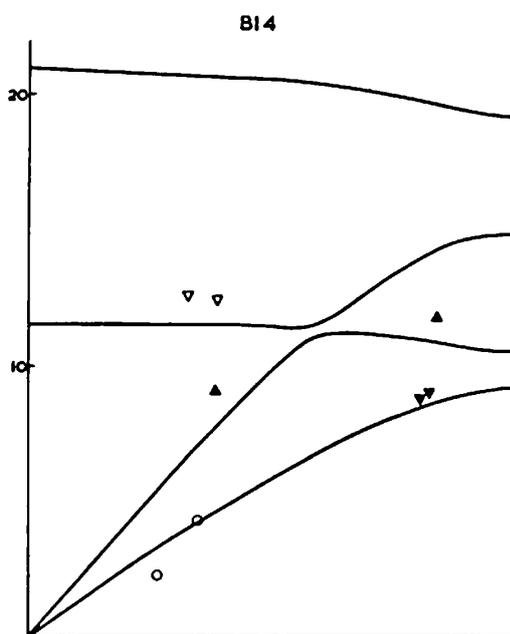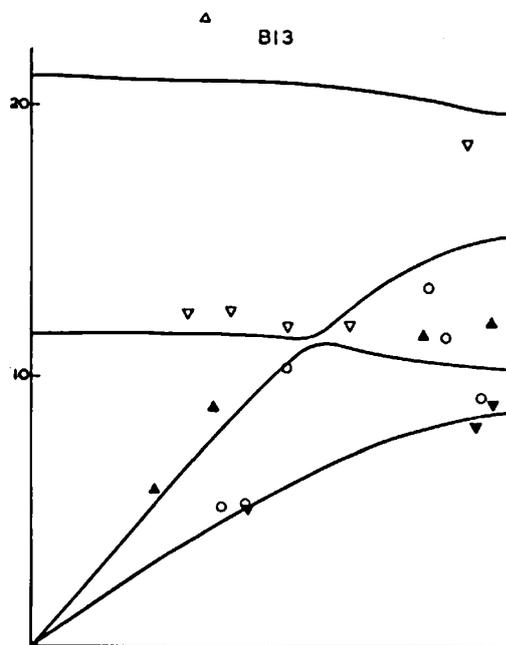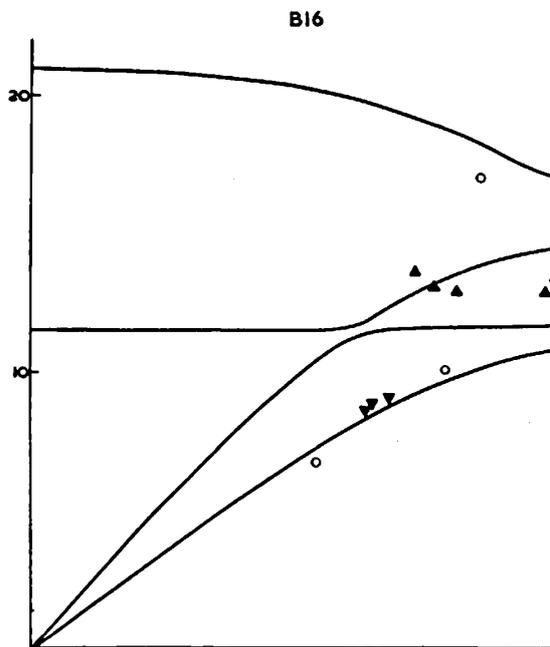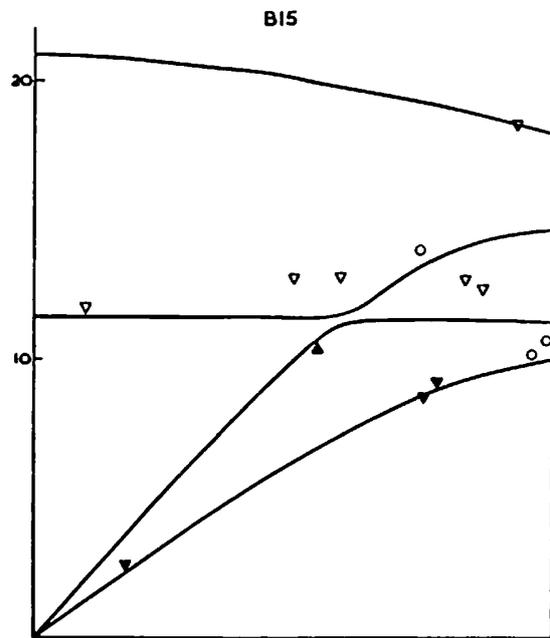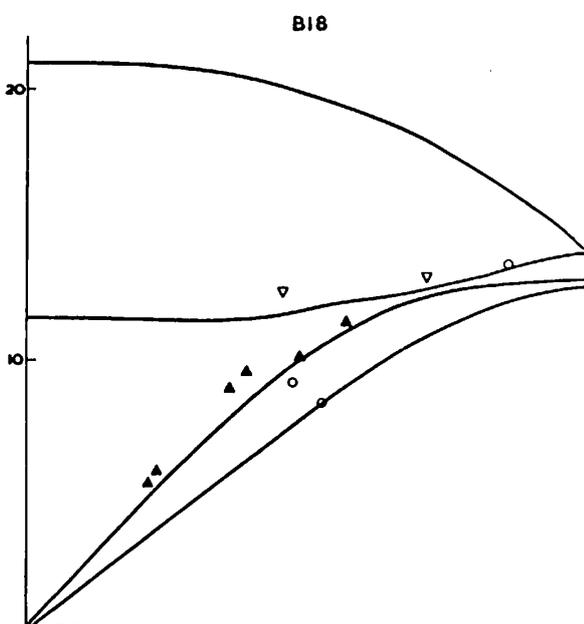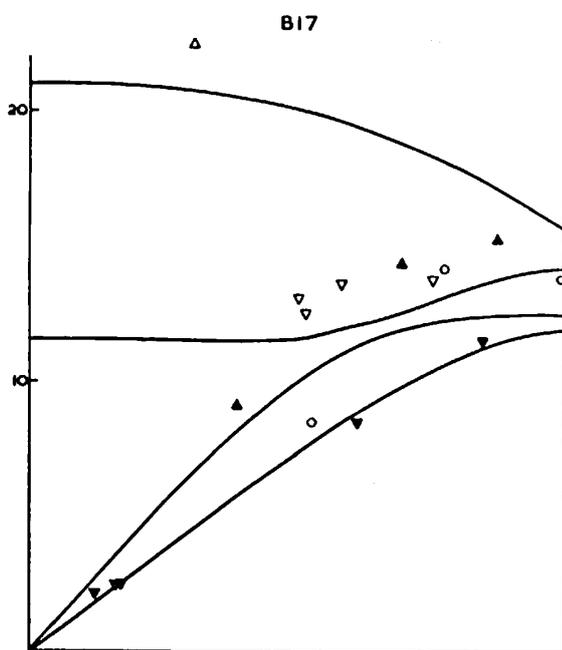
Figure 7.18

the two constituent peaks. If one branch is known to give a very small intensity, it could be assumed that the peak position corresponded to the other branch. Unfortunately, the branches are of course nearest together in the region of a degeneracy, and this is just the region where we are most unsure of the phonon polarisation vectors and hence of the intensity of the peaks. It has been shown in Chapter 6 that the polarisation vectors change rapidly near a degeneracy, and hence the polarisation vector of a particular branch for a given wave vector will depend critically on the position of the neighbouring degeneracy. This position will depend on the exact values of the parameters of the theory. In a symmetry direction, however, the polarisation vectors are known, and the above difficulty does not arise.

The sections of the dispersion relations show that branches 2 and 3 will be unresolved over quite large areas of reciprocal space.

7.5 Intensities

The cross section formula (equation 2.3) may be used to calculate the expected intensity of a peak in the time of flight spectrum given the wave vector, branch and the parameters of the theory. The Debye-Waller factor may be estimated from the Debye temperature. This, for MgO, is of the order $800°K$. A typical neutron wave vector change in the scattering process is 0.5 Å^{-1}. The factor e^{-2W} is then about 0.95. This differs little from unity, and the Debye-waller factor has therefore been ignored. The expression for g_j^2 for a crystal with the sodium chloride structure becomes

$$g_j^2 = \left(\frac{b_1}{\sqrt{m_1}} \boldsymbol{Q} \cdot \boldsymbol{\xi}_{1j} - \frac{b_2}{\sqrt{m_2}} \boldsymbol{Q} \cdot \boldsymbol{\xi}_{2j} \right)^2 \tag{7.1}$$

where the $+$ sign is taken if the lattice vector $\boldsymbol{\tau}$ in the equation

$$\boldsymbol{Q} = \boldsymbol{q} + \boldsymbol{\tau}$$

is even, and the $-$ sign if it is odd. The notation is that of Chapter 2.

An empirical formula was used for the detector efficiency E:–

$$E = \frac{1}{1.10|k_1|^3 + 1.97} \qquad (k_1 \text{ in } \text{Å}^{-1})$$

This formula approximately reproduces the efficiencies given by Harris, Wraight and Duffil (1962) for similar detectors.

The factor J_j depends on the gradient of the dispersion relation. This was calculated for each of the four possible branches for the observed phonon wave vector. The factor g_j^2 depends on the polarisation vectors, and was again calculated for each of the four possible branches. The other factors on the cross section were calculated from the experimental values of phonon frequency and wave vectors. Four theoretical intensities given by

$$I_j = E|k_1| \frac{P}{\nu} \frac{g_j^2}{J_j}$$

are thus calculated and compared with the observed intensity I_0. No attempt has been made to obtain an absolute value for the theoretical intensity, which

would depend on the sample size, beam flux, etc, but the ratio I_j/I_0 should be a constant for the experiment with a correct choice of j . In practice, this ratio was found to vary between about 0.2 and 1.2. Various factors could have caused this variation. The efficiency of the individual detectors was not measured and might have varied from one to another by as much as a factor of 2. Different volumes of the sample may have been in the beam at different crystal angles. An anomalous intensity will be found if the neutron underwent a Bragg reflection either before or after the inelastic scattering process. This latter effect will be discussed below. It seems to be important because, due to the high frequencies of some of the phonons in MgO, the wave vectors of the scattered neutrons may be large.

When the ratio I_j/I_0 was within the range mentioned for a particular j, but well outside the range for other values of j, the phonon has been plotted in figs.7.5 to 7.18 with a special symbol to indicate its branch (see key in fig.7.4). When two theoretical frequencies were similar to the observed frequency, but the other two quite different, the intensity has been used to distinguish between the two nearest branches only.

The intensity calculations are not considered to be very reliable for the reasons already given, and if a phonon quite obviously belongs to a particular branch by virtue of its frequency, this should overrule the allocation to a particular branch according to intensity. However, it is considered that if the intensity consistently favours a particular branch for several adjacent points, these points probably do belong to this branch. In Chapter 6 it was shown that the dis- persion relation takes the form of an elliptic cone in the neighbourhood of a degeneracy. A cross section passing near the degeneracy will be hyperbolic in form and the polarisation vectors will be as shown in fig. 7.19 (see fig.6.3).
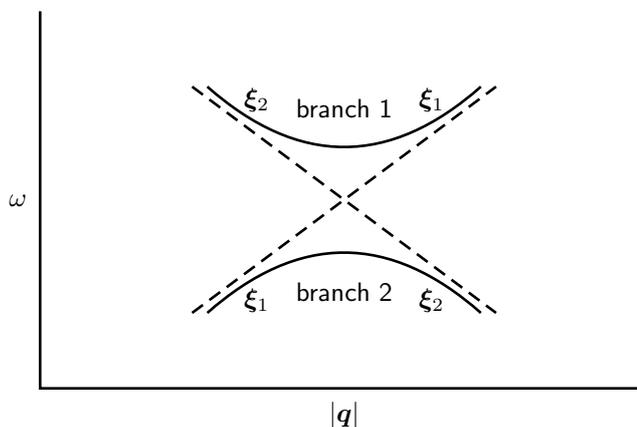
Figure 7.19: Dispersion relation near a degeneracy showing polarisations

The intensity of neutron groups scattered from branch 1 on the left of fig. 7.19 will be similar to the intensity from branch 2 on the right as both the polarisation vectors and gradients are similar.

7.6 Bragg Reflections in the Sample

If the neutrons undergo a Bragg reflection either before or after the inelastic scattering process, the calculated phonon wave vector will differ by a reciprocal lattice vector from the true phonon wave vector. This will not affect the reduced wave vector, and a point on the dispersion relation will still be obtained. However, the factor $(\boldsymbol{Q}\cdot\boldsymbol{\xi})^2$ in the intensity formula will not be correctly calculated, and the calculated intensity will not agree with the observed intensity. In fact the intensity may well indicate that the phonon belongs to a different branch. The probability of a Bragg reflection is given by the following considerations.

A neutron wave vector ($\boldsymbol{k}$) satisfies the Bragg condition if any reciprocal lattice point (Q) lies on the surface of the sphere centred on the end of the wave vector (P) , and passing through the origin (O) (fig. 7.20). Since OP = PQ in the triangle OPQ,
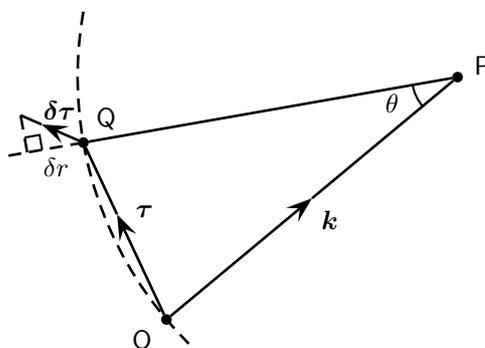
Figure 7.20: Change in neutron wave vector caused by Bragg reflection

where $\boldsymbol{\tau}$ is the reciprocal lattice vector OQ. Because of the finite resolution of the apparatus, neutrons with wave vector ($\boldsymbol{k}+\boldsymbol{\delta k}$) are also accepted by the detectors. A lattice point at ($\boldsymbol{\tau}+\boldsymbol{\delta\tau}$) would satisfy the Bragg condition with this wave vector where

$$(\boldsymbol{\tau}-\boldsymbol{k})\cdot\boldsymbol{\delta\tau}=\boldsymbol{\tau}\cdot\boldsymbol{\delta k} \tag{7.2}$$

($\boldsymbol{\tau}-\boldsymbol{k}$) is the vector PQ and $|\boldsymbol{\tau}-\boldsymbol{k}|=|\boldsymbol{k}|$. The left-hand side of equation 7.2 may be written as $|\boldsymbol{k}|\delta r$, where δr is the distance of the lattice point ($\boldsymbol{\tau}+\boldsymbol{\delta\tau}$) from the surface of the sphere OQ. If we assume that the apparatus has an independent standard deviation resolution σ in each component of $\boldsymbol{k}$, the quantity $\boldsymbol{\tau}\cdot\boldsymbol{\delta k}$ has standard deviation $|\boldsymbol{\tau}|\sigma$. The right-hand side of equation 7.2 exists between the approximate limits $\pm1.6|\boldsymbol{\tau}|\sigma$ (These limits include about 90% of the neutrons accepted by the detectors). The limits of δr are given by

$$|\boldsymbol{k}|\delta r = \pm1.6|\boldsymbol{\tau}|\sigma$$
$$\delta r = \pm1.6\frac{|\boldsymbol{\tau}|\sigma}{|\boldsymbol{k}|}$$

We may integrate over the surface of the sphere OQ to obtain the volume V in which reciprocal lattice points must lie to satisfy the Bragg condition:

$$V = \int_0^\pi 2\pi |\boldsymbol{k}|^2 \left(3.2 \frac{|\boldsymbol{\tau}|\sigma}{|\boldsymbol{k}|} \right) \sin\theta \, d\theta$$

Now $\qquad |\boldsymbol{\tau}| = 2|\boldsymbol{k}| \sin \dfrac{\theta}{2}$

The integral may be evaluated to give

$$V = 53.6 |\boldsymbol{k}|^2 \sigma$$

Table 3.4 shows that the resolution in the scattered wave vector is about 1.1% and remains more or less constant over the range of wave vectors obtained. The number of reciprocal lattice points per unit volume in reciprocal space is $2r_0^3$, and the average number of points, N, which will satisfy the Bragg condition is given by

$$N = 2r_0^3 V$$

or $\qquad N = 10.9 |\boldsymbol{k}_1|^3$

where $|\boldsymbol{k}_1|$ is in Å^{-1}.

Table 7.1: Average Number of Reciprocal Lattice Points Satisfying the Bragg Condition

Phonon frequency (c/sec)	$|\boldsymbol{k}_1|(\text{Å}^{-1})$	N
5×10^{12}	0.559	1.9
10×10^{12}	0.752	4.7

It is difficult to calculate the fraction of neutrons of a given energy that will be Bragg reflected by a crystal. The fraction will depend on the size and shape of the crystal and its mosaic spread. Calculations have been made for the case of an infinite crystal slab by Bacon and Lowde (1948). In practice it is found that, for a crystal a centimetre or so thick formed of atoms with a high coherent cross section, as much as 50% of an incident neutron beam may be reflected. The percentage reflected will be less than this if the reciprocal lattice point involved is far removed from the origin. The scattering lengths for magnesium and oxygen are similar, and the structure factor for odd lattice points which contains their difference is thus small. However, it is considered that since there are usually several reciprocal lattice points satisfying the Bragg condition for a given neutron wave vector ($\boldsymbol{k}_1$) (Table 7,1), strong reflection of the inelastically scattered neutrons will frequently occur. The presence of neutron groups with anomalous intensities is explained by this effect as was mentioned in section 7.5.

7.7 Discussion

The experimental results appear to be in good agreement with the theory. The agreement is particularly good for branch 4, the lowest frequency branch. Unfortunately, the resolution of the apparatus was not good enough for the

behaviour of branches 2 and 3 to be determined unambiguously where they are nearly degenerate. This is particularly obvious in sectors A6 to A9.

There are no points on the optic branches near the origin in any of the sectors in the (1,0,0) plane. All lattice points in this plane are even and the plus sign must be used in equation 7.1 for the structure factor. For optic modes near a lattice point, $\boldsymbol{\xi}_{1j} \approx -\boldsymbol{\xi}_{2j}$, and since the scattering lengths b_1 and b_2 are nearly equal for magnesium and oxygen, the two terms almost cancel one another, giving a very small cross section. The results for the (1,1,0) plane show that the theoretical frequencies for branch 2 near the origin are too low. This indicates that the value used for the infra-red dispersion frequency was too low. Further analysis of Smart's results, and other independent measurements show that this was indeed the case (see section 6.11).

page 201　　The revised frequencies given in Table 6.7 make branch 2 a better fit to the experimental results near the origin, but discrepancies remain near the point $(1/2, 1/2, 1/2)$ where the theoretical frequencies for this branch appear to be too low (see sectors B8 to B15).

There are very few results for branch 1 owing to its high frequency and consequent small population factor in the cross section. The few results there are indicate that the theoretical frequency is too low near the point (1,0,0), and too high near the point $(1/2, 1/2, 1/2)$ (see sectors B1 to B12). However, these are rather inaccurate measurements as the number of counts in the peaks of the time-of-flight spectra were small (fig.7.3).

Some isolated points do not appear to lie on any of the branches shown. It is possible that these points lie on the branches polarised perpendicularly to the mirror planes. The cross section for scattering by such phonons should of course be zero, but it has been pointed out that if the neutrons undergo a Bragg reflection after being inelastically scattered, neutron groups corresponding to these phonons may be observed. The theoretical frequencies for the perpendicularly polarised branches have not been calculated.

page 202　　Some of the experimental results have been presented elsewhere (Peckham, 1963), and compared with previously unpublished calculations by Hardy and Karo. The present calculations are in considerably better agreement with the experimental dispersion curves. Hardy and Karo's value for the frequency of branch 4 at the point $(1/2, 1/2, 1/2)$ for example, is almost one half that given by the *Shell Model* calculations.

The *Shell Model* provides a fairly accurate description of the crystal dynamics of magnesium oxide. However, further experimental results are required to check the frequencies given for the branch of the dispersion relation with the highest frequency. It would be necessary to perform an experiment in which the neutron loses energy to obtain such results.

Chapter 8

Crystal Spectrometer

8.1 Introduction

The frequencies of the longitudinal optic mode in magnesium oxide are expected to be as high as 21×10^{12} c/sec. At this frequency, the occupation factor, N_j, in the expression for the cross section falls to 0.033 and the mode can, therefore, be investigated only in phonon creation experiments. In this type of experiment, a high energy incident neutron beam is required. Two phased rotors are necessary to monochromate such a beam mechanically with reasonable resolution, and no such equipment was available at Harwell. However, a crystal spectrometer was available which was capable of providing a monochromatic beam of the required energy. It was decided to construct an analysing spectrometer which would convert the apparatus into a three axis spectrometer suitable for inelastic scattering experiments.

The constant $\boldsymbol{Q}$ method of operation – described in the next section – seemed to offer such advantages (Brockhouse, 1960) that the necessary control equipment was designed and built. This consisted of a mechanism to control the monochromator spectrometer arm angle, the sample angle, and the scattering angle automatically from punched paper tape. The tapes were prepared directly by the Mercury computer.

A study was made of the conditions necessary to obtain narrow, focussed peaks in the energy spectra, and a convenient graphical method of focussing was evolved.

Unfortunately, fast neutrons leaking past the collimator and through the inadequate monochromator shielding produced so high a background count rate in the detector that experiments proved impossible with the original arrangement. The apparatus is currently being rebuilt with a new collimator, and much improved shielding around the monochromator.

8.2 The Three Axis Spectrometer

A horizontal cross section of the spectrometer is shown in fig.8.1. The original apparatus consisted of a spectrometer arm which could be rotated by an electric motor about the monochromator crystal in steps of $^1/_3$ of a degree. The spectrometer arm was heavily built and counterbalanced to support the scattering sample, detectors, and shielding. The aluminium monochromator crystal was mounted on a turntable which was driven from the arm by a half angling device. This ensured that as the monochromator Bragg angle changed, the reflected beam always passed down the centre of the spectrometer arm. The monochromator crystal could be rotated on its platform by electric motors during its initial alignment and when it was desired to change the reflecting planes. The monochromator crystal was surrounded by about 18 in of shielding composed of a mixture of polythene chips, resin and boric oxide. The arm carried a further 12 in of similar shielding which covered the slot in the monochroma-
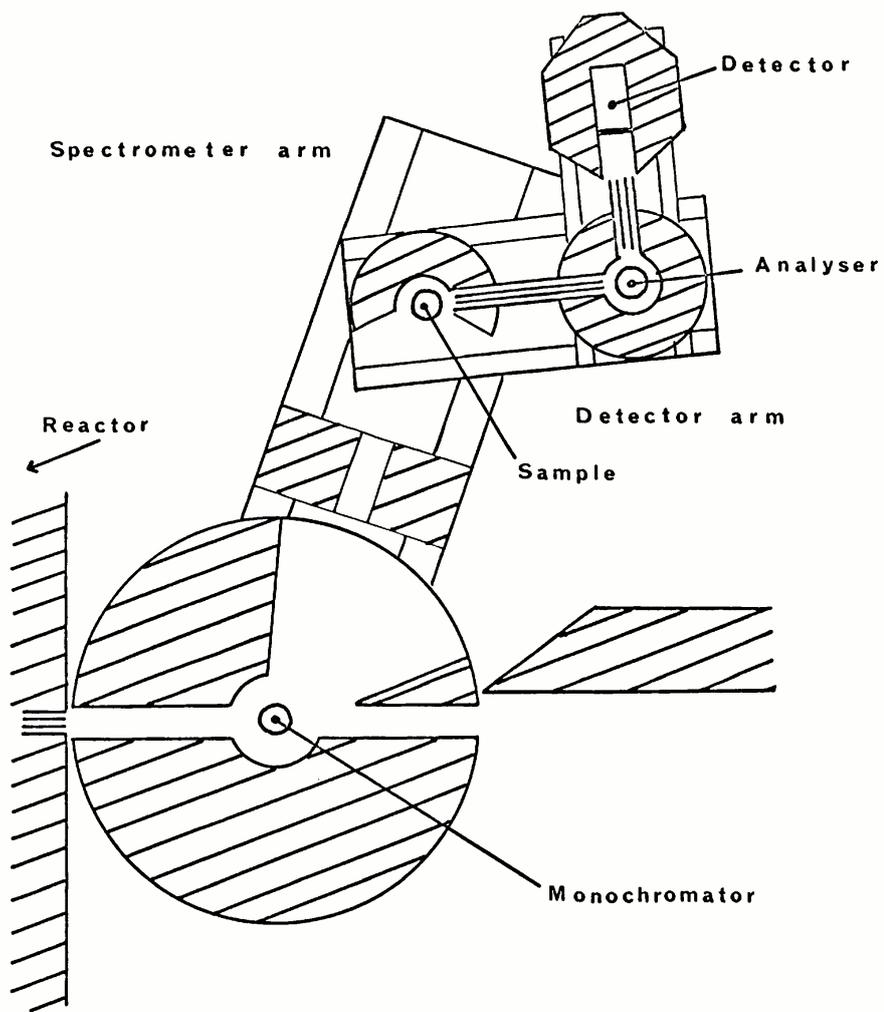
Figure 8.1: Triple axis spectrometer

tor shielding through which the beam emerged. The whole spectrometer was enclosed in a concrete blockhouse to absorb the fast neutrons and γ radiation escaping from the collimator. The radiation level inside the blockhouse was such that the blockhouse could not be entered when the collimator was open. Provision was made for closing the collimator by rotating a turret containing a steel plug, and flooding a tank in the beam with water.

The spectrometer was converted to a three axis instrument by the addition of a second arm, the detector arm, bearing an analyser crystal and detector. This arm was mounted on the end of the spectrometer arm and could rotate about a vertical axis. The sample was supported by levelling screws from a turntable which could be independently rotated about the same vertical axis. Neutrons scattered from the sample in a direction defined by a multi-slit collimator carried by the detector arm, reached the analyser crystal and, if they were of the correct energy, were Bragg reflected into the detector. A second multi-slit collimator, with twice the angular divergence of the first, was interposed between the analyser crystal and the detector to reduce the number of background neutrons reaching the detector. The detector was a scintillator similar to that used in the cold neutron apparatus. The spectrometer was intended to be used with a fixed detector energy, so no provision was made for changing the analyser Bragg angle. The analyser crystal could be rotated through 4° from its Bragg position to measure the background count rate in the detector. This motion was controlled by the existing spectrometer control equipment. The sample, analyser crystal and detector were surrounded by shielding against fast and thermal neutrons.

The triple axis spectrometer allows neutrons undergoing a desired energy and momentum change in the sample to reach the detector. A series of measurements of the scattered neutron intensity is made at closely spaced intervals along a particular line or track in energy-momentum space. Where this track crosses the phonon dispersion relation of the sample, a peak will be observed. The momentum change is restricted to the horizontal plane, but otherwise any track may be followed by adjustment of the spectrometer arm angle, the sample angle and the detector arm angle between each measurement. In particular, the momentum change may be held constant while the energy change is varied. This is the constant Q method described by Brockhouse (1960) and is very useful if the frequency of a phonon with a particular wave vector is required. Each of these angles could be varied by electric motors driving through worm-reduction gearing. The angles were measured to the nearest $^1/_{10}$th of a degree by revolution counters geared to the worm. The revolution counters could be read electrically by means of ten position switches attached to each drum, and the motor was controlled to make each revolution counter agree with a number punched on paper tape. The control equipment required to set the three angles worked in conjunction with existing equipment, which timed and printed out counts of pulses from the neutron detector. The equipment is completely automatic and is fully described elsewhere (Peckham, 1964a). Punched paper tapes for constant Q control were prepared directly by the Mercury computer.

8.3 Focussing

In a beam of neutrons which has been rendered monochromatic by Bragg reflection from a single crystal, there is a strong correlation between the direction

of travel and the energy of the neutrons. We shall show in the next section that the ends of the wave vectors of neutrons in the beam occupy a thin disc in reciprocal space. We can make use of the known orientation of this disc to determine conditions when the broadening of the peak in the observed spectrum, caused by the resolution of the apparatus, is at a minimum. These conditions are known as focussing conditions. The width of the peak is also affected by the direction of the track in energy-momentum space, which should be normal to the dispersion relation for minimum width. This effect is independent of the focussing conditions and will will not be discussed further.

We can define a scattering surface as the locus of the ends of the wave vectors of those neutrons scattered by a particular branch of the dispersion relation for a given incident neutron energy and direction. As the experiment proceeds, the disc of wave vectors acceptable to the analysing spectrometer is tracked through this surface, and while the disc is cutting the surface, a peak is observed in the scattered intensity. It is clear that the peak is narrowest when the disc is parallel to the surface. In this condition, the analyser is focussed. Similar considerations apply to the monochromator. In this case a scattering surface is defined as the locus of the ends of the wave vectors of those incident neutrons which, when scattered by phonons of a particular branch of the dispersion relation, give rise to neutrons of a given energy in a given direction. (The energy and direction are determined by the analysing spectrometer.) The disc of wave vectors of neutrons in the incident beam must be parallel to this scattering surface.

If the monochromator (or analyser) mosaic spread were zero, the disc would be parallel to the reflecting planes. It will be shown in the next section that it is always approximately in this direction, and, for the sake of simplicity, the effect of the mosaic spread will be ignored.

The Bragg condition may be written

$$\boldsymbol{k}_0 + \boldsymbol{d}_0 = \text{constant} \tag{8.1}$$

where $\boldsymbol{k}_0$ is the neutron wave vector and $\boldsymbol{d}_0$ is a vector normal to the reflecting planes (see fig.8.2).

Due to finite collimation, neutrons with wave vector $(\boldsymbol{k}_0 + \boldsymbol{\delta k}_0)$ are present, where, differentiating 8.1,

$$\boldsymbol{d}_0 \cdot \boldsymbol{\delta k}_0 = 0 \tag{8.2}$$

Conservation of energy and momentum in the scattering process give

$$\omega(\boldsymbol{Q}) = (\hbar 2m)(k_0^2 - k_1^2) \tag{8.3}$$

$$\boldsymbol{Q} = \boldsymbol{k}_0 - \boldsymbol{k}_1 \tag{8.4}$$

where $\boldsymbol{k}_0$ is the incident neutron wave vector and $\boldsymbol{k}_1$ the scattered neutron wave vector. m is the mass of a neutron. $\boldsymbol{Q}$ is the phonon wave vector and $\omega(\boldsymbol{Q})$ its angular frequency.

Incident neutrons of wave vector $(\boldsymbol{k}_0 + \boldsymbol{\delta k}_0)$ also give rise to scattered neutrons of wave vector $\boldsymbol{k}_1$ if, differentiating 8.5 and 8.4,

$$\boldsymbol{\nabla}\omega \cdot \boldsymbol{\delta k}_0 = (\hbar/m)\boldsymbol{k}_0 + \boldsymbol{\delta k}_0$$

$$\text{or} \quad (\boldsymbol{\nabla}\omega - (\hbar/m)\boldsymbol{k}_0) \cdot \boldsymbol{\delta k}_0 = 0 \tag{8.5}$$
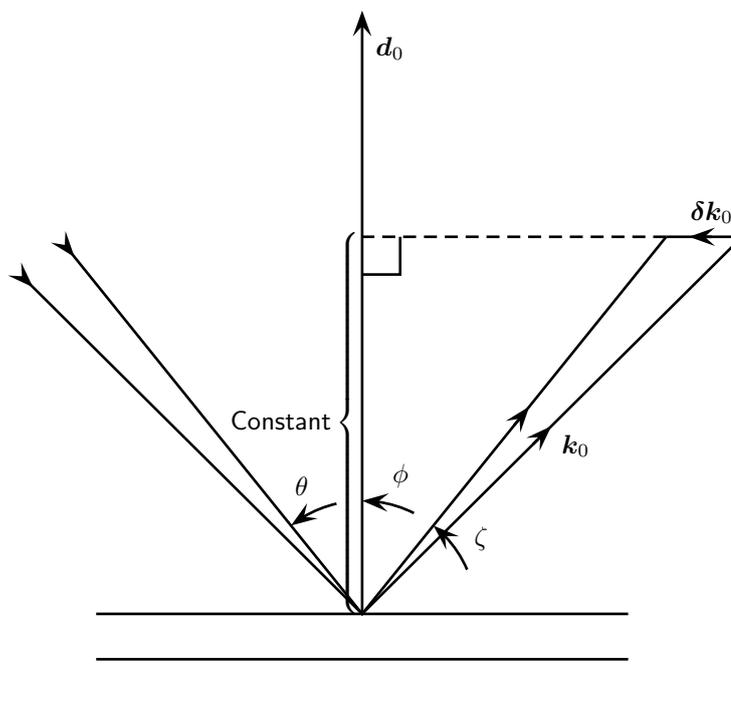
Figure 8.2: The change in wave vector of Bragg reflected neutrons on changing the incident beam direction

From equations 8.2 and 8.5, if all neutrons incident on the sample are to be capable of being scattered with wave vector $\boldsymbol{k}_1$, $(\boldsymbol{\nabla}\omega - (\hbar/m)\boldsymbol{k}_0)$ must be in the direction $\boldsymbol{d}_0$. This is the focussing condition for the monochromator.

Similar considerations apply to the analyser. $(\boldsymbol{\nabla}\omega - (\hbar/m)\boldsymbol{k}_1)$ must be in the direction $\boldsymbol{d}_1$.

Put $\boldsymbol{g} = (m/\hbar)\boldsymbol{\nabla}\omega$

The spectrometer is focussed if it is possible to draw the focussing diagram as in fig.8.3 with $\boldsymbol{g}$ drawn from the intersection of $\boldsymbol{d}_0$ and $\boldsymbol{d}_1$ to the end of $\boldsymbol{k}_0$. Frequently the spectrometer is used with either incident or scattered neutron energies fixed. In this case, generally it is not possible to satisfy the focussing conditions exactly. However, there are usually several points in the reciprocal lattice of the sample at which the desired phonon could be observed and the focussing diagram provides a convenient way to select the best point.

The focussing diagram deals with focussing in the plane of scattering when $\boldsymbol{d}_0$ and $\boldsymbol{d}_1$ also lie in this plane. With this arrangement focussing at right angles to the plane is automatically achieved if a mirror plane of the sample also lies in the plane of the spectrometer. Figure 8.4 shows another possible arrangement

116

of the spectrometer to achieve focussing.

For a longitudinal phonon (in a symmetry direction) $\boldsymbol{g}$ is parallel to $\boldsymbol{\xi}$ (the polarisation vector). Since the factor $(\boldsymbol{Q} \cdot \boldsymbol{\xi})^2$ occurs in the cross section, figure 8.4 represents a suitable arrangement for focussing longitudinal phonons. Similarly figure 8.3 represents a suitable arrangement for transverse phonons.

8.4 The Locus of the Ends of the Wave Vectors of Bragg reflected Neutrons in the Case of Finite Incident Collimation and Finite Mosaic Spread

In fig.8.2, θ, ϕ, ζ are the angles of the incident neutron, the normal to the reflecting planes, and the reflected neutron respectively, measured from a fixed direction.

From the conditions for Bragg reflection,

$$\theta - \phi = \phi - \zeta \tag{8.6}$$

or $\qquad \theta = 2\phi - \zeta$

and $\qquad k \cos(\phi - \zeta) = \text{constant} \tag{8.7}$

differentiating 8.6 and 8.7,

$$\delta\theta = 2\,\delta\phi - \delta\zeta \tag{8.8}$$

$$\delta k\,\cos(\phi - \zeta) - k\sin(\phi - \zeta)\{\delta\phi - \delta\zeta\} = 0$$

or $\qquad \delta\phi = \dfrac{\delta k}{k\tan(\phi - \zeta)} + \delta\zeta \tag{8.9}$

substituting 8.9 in 8.8,

$$\delta\theta = \frac{2\,\delta k}{k\tan(\phi - \zeta)} + \delta\zeta \tag{8.10}$$

Let the incident beam intensity as a function of angle be $I_0 \exp\left(-\dfrac{\delta\theta^2}{2\eta^2}\right)$ and let the reflectivity of the crystal be $R_0 \exp\left(-\dfrac{\delta\phi^2}{2\,\epsilon^2}\right)$.

The reflected intensity is

$$I_0 R_0 \exp\left\{-\frac{1}{2}\left(\frac{\delta\theta^2}{\eta^2} + \frac{\delta\phi^2}{\epsilon^2}\right)\right\}$$

and a contour of constant intensity is given by

$$\left(\frac{\delta\theta}{\eta}\right)^2 + \left(\frac{\delta\phi}{\epsilon}\right)^2 = \text{constant}$$

Substituting from 8.9 and 8.10,

$$\frac{\left(\frac{4}{\eta^2} + \frac{1}{\epsilon^2}\right)}{\tan^2(\phi - \zeta)}\,\delta k^2 + \frac{2\left(\frac{2}{\eta^2} + \frac{1}{\epsilon^2}\right)}{\tan(\phi - \zeta)}\,\delta k\,(k\,\delta\zeta) + \left(\frac{1}{\eta^2} + \frac{1}{\epsilon^2}\right)(k\,\delta\zeta)^2 = \text{constant}$$

The contour of constant intensity is seen to be an ellipse in wave vector space. The axes of this ellipse are at an angle α to the scattered neutron direction given by

$$\tan \alpha = \frac{\tan \alpha'}{\tan(\phi - \zeta)}$$

$$\text{where} \qquad \tan 2\alpha' = \frac{2}{3} \left(\left(\frac{\eta}{\epsilon} \right)^2 + 2 \right)$$

The angle between the minor axis and the normal to the reflecting planes is β, given by

$$\beta = (\phi - \zeta) - \alpha$$

In the following table, β_{45} is the value of β for a Bragg angle of $45°$, $\beta_{\max}$ is the maximum value of β for any Bragg angle, and r is the ratio of minor to major axes.

For any ratio of incident beam collimation (η) to crystal mosaic spread (ϵ), the locus of the ends of the reflected neutron wave vectors is seen to be a thin disc ($r \ll 1$).

Table 8.1: Orientation and Thickness of the Disc of Wave Vectors

η/ϵ	β_{45}	$\beta_{\max}$	r
0	$18°24'$	$19°24'$	0
$1/\sqrt{2}$	$15°28'$		0.12
1	$13°15'$	$13°36'$	0.15
$\sqrt{2}$	$10°15'$		0.16
∞	0	0	0

The angle (β) the normal to this disc (the minor axis of the ellipse) makes with the normal to the reflecting planes is less than $20°$.

8.5 Redesigned Instrument

Experiments proved impossible with the arrangement so far described because of the very high background count rate in the detector. This was found to be almost entirely due to fast neutrons leaking past the collimator and through the inadequate monochromator shielding. A new collimator was already being designed which should improve the position considerably, but it was also decided to build new monochromator shielding which would allow only certain discrete Bragg angles to be used. The holes in the monochromator shielding through which the beam would emerge for Bragg angles other than the one in use could be blocked, resulting in very much better shielding around the monochromator than could be obtained with the open slot in the old arrangement. As the incident beam energy would not be continuously variable, a variable energy analyser had to be constructed. This makes use of a half angling device in a similar way to the old monochromator. Much of the equipment of the old spectrometer including the control equipment is used in the redesigned instrument.
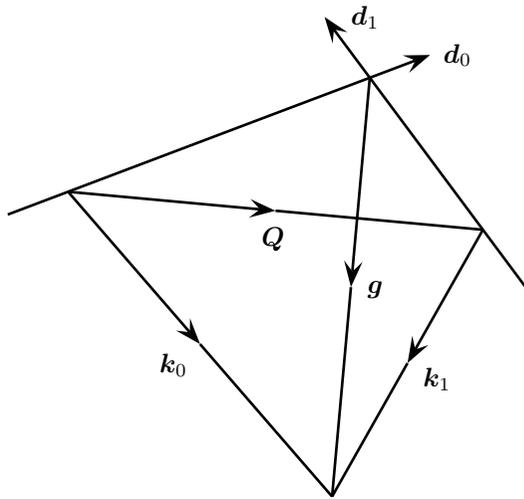
Figure 8.3a: Focussing vector diagram
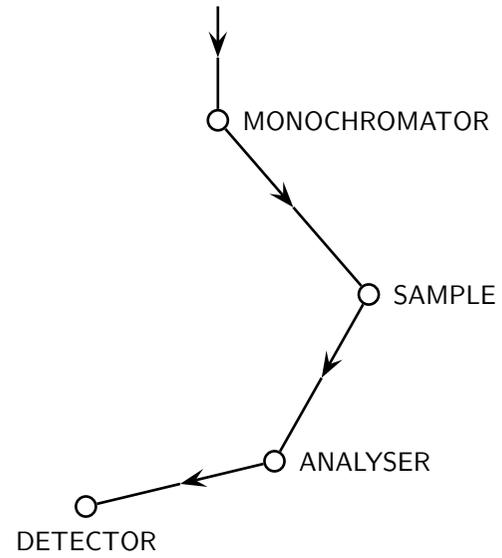
Figure 8.3b: Path of neutrons through the apparatus
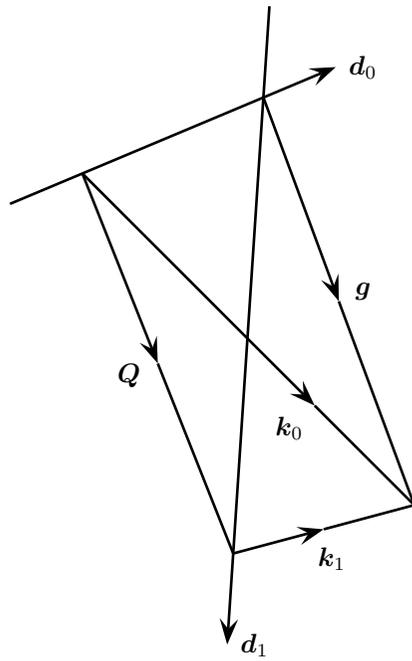
Figure 8.4a: Focussing vector diagram
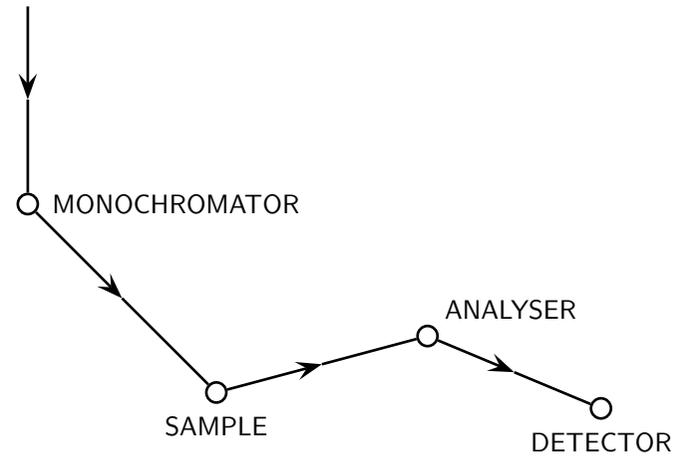
Figure 8.4b: Path of neutrons through the apparatus

Appendix I

The Circular Arc Approximation for Rotor Slots

For ease of manufacture, the rotor slots are cut as arcs of a circle. We shall show that a circular arc is a good approximation to the path of a neutron relative to axes rotating with the rotor.

Relative to fixed axes, the equation of motion of a neutron of velocity v is

$$x' = vt \qquad\qquad y' = 0$$

With respect to axes rotating with the rotor (angular velocity ω)

$$x = x' \cos\theta \qquad\qquad y = -x' \sin\theta \qquad\qquad \text{where} \quad \theta = \omega t$$

Put $v/\omega R = p$ where R is the rotor radius, then

$$vt = p\,\theta R$$
$$\text{and} \quad x = p\,\theta R \cos\theta \qquad\qquad y = -p\,\theta R \sin\theta$$

This curve is sketched below. Also shown is a circle, radius r, centre $(0, -r(1 + \beta))$, which approximates the curve. There are 5 points of maximum deviation
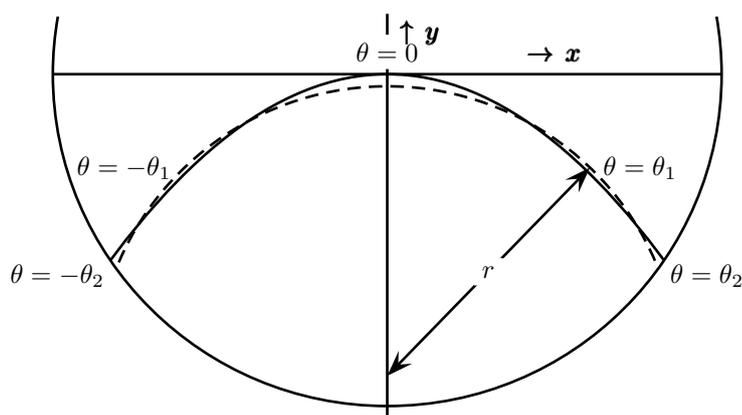
Figure I.1: Circular arc approximation for rotor slots

from the circle, corresponding to values of θ of 0, $\pm\theta_1$, $\pm\theta_2$. We shall assume that, for the circle that is the best fit to the curve, these deviations are equal in magnitude, but alternate in sign.

121

The distance of points on the curve from the centre of the circle is d given by

$$d^2 = x^2 + (y + r(1+\beta))^2$$

$$\text{or} \quad d^2 = x^2 + y^2 + 2xy(1+\beta) + r^2(1+2\beta)$$

ignoring terms of order β^2 as $|\beta| \ll 1$

$$\text{Write} \quad d = r(1+\epsilon) \quad \text{where} \quad |\epsilon| \leq |\beta| \leq 1$$

$$d^2 = r^2 + 2\epsilon r^2$$

$$\epsilon = \frac{1}{2}\left(\frac{d^2 - r^2}{x^2}\right)$$

Substituting for d^2,

$$\epsilon = \frac{x^2 + y^2}{2x^2} + \frac{y}{r}(1+\beta) + \beta$$

Substituting for x and y and putting $\frac{pR}{r} = \gamma$

$$\epsilon = \frac{\gamma^2}{2}\theta^2 - \gamma(1+\beta)\theta\sin\theta + \beta$$

To find the positions of maximum deviation, put $d\epsilon/d\theta = 0$

$$\text{or} \quad \gamma^2 - \gamma(1+\beta)(\sin\theta + \theta\cos\theta) = 0$$

The solutions are $\theta = 0$ and $\theta = \pm\theta_1$, where

$$\frac{\sin\theta_1}{\theta_1} + \cos\theta_1 = \frac{\gamma}{1+\beta} \tag{I.1}$$

$$\text{Now} \quad \epsilon(0) = -\epsilon(\theta_1) = \epsilon(\theta_2)$$

$$\text{and} \quad \epsilon(0) = \beta$$

$$\epsilon(\theta_1) = \frac{\gamma}{2}\theta_1^2 - \gamma(1+\beta)\theta_1\sin\theta_1 + \beta$$

$$\epsilon(\theta_2) = \frac{\gamma}{2}\theta_2^2 - \gamma(1+\beta)\theta_2\sin\theta_2 + \beta$$

$$\text{hence} \quad \frac{\gamma^2}{2}\theta_1^2 - \gamma(1+\beta)\theta_1\sin\theta_1 + 2\beta = 0$$

$$\text{and} \quad \frac{\gamma^2}{2}\theta_2^2 - \gamma(1+\beta)\theta_2\sin\theta_2 \quad\quad = 0$$

$$\text{or} \quad \frac{1}{4}\left(\frac{\gamma}{1+\beta}\right)^2\theta_1^2 - \frac{1}{2}\left(\frac{\gamma}{1+\beta}\right)\theta_1\sin\theta_1 + \frac{\beta}{(1+\beta)^2} = 0 \tag{I.2}$$

$$\text{and} \quad \frac{1}{2}\left(\frac{\gamma}{1+\beta}\right) = \frac{\sin\theta_2}{\theta_2} \tag{I.3}$$

Now $\theta_2 = \omega R/v = 1/p$, and for the rotors under consideration, $p \approx 3$. Equations I.1, I.2 and I.3 may be solved by expanding the trigonometric functions. From I.1 and I.3, eliminating $\left(\frac{\gamma}{1+\beta}\right)$ and expanding both sides, we obtain

$$1 - \frac{\theta_1^2}{3} + \frac{\theta_1^4}{40} = 1 - \frac{\theta_2^2}{6} + \frac{\theta_2^4}{120}$$

or $\quad \theta_1^2 = \frac{1}{2}\theta_2^2 + \frac{7}{160}\theta_2^4$

Substituting this result in I.2 and expanding,

$$\frac{\beta}{(1+\beta)^2} = \frac{\theta_2^4}{24} - \frac{29\,\theta_2^6}{2880}$$

or $\qquad \beta = \frac{\theta_2^4}{24} - \frac{29\,\theta_2^6}{2880}$

page 225 The second term in the expression for β is about $1/38$ of the first.

For the last rotor listed, $p = 3$, and $\theta_2 = 1/3$

Hence $\quad \beta = \frac{1}{1944}\left(1 - \frac{1}{38}\right) = 0.0005$

From I.3, $\gamma \approx 2$, and from the definition of γ,

$$r = \frac{pR}{\gamma} = \frac{3 \times 4}{2} = 6\,\text{ins}$$

The maximum deviation of the neutron path from the circle is βr or .003ins. The slot width of this rotor is 0.1ins. Hence the neutron does not deviate more than 3% of the slot width from the circular path, justifying the manufacture of the rotor with circular slots.

A frequently made assumption is that the best fitting arc has the same curvature as, and coincides with, the neutron path at the centre of the rotor. This assumption is equivalent to putting $\beta = 0$ and $\gamma = 2$ in our equations. The deviation at the end of the slot is then

$$\epsilon(\theta_2) = 2\theta_2\left(\theta_2 - \sin\theta_2\right)$$
$$= \frac{\theta_2^4}{3} - \frac{\theta_2^6}{60}$$

page 226 This deviation is 8 times the maximum deviation from the circular arc previously chosen. For the rotor considered above, the deviation would be 0.024ins, or $1/4$ of the slot width. If the rotor slot really deviated this much or more from every neutron path, there would be a severe loss of intensity. A circular arc is then a very much better approximation than this simplified analysis shows.

The best transmitted inverse velocity

From equation I.3 we can obtain an expression for p, the ratio of neutron speed to rotor tip speed for the neutron whose path is the best fit to the rotor slot. Substituting for γ and θ_2, we find

$$\sin(1/p) = (R/2r)/(1+\beta)$$
or $\quad \sin(1/p) = (R/2r) \quad$ as β is of order $1/2,000$ $\qquad\qquad$ (I.4)

In deriving the rotor transmission function, we obtained an expression for n_0, the best transmitted inverse velocity, i.e., the inverse velocity at which the transmission is a maximum

$$n_0 = \tau/R$$

where 2τ is the time it takes the rotor to turn from a position with one end of the slot in the neutron beam to a position with the other end in the beam. It can be shown that $\tau = 1/_\omega \sin^{-1}(R/_{2r})$

hence $\qquad n_0\,\omega R = \sin^{-1}(R/_{2r})$

or $\qquad \sin(1/_p) = (R/_{2r})$

This is identical to the expression obtained above.

Appendix II

Slots not Passing through the Centre of the Rotor

By considering the times at which neutrons passed the ends of the slot, we obtained an expression for the best transmitted inverse velocity in close agreement with that obtained from a much more careful consideration of the neutron path along the whole length of the slot. We will now apply this same method to determine the best transmitted neutron inverse velocity for a slot not passing through the centre of the rotor.
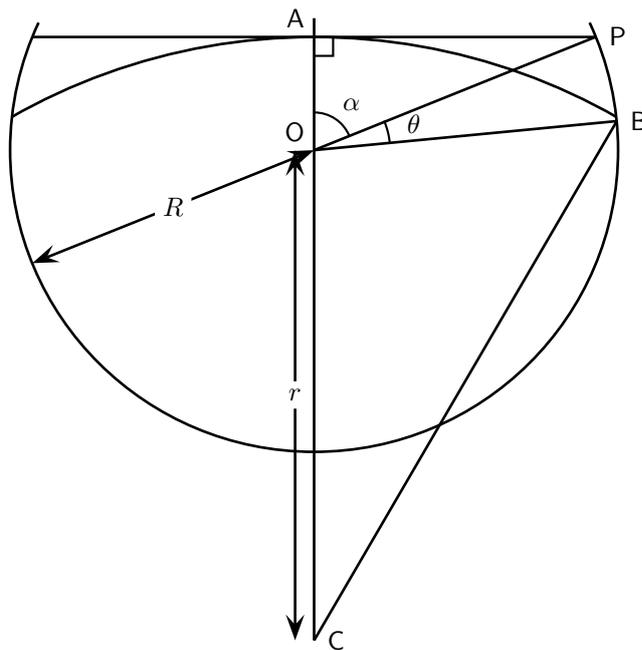
Figure II.1: Slots not passing through the centre of the rotor

In the above diagram, AB is the slot, O the rotor centre, and C the centre of curvature of the slot. CO meets the slot at A, and P is a point on the periphery of the rotor such that PA is perpendicular to CO.

A neutron following the slot travels from A to P while the rotor turns through

125

the angle BOP (marked θ in the diagram). Hence, with our previous notation,

$$n = \frac{\theta}{\omega R \sin \alpha}$$

$$\text{or} \quad \theta = \frac{\sin \alpha}{p}$$

In triangle BOC,

$$BC^2 = CO^2 + BO^2 + 2BO\,CO\,\cos \widehat{BOA}$$

$$\text{or} \qquad (r + R \cos \alpha)^2 = r^2 + R^2 + 2Rr\cos(\alpha + \theta) \qquad \text{(II.1)}$$

$$\text{and} \quad \cos\left(\alpha + \frac{\sin \alpha}{p}\right) = \cos \alpha - \frac{R}{2r}\sin^2 \alpha$$

$$\text{or} \qquad \cos\left(\alpha + \frac{\sin \alpha}{p}\right) = \cos \alpha - \sin\left(\frac{1}{p_0}\right)\sin^2 \alpha$$

Where $\sin(1/p_0) = R/2r$, and p_0 is the ratio of neutron speed to rotor tip speed for a slot with the same centre of curvature, but passing through the centre of the rotor.

For the slot through the rotor centre, $\alpha = \pi/2$. Differentiating the above *page 230* expression, and putting $\alpha = \pi/2$ and $p = p_0$, we find

$$\frac{dp}{d\alpha} = p_0^2\left(1 - \frac{1}{\cos 1/p_0}\right) - \left(\frac{1}{2} + \frac{5}{24}\frac{1}{p_0^2} + \cdots\right)$$

This gives the approximate expression for p

$$p = p_0 + \beta\left(\frac{1}{2} + \frac{5}{24 p_0^2}\right)$$

where $\beta = \pi/2 - \alpha$

For $p_0 = 3$ and $\cos \alpha = 1/4$, the accurate expression gives $p = 3.129$, and the approximate expression $p = 3.132$.

For a rotor with many slots extending over a width $2c$ and all cut with the same centre of curvature, the limits of β are approximately $\pm c/R$. The corresponding limits of p are given by

$$p - p_0 = \pm\frac{c}{R}\left(\frac{1}{2} + \frac{5}{24}\frac{1}{p_0^2}\right)$$

We may define a width in p as the square root of the second moment of the neutron distribution as a function of p

$$\delta p = \frac{1}{\sqrt{3}}\frac{c}{R}\left(\frac{1}{2} + \frac{5}{24}\frac{1}{p_0^2}\right)$$

$$\text{or} \quad \frac{\delta p}{p_0} = \frac{\delta n}{n_0} = \frac{1}{\sqrt{3}}\frac{c}{R p_0}\left(\frac{1}{2} + \frac{5}{24}\frac{1}{p_0^2}\right) \qquad \text{(II.2)} \qquad \textit{page 231}$$

For rotor 3, $c = 1$", $R = 4$", $p_0 = 3$. *page 231*

$$\text{Then} \quad \frac{\delta n}{n_0} = 0.0252$$

126

This is almost equal to the spread in velocities due to the finite width of the slots previously calculated for this rotor.

For ease of manufacture, rotors are usually made with all the slots cut with the same centre of curvature. It has been shown that this leads to an appreciable increase in the velocity spread transmitted by the rotor, and it is of some interest to see how the centre of curvature should be changed for slots not passing through the centre of the rotor.

Differentiating equation II.1 with respect to α, keeping p constant,

$$\frac{dr}{d\alpha} = r\,\frac{1 - \cos(1/p_0)}{\sin(1/p_0)} \quad \text{when } \alpha = \frac{\pi}{2} \text{ and } p = p_0$$

If c is the distance OA of the slot from the rotor centre,

$$
\begin{aligned}
\frac{dr}{dc} &= -\frac{1}{R}\frac{dr}{d\alpha} \\
&= -\frac{r}{R}\,\frac{1 - \cos(1/p_0)}{\sin(1/p_0)} \\
&= -\frac{1}{2}\,\frac{1 - \cos(1/p_0)}{\sin^2(1/p_0)} \\
&= -\frac{1}{2}\,\frac{1}{1 + \cos(1/p_0)}
\end{aligned}
$$

r should be increased by an amount δr given by

$$
\begin{aligned}
\delta r &= -\frac{c}{2}\,\frac{1}{1 + \cos(1/p_0)} \\
&= -\frac{c}{4}\left(1 + \frac{1}{4}\left(\frac{1}{p_0}\right)^2 + \frac{1}{24}\left(\frac{1}{p_0}\right)^4 + \cdots\right)
\end{aligned}
\tag{II.3}
$$

If we compare this slot with the one through the centre of the rotor, we find to a first approximation that the centre of curvature should be displaced $1/4$ as far as the slot is displaced and in the same direction. A more accurate value could be obtained in a particular case by using equation II.1.

127

Appendix III

Alignment of Apparatus

III.1 Goniometer Alignment

The axis of rotation of the goniometer is made perpendicular to the scattering plane by adjustment of the goniometer platform levelling screws. The alignment is checked optically. (Refer to fig. 3.1)

(1) A telescope has been fixed in the line of the beam near the reactor wall. with the beam off and the beamstop removed, crosswires at the position of the beam stop are adjusted to be in line with this telescope and the aperture in the rotor tank.

(2) A double-sided mirror is inserted in the goniometer in place of the crystal. The mirror should be parallel to the small arc of the goniometer. A band is placed across the mirror at a position corresponding to the centre of the crystal. The goniometer arcs and lateral slides are adjusted to their zero marks, so that the axis of rotation of the goniometer lies approximately in the plane of the mirror.

(3) The mirror is viewed from the beam stop, and the goniometer platform is adjusted vertically and horizontally until the part of the mirror crossed by the band appears central against the aperture in the rotor tank.

(4) The goniometer is turned so that the mirror is in a vertical plane, and a vertical wire is erected at the beam stop so that the wire, its image in the mirror, and the band are in line. The mirror is turned through 180° and a second wire erected in the same way. A third wire is placed midway between the first two and the first two wires are removed. The goniometer large arc is adjusted so that this wire, its image in the mirror and the band are in line.

The axis of rotation of the goniometer should now be parallel to the plane of the mirror. The mirror is again rotated through 180° to check that the wire remains in line with its image and the band, and the adjustment repeated if necessary. When making this check, it should be remembered that as the crosswires are about 5 ft from the mirror, if the mirror is 0.1° out of alignment, the image and the band will appear in line when viewed from a point 0.2 ins to one side of the wire. The wire is now removed.

(5) The goniometer platform is turned about a vertical axis until the vertical cross wire, its image, and the band are in line. The axis of rotation of the goniometer should now be perpendicular to the neutron beam direction. The mirror is turned through 180° and a check is made that the vertical cross wire, its image, and the band are still in line.

(6) The first (90°) detector is adjusted to be central between the shielding tanks. The position of this detector, together with the direction of the incident beam, defines the scattering plane.

The goniometer is turned so that the image of this detector in the mirror is visible from the beam stop. The goniometer platform is tilted about an axis parallel to the beam until the vertical crosswire, the band on the mirror, and the centre of the image of the detector are in line.

The axis of rotation of the goniometer should now be perpendicular to the scattering plane. The last adjustment is checked by rotating the mirror through 180° and checking that the vertical crosswire, the band, and the image of the detector are still in line.

(7) The goniometer is turned so that each of the other detectors in turn is visible in the mirror from the beam stop. The position of the detectors between the side tanks is adjusted so that they line up in the same way as the first detector.

All of the detectors now lie in the scattering plane.

(8) The angle of each detector is found by rotating the goniometer until the image of the detector appears central in the mirror when viewed from the horizontal crosswire at the beam stop, and then reading the vernier scale attached to the goniometer axis. The reading of the vernier scale should also be noted for the position of the goniometer when the image of the horizontal crosswire itself appears central in the mirror. These readings are noted for both sides of the mirror so that scale eccentricity can be allowed for. The mirror is removed

(9) The distances from monitor 1 to the sample, from monitor 1 to monitor 2, and from the sample to each of the detectors is measured.

III.2 Alignment of the Single Crystal Sample

It is assumed that we wish to align the crystal with a mirror plane parallel to the scattering plane. This can be done by adjusting the goniometer so that Bragg reflections from two planes at right angles to this mirror are observed in one of the detectors. The beryllium filtered beam which will be used in the inelastic scattering measurements can be used if planes can be found with a spacing of more than 2.8 Å. The lead crystal was aligned in this way as its (1, 1, 1) planes have a spacing of 2.85 Å. However, most crystals do not have such widely spaced planes, and in order to observe Bragg reflections in the detectors, a higher energy incident beam must be used. The beam turret may be rotated, moving the beryllium filter out of the beam and allowing higher energy neutrons to emerge from the reactor. The rotor must also be lifted clear of the beam. One of the magnesium oxide crystals was aligned using this open beam.

Many ionic crystals will cleave along symmetry planes, allowing them to be aligned optically by reflection from these cleaved surfaces. Both the magnesium oxide crystals were aligned in this way.

Neutron alignment

(1) The crystal is inserted in the goniometer so that the large arc is not parallel to either of the planes which are to be used to align the crystal.

The output of the 90° detector is taken to a ratemeter.

(2) The crystal is adjusted to approximately the correct position for a Bragg reflection to be observed in this detector. If this position is not known, it is best to commence the alignment using a detector which subtends a much larger angle.

A search is made for the Bragg reflection by making a series of sweeps with the motor-driven axis of the goniometer for settings of the large arc spaced about $1/2°$ apart. The readings of the vernier scale and of the large arc should be noted when the ratemeter indicates a maximum. A flexible drive is provided for the large arc so that it may be adjusted without the beam being turned off.

Let the angle between the Bragg reflecting plane normal and the normal to the plane containing the large arc be θ_1, and let the scale reading of the large arc be α_1

(3) Repeat this search for the other Bragg reflection, again adjusting the motor-driven axis and the large arc only. Let the corresponding angles be θ_2 and α_2.

(4) The angle α to which the large arc should be set is given by

$$\alpha = \frac{\alpha_1 \tan \theta_1 - \alpha_2 \tan \theta_2}{\tan \theta_1 - \tan \theta_2}$$

The angle β by which the small arc should be moved is given by

$$\beta = \frac{\alpha_1 - \alpha_2}{\cot \theta_1 - \cot \theta_2}$$

The positive directions of rotation are given in the following diagram.
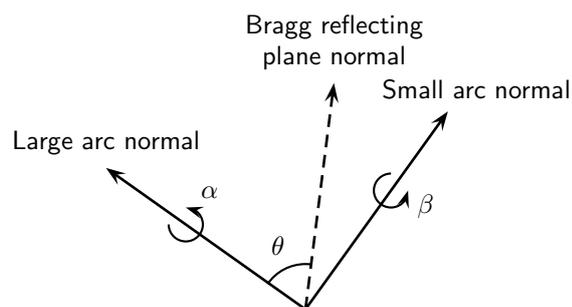
Figure III.1: Goniometer arc rotation angles

(5) With the arcs set to these angles, it should be possible to observe both Bragg reflections by rotating the goniometer about the motor-driven axis only. If either of the reflections are significantly weaker than before, the adjustment must be repeated.

The crystal is now oriented with the mirror plane in the scattering plane.

Optical Alignment

Two cleaved planes cannot always be found which are perpendicular to the mirror plane chosen as the scattering.plane. The procedure will depend on the cleaved faces available on any particular sample. The methods used to align the two magnesium oxide crystals will be described.

Crystal A

This crystal was to be aligned with a (1,1,0) mirror plane as the scattering plane. It possessed one cleaved (1,0,0) plane (a) perpendicular to this mirror plane, and two more cleaved planes of the same type (b and c) at 45° to the mirror plane.

(1) The crystal was mounted in the goniometer with plane (a) parallel to the small arc. A strongly illuminated slit was placed by the vertical crosswire at the beam stop, and the large arc adjusted until the vertical crosswire, the image of the slit in plane (a), and the centre of the crystal were in line.

(2) The illuminated slit was next placed as shown in the following diagram
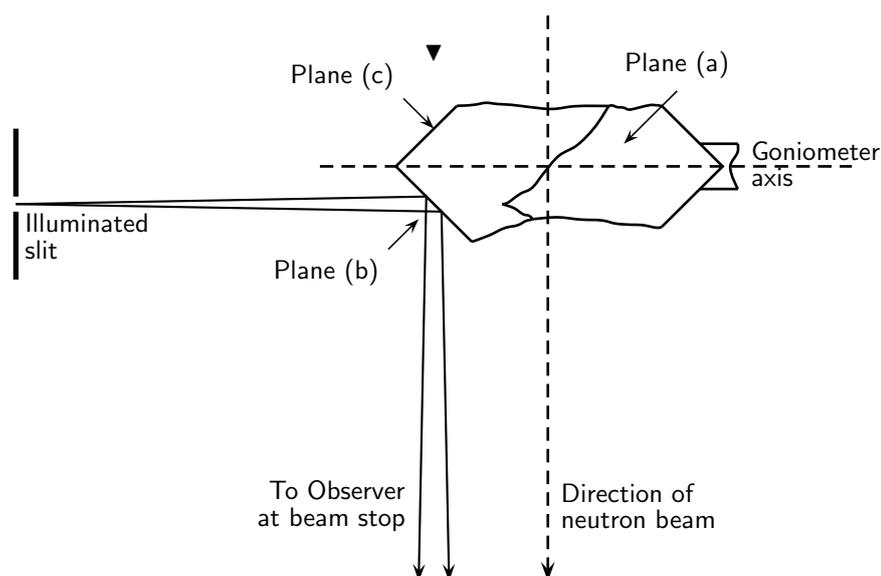
Figure III.2: Optical alignment of a magnesium oxide crystal

so that its reflection in plane (b) could be observed from the beam stop. A wire was erected at the beam stop in line with the image of the slit and a mark atthe crystal. The goniometer was then rotated through 180° so that the image of the slit was observable in plane (c). A second wire was erected in the same way. A third wire was placed midway between the first two, and the first two removed. The small arc was then adjusted so

that the image of the slit, the mark at the crystal, and the wire were in line.

This procedure was repeated until the same wire was in line with the image of the slit and the mark at the crystal when viewed in both planes (b) and (c) .

(3) The alignment of this crystal was checked by the neutron method already described. The two methods were found to agree within $1/4^{\circ}$

Crystal B

This crystal was to be aligned with a (1,0,0) mirror plane parallel to the scattering plane. The alignment was more straightforward as all four (1,0,0) faces perpendicular to the (1,0,0) mirror plane were cleaved. The crystal was mounted in the goniometer with these cleaved faces parallel to the goniometer arcs, and both arcs were adjusted as in paragraph (1) for crystal A.

References

page 244   Bacon,G.E., and Lowde,R.D. (1948). Acta Cryst. **1**, 303.

Born,M. and Huang,K., 1954. *Dynamical Theory of Crystal Lattices*, Oxford University Press.

Born,M. and Kármán,Th.von, 1912. Phys. Zeit. **13**, 297.

Brockhouse,B.N., 1960. Proc. Symp. on Inelastic Scattering of Neutrons, Vienna, p.113 (published by International Atomic Energy Agency, Vienna, 1961).

Brockhouse,B.N., Arase,T., Cag1ioti,G., Sakamoto,M., Sinc1are,R.N., Woods,A.D.B., 1960. Proc. Symp. on Inelastic Scattering of Neutrons, Vienna, p.531 (published by International Atomic Energy Agency, Vienna, 1961).

Brockhouse,B.N., Becka,L.N., Rao,K.R., Woods,A.D.B., 1962. Proc. Symp. on Inelastic Scattering of Neutrons, Chalk River, Canada vol.II, p.23 (published by International Atomic Energy Agency, Vienna, 1963).

Chung,D.H.,1963. Phil. Mag. **8**, 833.

Cochran,W., 1961. Advances in Physics **10**, 401.

Cocking,S.J., 1960. Proc. Symp. on Neutron Time-of- Flight Methods, Saclay, France, p.283 (published by European Atomic Energy Community, Brussels, 1961).

Collins, M.F., 1961. Dissertation, University of Cambridge.

Cowley,R.A., 1962, Proc. Roy. Soc. **A268**, 109 and 121. Cowley,R.A., Cochran,W., Brockhouse,B.N., Woods,A.D.B., 1963, Phys. Rev. **131**, 1030.

Dick,B.G., and Overhauser,A.W., 1958, Phys. Rev. **112**, 90.

page 245   Dolling,G., 1961. Dissertation, University of Cambridge.

Field,R., Smart,C., and Wilkinson,G.R., 1964. To be published.

Foreman,A.J.E., and Lomer,W.M., 1957. Proc .Phys. Soc., **B70**, 1143.

Goldschmidt,V.M., 1926. Skrifter det Norske Videnskaps Akademie **2**, 1927, **8**.

Goens,E., and Weerts,J., 1936. Physik. Zeits. **37**, 321.

Häfele,H.G.von, 1963. Annalen der Physik 7-10, 321.

Ha1l,J.W., 1959. U.K.A.E.A. Reports AERE – M 502 and M 558.

Hanlon,J.E., and Lawson,A.W., 1959, Phys. Rev., **113**, 472.

133

Hardy,J.R., and Smith,S.D., 1961, Phil. Mag. **6**, 1163.

Harris,D., Cocking,S.J., Ege1staff,P.A., Webb,F.J., 1962. Proc. Symp. on Inelastic Scattering of Neutrons, Chalk River, Canada, Vol.I, p.107 (published by International Atomic Energy Agency, Vienna, 1963).

Harris,D., Wraight,L.A., and Duffil,C., 1962. Proc. Symp. on Inelastic Scattering of Neutrons, Chalk River, Canada, Vol.I, p.171 (published by International Atomic Energy Agency, Vienna, 1963).

Hove,L.van, 1953. Phys. Rev. **89**, 1189.

Ke11ermann,E.W., 1940. Phil. Trans. **A238**, 63.

Kitte1,C., 1956, *Introduction to Solid State Physics*, Wiley, New York.

Landau,L.D., and Lifshitz,E.M., 1958. *Quantum Mechanics*, Permagon Press, London.

Marseguerra,M., and Pau1i,G., 1959. Nuc1. Inst. **4**, 140.

Pauling,L., 1948. *Nature of the Chemical Bond*, p.343, Cornell.

Peckham,G.E., 1965. Proc.Int.Conf.on Lattice Dynamics, Copenhagen (To be published as a supplement to Journal of the Physics and Chemistry of Solids).

Peckham,G.E., 1964a. U.K.A.E.A. report AERE – M 1423

Peckham,G.E., 1964b. U.K.A.E.A. report AERE – M 1424

Peckham,G.E., 1964c. U.K.A.E.A. report AERE – M 1425

P1aczek,G., and Hove,L.van, 1954. Phys.Rev. **93**, 1207.

Smart,C., 1961 . Thesis, King's College, London.

Squires,G.L. 1962. Proc. Symp. on Inelastic Scattering of Neutrons, Chalk River, Canada, Vo1.II, p.55 (published by International Atomic Energy Agency, Vienna, 1963).

Squires,G.L., 1963. Arkiv för Fysik **25**, 21.

Stedman,R., 1960. A.E.C.L. report CRRP 931.

Sun,K.N., Malmberg,P.R., Pecjak,F.A., 1956. Nucleonics **14**, 46, No.7.

Turberfield,K.C., and Egelstaff,P.A., 1960. Proc. Int. Conf. on Inelastic Scattering of Neutrons, Vienna, p.581 (published by International Atomic Energy Agency, Vienna, 1961).

Wa1ker,C.B., 1956, Phys.Rev. **103**, 547.

Wa11er,I., and Fröman,P.O., 1952. Arkiv för Fysik,4,183.

Wasastjerna,J.A., 1923. Soc. Sci. Fenn. Comm. Phys. Math. **38**, 1.

Webb,F.J., and Pearce,D.G., 1962. Proc. Symp. on Inelastic Scattering of
    Neutrons, Chalk River, Canada, vol. I p.83 (published by International
    Atomic Energy Agency, Vienna, 1963).

Woods,A.D.B., Cochran,W., Brockhouse,B.N., 1960. Phys. Rev. **119**, 1980.

Wraight,L.A., 1964, U.K.A,E.A. report AERE – M 833.